SCUOLA SUPERIORE MERIDIONALE
University of Naples Federico II

DOCTORAL THESIS
in Modeling and Engineering Risk and Complexity

Investigating climate compound events via complex climate networks

---

Author:
Domenico Giaquinto

Supervisors:
Prof. Jürgen Kurths
Prof. Warner Marzocchi

Submitted in fulfilment of the requirements for
the degree of Doctor of Philosophy in
Modeling and Engineering Risk and Complexity.
Coordinator: Prof. Mario di Bernardo.

31 October 2024

"C’è quindi una sfida della complessità: essa si ritrova
in ogni conoscenza, quotidiana, politica, filosofica e,
in maniera ormai acuta, nella conoscenza scientifica.
Essa si espande anche sull’azione e sull’etica."

Edgar Morin, *La sfida della complessità*

Abstract

The Earth system is a complex ensemble of elements and processes occurring at various spatio-temporal scales. Climate science is indeed one of the most complex field of study: different chemical, biological and physical processes take place among several environmental compartments, each one characterized by their own variables and dynamics. Despite the giant steps made in this field, climate scientists are facing many open questions, which are becoming more and more pressing due to the rising impacts of climate change, such as the multi-scale and chaotic nature of the climate system, tipping elements dynamics and their interactions, the spatio-temporal dynamics and impacts of climate and weather extremes and compound events, the causal relationships between climate processes. In particular, we are facing the simultaneous increase of the frequency and the intensity of weather and climate extremes, which result in major impacts on ecosystems and society.

The research presented in this dissertation falls within the field of climate science, utilizing an interdisciplinary approach that bridges the gap between complex systems science and atmospheric physics. This approach employs modern analytical techniques derived from complex networks science and applied to the study of extreme climate events. In particular, we develop a robust methodology to construct climate networks from data, minimizing uncertainties related to link attribution. We apply this methodology to uncover the spatio-temporal structures of hot and dry extremes synchronizations in Europe. Moreover, we identify and describe the causal relationships behind hot and dry compound events and characterize the atmospheric precursors responsible for the occurrence these events.

In our first application, we investigate the spatial patterns and features of meteorological droughts in Europe using event synchronization analysis. We establish robust continental networks of meteorological droughts based on the co-occurrence of these events at different locations for the period 1981-2020 and compare the results for different accumulation periods of rainfall. Each continental network is then further examined to unveil regional clusters which are characterized in terms of droughts propagation.

For our second application, we extend our methodology to build evolving spatially embedded climate networks of compound hot and dry synchronizations. Focusing on the summer and winter seasons of the period 1941-2020, we highlight hotspot regions in Europe where these spatially compound extremes are increasing and analyse the atmospheric precursors driving these anomalous conditions. This way, we bring out key

aspects concerning the underlying spatio-temporal dynamics of concurrent hot and dry events.

In the third application, we apply causal discovery to the study of hot and dry extremes in central Europe, by using causal effect networks. We show that hot extreme events in central Europe are driven primarily by anomalous atmospheric patterns and soil water deficiency, while dry extreme events are mainly induced by anomalous atmospheric patterns and soil moisture memory. We describe the historical trends of the found causal links in 1979-2020, and we find that the influence of dry soil on temperature has been amplified by 67% during compound hot and dry extremes, while the impact of atmospheric drivers on soil moisture has intensified by 50% during compound extremes.

Climate complex networks help identifying non trivial spatio-temporal patterns of extreme events, getting new insights into the statistical relationships of the analysed phenomena. To the best of our knowledge, so far few works have addressed compound events by using climate networks and causal effect networks. The aim of our research is to fill this gap, improving our understanding of hot and dry extremes in Europe, revealing their synchronization, propagation mechanisms and causal structure.

Contents

II Applications 37

1 Introduction

Over the last decades, climate change has emerged as one of the most pressing issues for ecosystems and society. It is crucial to understand the role of humankind, what are the major threats connected to global warming and what we should do to mitigate or avoid the most dangerous future scenarios. The scientific community is putting a lot of effort into the studying of climate, approaching it in a multidisciplinary way, from physics to engineering, chemistry, mathematical modelling, statistics, sociology, politics and so on. Indeed, climate science is one of the most complex field of study: different chemical, biological and physical processes take place among several environmental compartments, each one characterized by their own variables and dynamics. Climate change and global warming are threatening life as we know it, due to the increasing occurrence and intensity of extreme weather and climate events, which result in strong impacts on natural ecosystems, human society, and global economy. Investigating atmospheric mechanisms is therefore not only a scientific matter, but is needed in order to predict and mitigate forthcoming extreme events.

The research presented in this dissertation, conducted as part of the PhD program in "Modeling and Engineering Risk and Complexity" (MERC) at the Scuola Superiore Meridionale, falls within the field of climate science, utilizing an interdisciplinary approach that bridges the gap between complex systems science and atmospheric physics. This approach employs modern analytical techniques derived from the science of complex networks and applied to the study of extreme meteorological and climate events, following a line of research that began about twenty years ago. The Potsdam Institute for Climate Impact Research (PIK), a leader in Earth system research, has been and continues to be one of the most specialized centers in the field of climate networks. I had the privilege of being a guest at PIK during the springs of the 2022-2024 triennium, for a total of one year of activities. Much of the results presented in this thesis were developed during my stay at the PIK in the Complexity Science department, under the kind supervision of Prof. Jürgen Kurths. I would also like to take this opportunity to thank Prof. Warner Marzocchi for his invaluable human and scientific support throughout my PhD.

In the following, we describe the scientific context and the key research questions of our work, as well as its relevance to risk and complexity areas. We conclude the Introduction by outlining the structure of this dissertation.

1.1 Context of the research topic

1.1.1 Climate science and climate modeling

The Earth system is a complex ensemble of elements and processes occurring in various environmental compartments, such as the atmosphere, the cryosphere, the hydrosphere, and the biosphere (Figure 1.1).

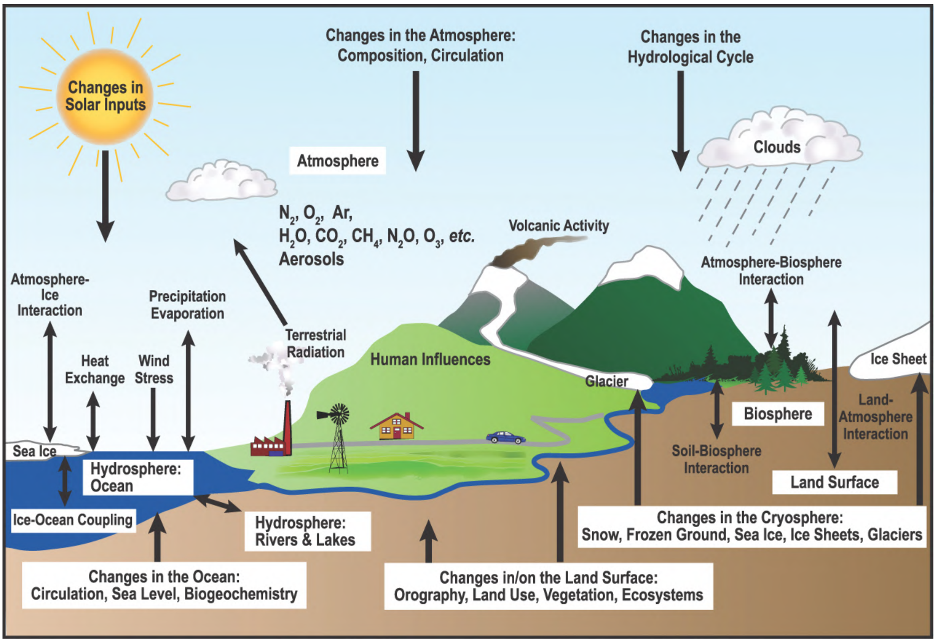

Figure 1.1: **The climate system.** Schematic view of the components of the climate system, their processes and interactions. From the fourth assessment report of the Intergovernmental Panel on Climate Change (Solomon et al., 2007).

Depending on the temporal scale at which these processes are observed and described, a distinction is made between the weather and the climate. The first refers to the short-term (minutes to weeks) changes in the atmosphere, while the latter is defined as the statistical description over a long period of time (30 years at least) of relevant quantities and processes. Consequently, although weather and climate temporal scales differ, the underlying and fundamental physical processes are the same.

The traditional approach to model and predict both weather and climate involves the use of advanced high-dimensional physical models. The Earth system is reduced into its numerous components and - often - nonlinear processes and physical laws are used to model all the relevant environmental aspects, according to the objective of the study. Modern computational resources allow scientists to numerically simulate these physical models, coupling the different environmental compartments (typically the atmosphere and the oceans above all) in a global representation of the Earth system.

The history of climate modelling dates back to the 19th century. In 1861, John Tyndall discovered the greenhouse effect by observing that some gasses like water vapour, carbon dioxide, methane and others are capable of absorbing and re-radiating infrared energy as heat (Tyndall, 1862). A little later, in 1896, Svante Arrhenius quantitatively assessed climate sensitivity, i.e. the change in the surface temperature following a doubling of CO_2 concentration in the atmosphere, laying the foundation of climate modelling (Arrhenius, 1896). It was in 1904 when Vilhelm Bjerknes suggested to use physical laws for weather prediction (Bjerknes, 1904) and, in 1922, Lewis Fry Richardson completed the picture by using numerical modeling for weather predictions (Richardson, 1922). Thereby, in the early 1900s everything was set for scientists to tackle climate modeling, and indeed, in 1950, John von Neumann and Jule Gregory Charney produced the first numerical weather forecast with the first programmable computer, the ENIAC (Charney et al., 1950). The journey of climate modelling took a decisive turn thanks to the key work of Edward Lorenz, who discovered in 1963 deterministic chaos in a model he developed for studying convective processes in the atmosphere (Lorenz, 1963).

Much has happened since Neumann and Charney's first weather forecast: impressive scientific and technological advances, along with the collection and availability of vast amounts of high-quality observations, led the scientific community to develop various types of highly sophisticated models, each with different levels of complexity in terms of represented processes and spatial resolution. Depending on the needs, one can choose among different types of physical models, as depicted in Figure 1.2.

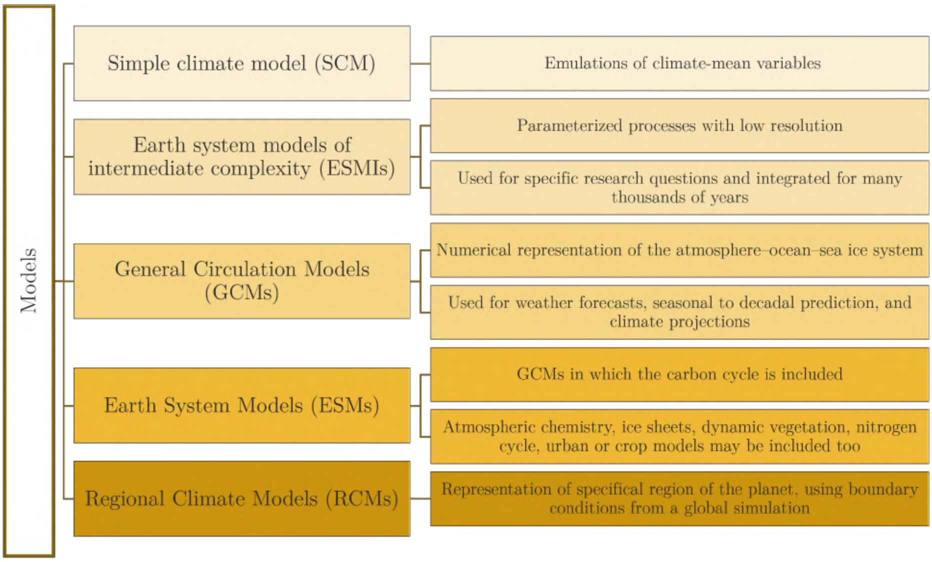

Figure 1.2: **Overview of different types of climate models.**

However, as far as complicated and detailed a single model is, it usually fails in perfectly simulating all climate processes, due to numerous issues, such as: (i) the chaotic nature of climate; (ii) the dependence on precise initial conditions (especially for short-range forecasts) and external forcings (for climate projections in particular); and (iii) the spatio-temporal multi-scale nature of the Earth system. For these reasons, scientists employ ensemble methods, such as multi-model ensembles or initial conditions ensembles, which are designed to combine the predictive strengths of each model and quantify epistemic uncertainties. For instance, the Coupled Model Intercomparison Project (CMIP) is the standard experimental framework for studying the output of coupled atmosphere-ocean general circulation models, which is now entering Phase 6 (Eyring et al., 2016).

Nevertheless, many challenges are still ahead of us. Together with the achievements concerning the physical understanding of the environmental processes, the evidences of the anthropogenic influence on climate have accumulated rapidly over the past decades. The frequency and the intensity of weather and climate extremes are increasing (Nicholls et al., 2012), resulting in major impacts on ecosystems and society. The amount of available high-quality observations corroborates the evidence of Earth's surface temperature increase due to human activities, as also clearly stated in the last assessment report of the Intergovernmental Panel on Climate Change (IPCC) (IPCC, 2023).

Despite the giant steps made in little more than a century, climate scientists are facing many open questions, which day by day become more and more pressing due to the rising impacts of climate change. Some of the most critical issues include the multi-scale and chaotic nature of climate system, tipping elements dynamics and their interactions (e.g. Greenland ice sheet, the Atlantic meridional overturning circulation, the Amazon rainforest, to name a few) (Lenton et al., 2008), the spatio-temporal dynamics and impacts of climate and weather extremes and compound events, the causal relationships between climate processes.

1.1.2 Complex climate networks

The intrinsic complex nature of climate calls for systematizing different scientific approaches and even more building new interdisciplinary frameworks: new methods are needed to complement the well established methodologies of physical modeling to broaden our general understanding of the Earth system and extreme events. In this context, alternative ways for studying the Earth system have emerged in recent years, and, among these, the use of statistical physics (Fan et al., 2021) and complex networks (Donges et al., 2009a; Ludescher et al., 2021) has drawn particular interest.

Network theory enables a good description of various real-world systems composed of many interacting dynamical units, such as food-web communities, proteins interactions, the internet, human contacts, and many others (Newman, 2003; Strogatz, 2001; Wang, 2002). The structure of the network encodes and often shapes the underlying interactions among the units, linking together structural and dynamical aspects of the studied system (Boccaletti et al., 2006).

Networks offer a promising way to study climate as well, by approximating its dynamics via a grid of low dimensional nonlinear dynamical systems. The graph topology resulting from the linear and nonlinear interactions among these sub-systems provides clues about the collective dynamics of the network. When applying networks to climate, it is crucial to establish which components represent the nodes of the climate graph and how to model the interactions between the nodes, i.e. the network links. One way is to discretize Earth's surface using a regular latitude-longitude grid, and to use the grid points as nodes to infer spatial patterns of climate variability. Another possibility is to use climate variables, processes or sub-systems as nodes, with the aim of studying their statistical relationships. The network links are then estimated via the physical laws underlying the interactions between the nodes, if known, or by measuring the degree of correlation, causation or synchronization between the interacting units. Once the network structure is established, it is possible to study its topology to get new insights into the statistical relationships and/or spatial patterns of the analysed phenomena.

Complex networks have been implemented in the climate field for about twenty years now, proving to be reliable tools to gain new insights into Earth system functioning. As pointed out by Tsonis and Roebber (2004), the climate system exhibits the properties of a small-world network, being both stable and efficient in transferring information. By applying a complex-network methodology to extreme-rainfall events, Boers et al. (2019) find two different weather systems: a regional one, characterized by short, power-law distributed connections, and a global one, where longer, super-power-law-distributed connections are responsible for a global rainfall teleconnection pattern. Another study by Stolbova et al. (2014) focuses on the configuration of a precipitation network before, during and after the Indian summer Monsoon, identifying those regions which mediate extreme precipitation patterns. Di Capua et al. (2020a) identify remote drivers of the Indian summer monsoon variability by applying causal discovery to construct climate causal effect networks. These are just few examples that show the versatility of climate networks to study several phenomena at different spatio-temporal scales.

1.1.3 Climate compound events

The primary focus of our research is weather and climate compound events. In the SREX special report (Field et al., 2012), the IPCC defines compound events as (1) *two or more extreme events occurring simultaneously or successively*, (2) *combinations of extreme events with underlying conditions that amplify the impact of the events*, or (3) *combinations of events that are not themselves extremes but lead to an extreme event or impact when combined*. Short after, Leonard et al. (2014) proposed a more general definition: *a compound event is an extreme impact that depends on multiple statistically dependent variables or events*. This latter definition emphasizes the extremeness of the impact rather than the variables or events it depends on, highlighting the necessity of multiple variables or events and the role of statistical dependence. These related extremes contribute to societal and/or environmental risk (Zscheischler et al., 2018) (see Figure 1.3).

There are several examples of climate compound events: heavy precipitations followed by floods and/or landslides, usually preconditioned by high soil water content (Berghuijs et al., 2016, 2019); droughts and heatwaves (Zscheischler and Seneviratne, 2017); high precipitations and winds, usually driven by tropical or extra-tropical cyclones (Mailier et al., 2006).

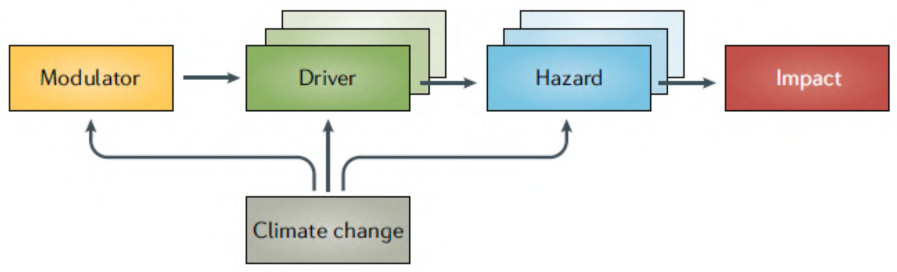

Figure 1.3: **Elements of a compound weather/climate event.** Multiple climate drivers and/or hazards potentially cause an impact. Climate modulators (e.g., the El Niño–Southern Oscillation) influence the frequency, magnitude and location of the drivers and possibly change the hazard frequency and intensity. Climate change potentially affects the modulator, the drivers and the hazards. Arrows refer to a direct causal link between the different elements (from Zscheischler et al. (2020a)).

To the best of our knowledge, most of the climate network studies have focused on the analysis of one extreme event, while very little has been done with respect to compound events. For this reason, we mainly focus on the application of climate networks to compound events. In particular, we explore the spatial and causal patterns of hot and dry extremes in the context of the European continent.

1.2 Key research questions and objectives

The general framework of our project involves the application of climate complex networks to compound events. This research addresses open questions in climate science, which we aim to tackle using our methodologies. Our focus is specifically on spatially compound extremes in Europe, along with their interactions and driving forces.

Key questions we explore include: is there a coherent structure emerging from extremes synchronizations? Can we detect this structure to enhance our understanding of the occurrence and propagation of these extremes? What are the statistical relationships between local and atmospheric variables that lead to compound events? Have these statistical relationships changed in the recent past with increasing global warming? Can we detect and quantify the causal links between the local and atmospheric variables connected to hot and dry extreme events?

We attempt to answer these questions by using climate spatially-embedded synchronization networks and causal effect networks. Consequently, we focus on four main objectives: (1) to develop a robust methodology for constructing climate networks from data, minimizing uncertainties related to link attribution; (2) to apply this methodology to uncover the spatial structures of hot and dry extremes synchronizations, thereby identifying compound hotspot regions; (3) to identify and describe the causal relationships behind hot and dry compound events through causal discovery, via causal effect networks; and (4) to identify and describe the atmospheric precursors responsible for the occurrence of hot and dry compound events.

1.3 Relevance to risk and complexity

Complex systems, as double pendulums, nonlinear circuits, the human brain, are typically constituted by a few elements or subsystems whose dynamics and interactions are nonlinear and may involve memory effects. Due to these properties, they generate rich emergent behaviors which are beyond the summation of the single subsystems' ones. Complex systems are usually characterized by chaotic dynamics and thus long-term predictions fail. The Earth system is a notable example of a large complex system. It is *large*, meaning that it is characterized by a plethora of variables and processes and, moreover, it covers a broad range of spatio-temporal scales.

Two contributions have been crucial more than others to our understanding of climate as a complex system. The first one is the the key work by Edward Lorenz, who in 1963 discovered deterministic chaos in a model he developed to study convective processes in the atmosphere (Lorenz, 1963). His findings shed light on the intrinsic limit which characterizes weather predictability, as extremely small errors in the initial state rapidly amplify, leading to large uncertainties over long prediction periods. These fluctuations are closely related to initial conditions and, assuming no external natural (e.g. volcanoes eruptions) or anthropogenic forcing (e.g. emissions in the atmosphere), constitute what is known as internal climate variability. It was Klaus Hasselmann who recognized in 1976 (Hasselmann, 1976) the role of weather fluctuations in influencing climate variability, by introducing it in his stochastic climate model. He coupled the statistically varying, short-time-scale atmospheric system to the more slowly changing components of climate. This way, he was able to explain the red-noise behavior observed in the long-term sea surface temperature anomaly data without incorporating external perturbations (Gupta et al., 2022a). Before his work, researchers used to take into account external perturbations (e.g. changes in the solar radiation and turbidity of the atmosphere), while neglecting the importance of weather fluctuations.

Climate displays a self-organizing behaviour which arises at different scales in the form of patterns of climate variability; thus, it is crucial to examine the whole system as a coherent entity to understand how order emerges from chaos, and this is one of the main tasks of complex systems science. Classical physics-based approaches can be complemented by complexity science tools to gain new understandings about the Earth system.

Together with complexity science, risk is the second conceptual pillar of our work. It is now well known that extremes are intensifying with increasing global warming (Coumou and Rahmstorf, 2012; Rahmstorf and Coumou, 2011), as reported by several studies over the last decades (AghaKouchak et al., 2020; Fischer et al., 2021; Seneviratne et al., 2021). The increase in intensity and duration of such events poses serious societal and environmental threats (Zhang et al., 2019; Yadav et al., 2023; Habibullah et al., 2022) and, moreover, single extremes could be statistically related in space and/or time, due to numerous and often nonlinear mechanisms. These events, namely *climate and weather* *compound events* (Zscheischler et al., 2020a), are associated with impacts that are larger than the sum of the single ones (Zscheischler et al., 2018), and can have devastating effects on society and ecosystems, just think of the the 2010 Russian heatwave (Hoag, 2014) or the 2018 European one (Dirmeyer et al., 2021).

We aim at improving our understanding of these phenomena, in order to be able to predict upcoming events and reveal their synchronizations structure, propagation mechanisms, and main drivers.

1.4 Thesis structure and outline

The present thesis is organized according to the aforementioned topics. In Part I we focus on the the theoretical foundations of our work, while in Part II we present our applications and results.

In Chapter 2, we introduce and describe complex network theory, with a focus on spatially embedded climate networks, discussing how these are typically constructed, their features and main applications.

In Chapter 3, we introduce causal discovery and define causal effect networks in climate. We discuss the Peter and Clark momentary conditional independence algorithm (PCMCI), which is used to retrieve causal relationships among climate variables.

In Chapter 4, we describe our first application, namely the study of meteorological droughts spatial patterns across Europe. We investigate the spatial patterns and features of meteorological droughts in Europe using event synchronization analysis. We establish robust continental networks of meteorological droughts based on the co-occurrence of these events at different locations for the period 1981-2020 and compare the results for different accumulation periods of rainfall. Each continental network is then further examined to unveil regional clusters which are characterized in terms of droughts propagation.

In Chapter 5, we extend our methodology to build evolving spatially embedded climate networks of compound hot and dry synchronizations. Focusing on the summer and winter seasons of the period 1941-2020, we highlight hotspot regions in Europe where these spatially compound extremes are increasing and analyse the atmospheric precursors driving these anomalous conditions. With this work, we bring out key aspects concerning the underlying spatio-temporal dynamics of concurrent hot and dry events.

In Chapter 6, we apply causal discovery to the study of hot and dry extremes in central Europe. In particular, we use Causal Effect Networks (based on the Peter and Clark momentary conditional independence algorithm) and show that hot extreme events in central Europe are driven primarily by anomalous atmospheric patterns and soil water deficiency, while dry extreme events are mainly induced by anomalous atmospheric patterns and soil moisture memory. Moreover, we quantify the strength of the found causal links and describe their historical trends.

Chapter 7 concludes this dissertation by summarizing the contributions of our work and outlining the challenges and future directions of this research.

Finally, Appendices A and B contain supplementary material related to Chapters 5 and 6, respectively.

Part I

Theoretical Foundations

2 Complex networks

Abstract In this chapter, we introduce complex network theory, with a focus on spatially embedded climate networks, discussing how these are typically constructed, their features and main applications. For the fundamentals of network theory (Section 2.2) we mainly refer to the book by Newman (2018) and to the review by Boccaletti et al. (2006). Spatially embedded climate networks (Section 2.3) are described following Dijkstra et al. (2019) and Fan et al. (2021).

2.1 Introduction

In 1763, the Swiss mathematician Leonhard Euler solved the problem of the Seven Bridges of Königsberg. The old capital of East Prussia, now Kaliningrad, was distinguished by seven bridges connecting four distinct areas of the city. The question was whether there existed a route that would cross each bridge exactly once (Shields, 2012; Euler, 1741). Euler realized that this problem was not related to geometry in the traditional sense - i.e., the science of measurements and distances - and no calculations were required. Instead, he categorized it under the field of *geometry of position*, laying the groundwork for topology science and graph theory. From that point onward, graph theory flourished, establishing itself as a branch of mathematics and later becoming foundational for several physics models of real-world systems.

At first, the scientific community mainly focused on the description and the properties of ordered and random graphs (Erdos and Stone, 1946; Erdos et al., 1960). In particular, the work by Hungarian mathematicians Paul Erdős and Alfréd Rényi on random graphs and their evolution played a key role in the development of graph theory (Erdos et al., 1960). It was in 1998 that Watts and Strogatz (Watts and Strogatz, 1998) recognized that the structure underlying most biological, technological, and social networks is neither entirely ordered nor completely random, but somehow lying between these two extremes (see Figure 2.1). They observed that real-world systems are characterized by a structure which can be both highly clustered, like regular graphs, and have small path lengths, being efficient in spreading information from node to node, similar to random graphs. They introduced the so called *small-world network*, showing that this model well describes various real-world systems, like western US power grid (Watts and Strogatz, 1998). As pointed out later by Tsonis and Roebber (2004) in one of the very first papers on climate networks, the climate system exhibits the properties of a small-world network as well.

Another key step towards the representation of real world processes was made in 1999 by Albert-László Barabási and Réka Albert (Barabási and Albert, 1999), who found that the distribution of the number of links per node of many large networks follows a scale-free power-law distribution. This structure is characterized by the presence of a few nodes with a high number of links, which act as central hubs. As they suggested, this type of graph typically forms when new vertices are added to a preexisting structure, preferentially attaching to already well-connected nodes.

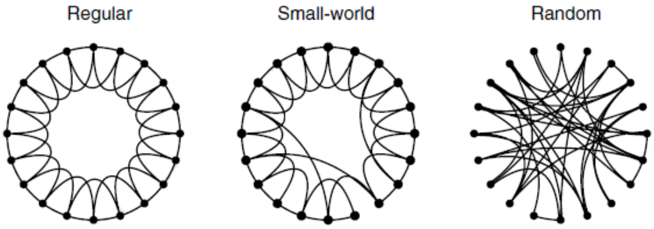

Figure 2.1: **Regular, small-world and random graphs.** From Watts and Strogatz (1998).

Nowadays, in our highly interconnected world, graphs are ubiquitous. It is difficult to imagine any real-world system composed of multiple units that cannot be conceptualized as a network. We are ourselves the units of a network of social relationships and, as biological systems, the network of biochemical reactions happening in our body (Boccaletti et al., 2006). Numerous fields have adopted the mathematical framework of graph theory to model all sort of systems and processes, included climate science. The main reason why networks are so popular is due to their versatility in modelling complex systems composed of many interacting dynamical units. Under this framework, the overlay between structural and dynamical aspect is immediately tangible. Thanks to network theory it is possible to infer the emerging properties of a system, something that is usually impossible to do by only looking at the single agents (e.g. via differential equations of their dynamics).

This Chapter is organized as follows. In Section 2.2 we touch upon the fundamentals of network theory, also describing the network measures used in our work and community detection. Section 2.3 introduces the concept of spatially embedded climate networks, describing the way these are constructed, the statistical test for significant link attribution and the correction due to spatial embedding.

2.2 Fundamentals of network theory

A network, or graph G, is a set of nodes, sometimes also referred to as vertices $v(G)$, and edges $e(G)$, also called links or connections. The nodes of a graph are used to model all sort of actors, e.g. humans in a friendships network (Eagle et al., 2009), animals in an ecological network (Montoya et al., 2006), proteins in their interaction network (Schwikowski et al., 2000), while links represent the relationships between the nodes (see Figure 2.2).

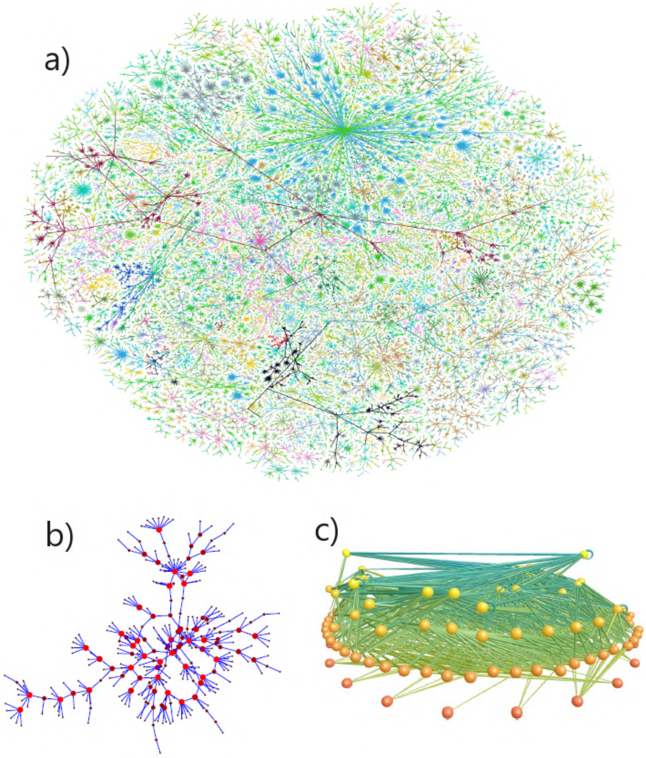

Figure 2.2: **Examples of real-world systems modeled as networks.** **a)** A visualization of the network structure of the Internet from Newman (2003). **b)** A social network of sexual contacts from Potterat et al. (2002). **c)** A food web of predator-prey interactions in a freshwater lake from Martinez (1991).

The fundamental mathematical representation of a network is the adjacency matrix $\mathbf{A}$, a $N \times N$ matrix, where N is the total number of nodes. Each row and column represents a node, and the entry A_{ij} is such that

$$A_{ij} = \begin{cases} a & \text{if there exists a link between nodes } i \text{ and } j, \\ 0 & \text{otherwise.} \end{cases} \tag{2.1}$$

In general, a is a real number which represents the strength of the connection between i and j. The simplest type of network is the undirected and unweighted graph, where the edges are simple binary connections between the nodes and no self-edges are considered, like in the example displayed in Figure 2.3a-b.

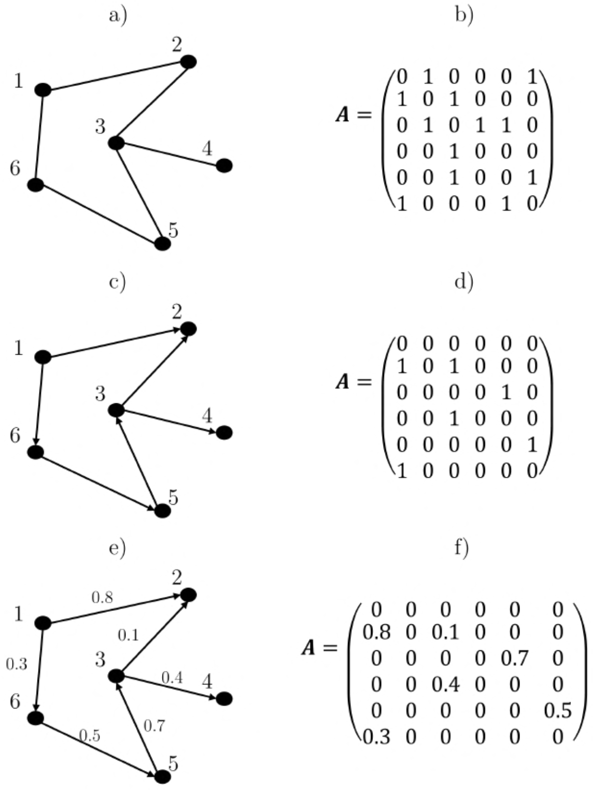

$$A = \begin{pmatrix} 0 & 1 & 0 & 0 & 0 & 1 \\ 1 & 0 & 1 & 0 & 0 & 0 \\ 0 & 1 & 0 & 1 & 1 & 0 \\ 0 & 0 & 1 & 0 & 0 & 0 \\ 0 & 0 & 1 & 0 & 0 & 1 \\ 1 & 0 & 0 & 0 & 1 & 0 \end{pmatrix}$$

$$A = \begin{pmatrix} 0 & 0 & 0 & 0 & 0 & 0 \\ 1 & 0 & 1 & 0 & 0 & 0 \\ 0 & 0 & 0 & 0 & 1 & 0 \\ 0 & 0 & 1 & 0 & 0 & 0 \\ 0 & 0 & 0 & 0 & 0 & 1 \\ 1 & 0 & 0 & 0 & 0 & 0 \end{pmatrix}$$

$$A = \begin{pmatrix} 0 & 0 & 0 & 0 & 0 & 0 \\ 0.8 & 0 & 0.1 & 0 & 0 & 0 \\ 0 & 0 & 0 & 0 & 0.7 & 0 \\ 0 & 0 & 0.4 & 0 & 0 & 0 \\ 0 & 0 & 0 & 0 & 0 & 0.5 \\ 0.3 & 0 & 0 & 0 & 0 & 0 \end{pmatrix}$$

Figure 2.3: **Graph types. a)** Undirected and unweighted network consisting of six nodes and **b)** its associated adjacency matrix. **c-d)** Same as **a**, but for a directed and unweighted graph. **e-f)** Same as **a**, but for a directed and weighted graph.

Conversely, in a directed network each edge has a direction, pointing from one node to another (Figure 2.3c-d), while a weighted network is characterized by edges having a strength, or weight (Figure 2.3e-f). In the directed case, the adjacency matrix is in general asymmetric, since the existence of an edge from i to j does not necessarily imply that there is also an edge from j to i. In our work, we employ both undirected and directed networks to model climate processes, as well as weighted and unweighted graphs.

Other types of networks include multigraphs, where more then one edge can connect two nodes (Newman, 2018); hypergraphs, where connections extend beyond pairwise interactions (Bretto, 2013; Boccaletti et al., 2023; Bianconi, 2021); and multilayer networks, where the structure is organized in different layers, each containing its own network, and interlayer edges connecting nodes in different layers (consider, for instance, a transportation network, where each layer represents the network of a different means of transport) (Boccaletti et al., 2014). All the aforementioned types of networks are categorized under the framework of static networks if their structure does not depend on time. In this case, the connections between the nodes refer to the entire time period of interest and the network essentially represents the time-averaged interactions between the components for that time period.

A special case of a multilayer network, which we employ in our studies, is the temporal or evolving network, a graph whose structure changes over time. Evolving networks are particularly suited to model real-world systems, since real structures are more often than not dynamical objects. Both the links and the nodes may change over time, with rewiring connections and nodes appearing or disappearing. The usual approach to model a dynamical system with an evolving network is to measure the structure at distinct time intervals, resulting in a sequence of snapshots of the system (Borgnat et al., 2008).

2.2.1 Network measures

In order to characterize the structure of a network, it is possible to employ several metrics which allow to study the topology at local, mesoscopic and global scales (Donges et al., 2009a). Here, we dwell on the metrics we employ in our work. For an overview of various network indices, the reader may refer to Boccaletti et al. (2006) and Newman (2018).

For an undirected network, the degree centrality k_i of node i is the number of edges connected to it:

$$k_i = \sum_{j=1}^{N} A_{ij}. \tag{2.2}$$

Despite its simplicity, the degree centrality is one of the most used of networks metrics. It measures the importance of a node at a local scale by counting its neighbours. For instance, the following table displays the degree of the nodes in Figure 2.3a:

Node i	k_i
1	2
2	2
3	3
4	1
5	2
6	2

Table 2.1: Degree centrality of the nodes in Figure 2.3a.

The study of the degree centrality has been particularly important in the development of network theory. One of the main results in the field was the identification of a unifying principle related to the degree distribution of real-world networks, denoted as $P(k)$, i.e.

the probability that a node chosen uniformly at random has degree k. In 1965, Price discovered that citation networks exhibit a scale-free degree distribution (Price, 1965). Later, Barabási and Albert showed that this scale-free, power-law distribution is typical of many real-world networks (Barabási and Albert, 1999).

For a directed network, each node has two degrees: the in-degree is the number of ingoing edges connected to a node and the out-degree is the number of outgoing edges. Following the convention that $A_{ij} = 1$ if the edge goes from j to i, the in- and out-degrees of node i are defined as follows:

$$k_i^{in} = \sum_{j=1}^{N} A_{ij}, \qquad k_i^{out} = \sum_{j=1}^{N} A_{ji}. \tag{2.3}$$

The total degree is then defined as $k_i = k_i^{out} + k_i^{in}$ and lies between -1 and 1 (if normalized). There are several others centrality measures besides the degree centrality, such as eigenvector centrality, closeness centrality, and betweenness centrality. For a comprehensive survey, please refer to Newman (2018) and Boccaletti et al. (2006).

For an undirected and unweighted network, the total number of edges m can be computed via the following:

$$m = \frac{1}{2}\sum_{i=1}^{N} k_i = \frac{1}{2}\sum_{ij} A_{ij}. \tag{2.4}$$

Given that the maximum possible number of edges is $\frac{1}{2}N(N-1)$, the fraction of links that are actually present in the graph, namely the density of the network ρ, is:

$$\rho = \frac{m}{\frac{1}{2}N(N-1)}. \tag{2.5}$$

By definition, the density lies in the range $0 \leq \rho \leq 1$. It can be seen as the probability that two random nodes in the network are connected by an edge. Depending on ρ, a graph can be dense or sparse. To formally define a sparse graph, one should check that $\rho \to 0$ as $N \to \infty$. In practice, since we only deal with finite networks, i.e. the graph has a finite number of vertices N, we say that a network is dense if ρ is close to 1, while it is sparse when $\rho << 1$.

Another useful metric for studying the structure of a network is the local clustering coefficient C_i, which is related to the concept of transitivity in a graph. This metric represents the average probability that a pair of i's neighbors are also connected to each other. It can be interpreted as the fraction of closed triangles involving node i, providing insight into the degree to which nodes tend to cluster together. It is defined as follows:

$$C_i = \frac{e(\Gamma_i)}{\frac{k_i(k_i-1)}{2}}, \tag{2.6}$$

where $e(\Gamma_i)$ is the number of existing edges in Γ_i, which is the set of neighbors of node i, and $\frac{k_i(k_i-1)}{2}$ is the maximum number of possible edges in Γ_i. The clustering coefficient lies between 0 and 1, with $C_i = 1$ meaning that i and its neighbours form a clique, and

$C_i = 0$ meaning that there are no links connecting the neighbours of i, i.e. i is the centre of a star graph with its neighbours. Since the local clustering accounts not only for the nodes it refers to but also for its immediate neighbors, it can be classified as a mesoscospic measure (Donges et al., 2009a).

2.2.2 Community detection in complex networks

Complex networks, especially if used to model real-world systems, are often characterized by the presence of community structures, or clusters. Given a graph G, a community is a subgraph G' whose nodes are tightly connected (Boccaletti et al., 2006). Broadly speaking, we can say that the average degree centrality of nodes within a community is higher than their average degree centrality with respect to the rest of the graph (Radicchi et al., 2004). Communities can reveal crucial information about a network, especially when dealing with large graphs where the underlying generating process is unknown. Community detection is generally approached as an optimization problem, since in most cases there is not a unique way to partition a graph into clusters. For instance, by applying different algorithms to Zachary's karate club network (Zachary, 1977), Cheng et al. (2014) detect different possible community structures (Figure 2.4).

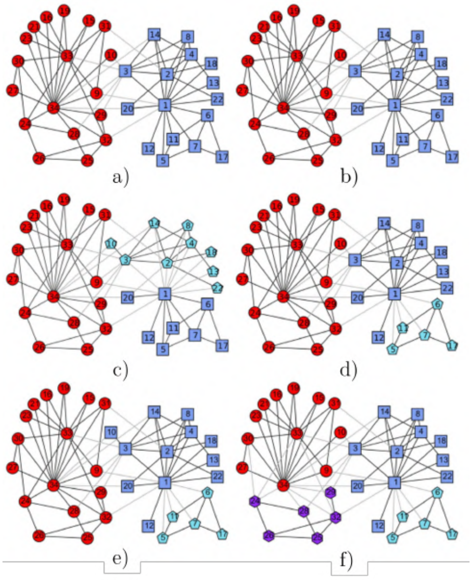
a)
b)
c)
d)
e)
f)

Figure 2.4: **Community structures in Zachary's karate club network.** **a)** The true community structure in Zachary's karate club network (Zachary, 1977) and **b-f)** the structures found by Cheng et al. (2014) using different methods. From Cheng et al. (2014).

The most widely used approach to find communities, which we also employ in our work, is based on modularity maximization. The modularity index is designed to measure if a graph is assortative, i.e. if similar nodes tend to cluster, sharing more links among themselves then with the remaining nodes. Its formulation is based on a comparison between the fraction of edged between nodes of the same type and the edges we would get if they were randomly placed.

Let us denote c_i the group node i belongs to, which is an integer $c_i = 1 \ldots M$, where M is the total number of groups. Then the total number of edges within groups is

$$\frac{1}{2} \sum_{ij} A_{ij} \, \delta_{c_i, c_j}, \tag{2.7}$$

where δ_{ij} is the Kronecker delta which equals 1 if $c_i = c_j$, i.e. nodes i and j belong to the same group.

If edges are placed at random, the expected number of links between nodes i and j depends on the number of links attached to them, which is their degrees k_i and k_j. Thus, the expected number of edges between all pairs of nodes of the same type is

$$\frac{1}{2} \sum_{ij} \frac{k_i k_j}{2m} \delta_{c_i, c_j}. \tag{2.8}$$

If we subtract 2.8 from 2.7 and normalize by the total number of edges m, we get the expression of the modularity Q:

$$Q = \frac{1}{2m} \sum_{ij} \left(A_{ij} - \frac{k_i k_j}{2m} \right) \delta_{c_i, c_j}. \tag{2.9}$$

The modularity is strictly less than 1 and takes positive values if there are more edges between nodes of the same type than we would expect by random chance. It can also assume negative values if there are fewer edges between nodes of the same type than we would expect by chance.

In community detection, the user does not know in advance which groups the nodes belong to, and identifying this partition is the task at hand. In principle, one could randomly assign nodes to groups and then check if the modularity reaches a high value. However, since there are 2^N possible divisions of a network with N nodes, it is impractical to check every possible division and select the one that maximizes modularity. Thus, in the case of community detection it is possible to find only approximate answers, i.e. partitions with high value of modularity, but not necessarily the largest overall.

Therefore, modularity maximization is performed by using heuristic algorithms, such as the Louvain algorithm (Blondel et al., 2008), which we employ in our work. The Louvain algorithm allows the division of a given graph into communities without requiring a predetermined number of groups. It works by iteratively merging nodes into groups and then merging those groups, aiming to find the partition with the highest modularity. Initially, each node is placed in its own group. Then, each node is moved into one of its neighboring communities if this change increases modularity. This process is repeated until no further modularity improvements can be made. Next, a similar round is conducted, but instead of moving individual nodes into other nodes' groups, the algorithm merges entire groups, treating them as single nodes. The same principle applies: a group is moved if doing so increases modularity. Once no further improvements in modularity are possible, the resulting configuration is considered the final partition of the graph.

The popularity of the Louvain algorithm is due to its computational speed. One round takes roughly time $O(m+N)$ because all N nodes and their neighbors have to be considered. Since the number of round can be maximum $O(log_2 N)$ (because the sizes of the groups roughly double on each round, so at most $log_2 N$ round are possible before the groups reach the size of the entire graph), the running time is about $O((m+N)log_2 N)$, which is fast enough even for very large graphs.

An important issue to consider when using modularity maximization to detect communities is the resolution limit, which is the inability to identify small communities within large networks. There are, in fact, specific examples that directly demonstrate this limitation (Lancichinetti and Fortunato, 2011). However, we apply modularity maximization using the Louvain algorithm to a large climate network (spanning the size of Europe) to identify regional communities. Therefore, we are not concerned with small clusters that may exist on a very small scale. For an overview of other types of community detection methods, see Newman (2018) and Fortunato (2010).

2.3 Spatially embedded climate networks

Networks can be classified into two types: (i) structural networks, which model existing connections between objects, whether physical (e.g., power grids, the internet, pipelines, road networks) or abstract (e.g., citation networks, social networks); and (ii) functional networks, which represent statistical dependencies between subsystems, regardless of whether the nodes are physically connected. Functional networks are used when the complete knowledge of the system is lacking, making it impossible to directly reconstruct the physical graph topology. In such cases, statistical dependencies between nodes can be measured by using observations or simulations, allowing the network structure to be inferred.

Climate networks are an example of functional networks. Starting from climate observations or model simulations, it is possible to utilize this data-driven approach to analyze, model, understand, and even predict various climate phenomena. In this section, we focus on spatially embedded climate networks, i.e. networks constructed using spatio-temporal climate dataset, wherein the nodes are distributed in space, representing the geographically localized time series on regular latitude–longitude grids, and the links are based on the statistical similarity between the time series of variables associated to different grid points. Thus, the topology of these climate networks is constrained by the geographical embedding. In essence, it is assumed that climate system dynamics can be approximated by a grid of low dimensional non-linear dynamical systems (the nodes) interacting with their spatial neighbours (via the links). The interaction between nodes can be measured, establishing the degree of correlation between any pair of nodes. We employ spatially embedded climate networks for the applications described in Sections 4 and 5.

The procedure used to construct a spatial climate network is depicted in Figure 2.5. Once the spatial domain of interest is selected (in the example of Figure 2.5 the entire

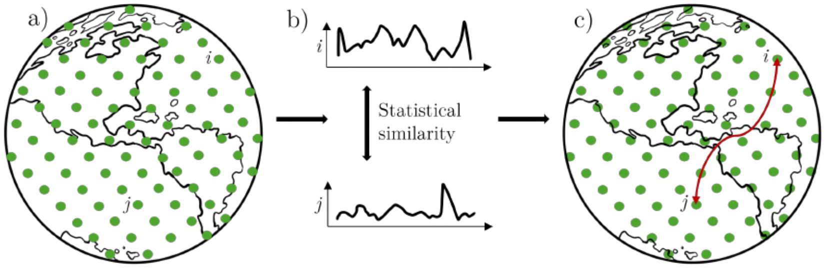

Figure 2.5: **Spatial climate network building.** **a)** The spatial domain of interest is discretized using a regular latitude-longitude grid. **b)** For each node i a time series of the variable of interest is collected and the statistical similarity for each node pair i and j is assessed. **c)** Based on the significance of the statistical similarity, a link between nodes i and j is established.

Earth), this is discretized using a regular latitude-longitude grid with a resolution of choice. The grid points serve as nodes of the climate network. In the second step, a climatological variable of interest (such as surface air temperature, geopotential height, precipitation, etc.) is selected and collected in the form of time series for every grid point, using observation data, reanalysis data or even climate model outputs. Subsequently, the interdependence between node pairs is quantified using a certain statistical similarity measure. Finally, a thresholding criterion is applied to select only those statistically significant similarities, for which a corresponding link is assigned. Notice that, depending on the purpose of the study, it is possible to attribute directed/undirected and weighted/unweighted links.

The choice of the statistical similarity measure and the statistical tests for significant links attribution are the two critical steps in climate networks reconstruction. In the next Sections 2.3.1 and 2.3.2 we cover this topics, with a focus on Event Synchronization (ES). Finally, we describe the procedure to correct network measures accounting for the spatial embedding (Section 2.3.3).

2.3.1 Statistical similarity metrics

There exist several ways to quantify the statistical similarity between time series.

The first set of methods belongs to correlation analysis. Given two time series $X(t)$ and $Y(t)$, the cross-correlation $\rho_{X,Y}(\tau)$, or Pearson correlation coefficient is defined as

$$\rho_{X,Y}(\tau) = \frac{cov(X(t),Y(t+\tau))}{\sqrt{\sigma_x^2\sigma_Y^2}} = \frac{E[(X(t)-\mu_X)(Y(t+\tau)-\mu_Y)]}{\sigma_X\sigma_Y}, \tag{2.10}$$

where $cov(X,Y)$ is the covariance of the two series, μ_X and μ_Y are their mean values, and σ_X and σ_Y their variances. The cross-correlation is a function of the lag τ and it is symmetric, meaning that $\rho_{X,Y}(\tau) = \rho_{Y,X}(\tau)$. The value of ρ is bounded between 1 and -1. In particular, 1 (-1) means perfect correlation (anticorrelation), while if $\rho = 0$ the two series are independent. An alternative to Pearson is Spearman correlation (Spearman, 1987). While Pearson correlation detects linear correlation, Spearman correlation is used to find monotonic (linear or nonlinear) relationships. Spearman correlation is a particular case of Pearson correlation, where instead of using the variables themselves, they are converted to ranks. It is defined as follows:

$$\rho_s = \frac{\sum_i (r_i - \mu_r)(s_i - \mu_s)}{\sqrt{\sum_i (r_i - \mu_r)^2}\sqrt{\sum_i (s_i - \mu_s)^2}}, \tag{2.11}$$

where r and s are the rank values of time series X and Y. Moreover, while Pearson correlation can be sensitive to outliers and it is based on the assumption that the analyzed variables are normally distributed, Spearman correlation is a non-parametric index, which does not depend on the assumption of normality. Another possible choice to detect correlation is Kendall's τ coefficient (Kendall, 1938), a non-parametric test which measures the rank correlation similarly to Spearman. Kendall's τ performs better than the Spearman coefficient for short time series (Bonett and Wright, 2000; Xu et al., 2013). Thanks to their simplicity and ease of interpretation, cross-correlation measures have been the first statistical metrics used in climate networks studies. As instance, Tsonis and Roebber (2004) apply Pearson correlation at lag 0 to build a global climate network of geopotential height at 500 hPa, while Yamasaki et al. (2008) use a lagged cross-correlation to show how the temperature network is affected by El Niño in various geographical zones around the world.

Another established measure applied to climate network reconstruction is mutual information, which is derived from information theory (Thomas and Joy, 2006). Mutual information is based on Shannon entropy H, a measure of the disorder (and thus unpredictability) of a time series, which is defined as follows:

$$H = -\frac{1}{logM}\sum_{n=1}^{M} p_n log(p_n). \tag{2.12}$$

The probability distribution is estimated from histograms of data values, using M bins, where p_n is the probability at bin n. Given two stochastic variables i and j (e.g. think of two time series), mutual information is defined as follows:

$$M(i,j) = H(i) + H(j) - H(i,j) = \sum_x \sum_y p(i,j)_{x,y} log\left(\frac{p(i,j)_{x,y}}{p(i)_x p(j)_y}\right), \tag{2.13}$$

where $p(i)$ is the probability density function of time series i, and $p(i,j)$ is the joint PDF of the pair i and j. Mutual information is non-negative and symmetric (i.e., $M(i,j) = M(j,i)$). If log base 2 is used, the units of entropy are in bits.

Mutual information quantifies linear and non-linear dependencies between the observables. If $M(i,j)$ is large, then the two time series are highly correlated or anti-correlated, but if Pearson correlation is concurrently low, it means that the relation between the variables is nonlinear. Moreover, likewise cross-correlation, it can be computed considering different time lags. Some drawbacks of mutual information include that it is always positive defined, making it difficult to distinguish between correlation and anti-correlation. In their work, Donges et al. (2009a) construct temperature climate networks using both the Pearson correlation and mutual information and compare the results on local, mesoscopic and global topological scales. They find a high degree of similarity on the local and mesoscopic scales, while larger differences are detected on the global scale. Feng and Dijkstra (2014) also apply both methods to investigate the westward propagation in the North Atlantic sea surface temperature observations, and show that mutual information performs better in capturing propagating patterns.

All the aforementioned metrics are generally applied to continuous data series to assess correlation patterns. Event Synchronization (ES), which we use in our applications described in Sections 4 and 5, is a nonlinear statistical similarity metric which allows to measure synchronizations in event-like data series. Here, with synchronization we refer to quasi-simultaneous occurrences of events. It was introduced by Quian Quiroga et al. (2002) to study brain signals synchronicity. This method is designed to treat time series characterized by spikes which can be defined as events and, in general, event series. ES was first used in climate networks science by Malik et al. (2010, 2012) to analyze spatial and temporal patterns of extreme rainfall during the Indian Summer Monsoon and it has been extensively applied in many studies (Boers et al., 2013, 2019; Agarwal et al., 2017; Gupta et al., 2022b) to treat extreme events records, whose synchronization patterns are of particular interest due to their potential impact on ecosystems and society.

The degree of synchronicity among nodes i, j is measured based on the number of quasi simultaneous events occurrences between the associated event series (see Figure 2.6).

Event l occurring at i at time t_l^i is considered to be synchronized with event m occurring at j at time t_m^j if $0 \leq t_l^i - t_m^j \leq \tau_{lm}^{ij}$, where

$$\tau_{lm}^{ij} = min\{t_{l+1}^i - t_l^i, t_l^i - t_{l-1}^i, t_{m+1}^j - t_m^j, t_m^j - t_{m-1}^j, t_{max}\}/2. \tag{2.14}$$

It is possible to set t_{max} to an arbitrary value to ensure that only concurrences developing in a predefined time window are counted as synchronizations. A score J_{lm}^{ij} is assigned to every events pair l and m according to the following rule:

$$J_{lm}^{ij} = \begin{cases} 1, & \text{if } 0 < t_l^i - t_m^j \leq \tau_{lm}^{ij} \\ 1/2, & \text{if } t_l^i = t_m^j \\ 0, & \text{otherwise.} \end{cases} \tag{2.15}$$

Finally, the number of times an event at i is synchronized with an event at j is counted:

$$C(i|j) = \sum_{l=1}^{S_i} \sum_{m=1}^{S_j} J_{lm}^{ij}, \tag{2.16}$$

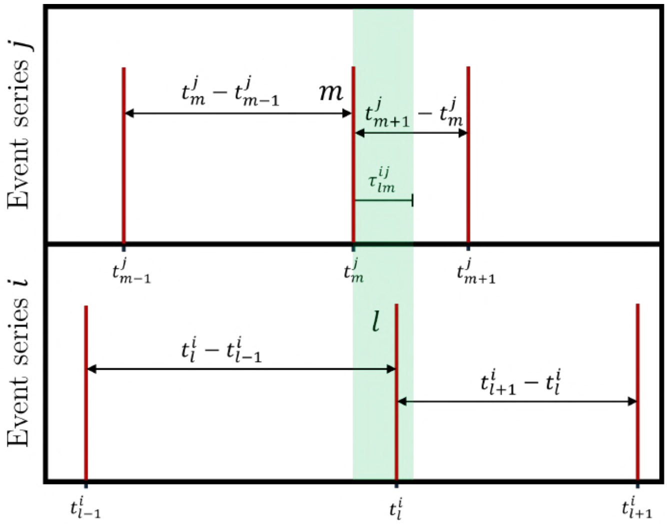

Figure 2.6: **Schematic representation of Event Synchronization.** In this example, event l is synchronized with event m because $0 \leq t^i_l - t^j_m \leq \tau^{ij}_{lm}$.

where S_i and S_j are the total number of events in i and j, respectively. The index C is used to obtain he symmetrical and anti-symmetrical combinations $Q(i, j)$ and $q(i, j)$:

$$Q(i,j) = \frac{C(i|j) + C(j|i)}{\sqrt{S_i S_j}}, \qquad q(i,j) = \frac{C(i|j) - C(j|i)}{\sqrt{S_i S_j}}, \tag{2.17}$$

which are used to measure the synchronization of the events and their delay behavior, respectively. They are normalized to $0 \leq Q(i, j) \leq 1$ and $-1 \leq q(i, j) \leq 1$. If several extreme events are very close in one record, then only the first one is considered.

The symmetrical score is suited to construct undirected networks, and $Q(i, j) = 1$ if and only if the events of the signals are fully synchronized. The anti-symmetrical one contains the additional information of the overall direction of the synchronicity between i and j: if there is a majority of events happening at i after they appear at j compared to how many develop at j after taking place at i, then q_{ij} will be positive, with link direction from j to i. Vice-versa, the sign will be negative, with direction of the link from i to j. The value of the anti-symmetrical score represents the percentage of times the j's events precede i's (or vice-versa, depending on the sign), and serve as weight of the link. It can be interpreted as the frequentist probability of observing an event happening at i given that an event has happened at node j.

Since the maximum time lag τ^{ij}_{lm} is specific to each event pairs and it is dynamically computed, there is no need to set it a priori (Quian Quiroga et al., 2002), which makes ES time-scale adaptive and therefore, preferable in applications to real data where there is no validated knowledge about the relevant time scales. Unlike correlation metrics and mutual information, ES can be applied in an anti-symmetric fashion to construct directed climate networks (see our application in Section 4).

However, it must be noted that these correlation and synchronization coefficients do not provide any physical information about the studied relationships. Therefore, it is necessary to carefully interpret the results in a physical sense in order to get valuable insights about the analyzed system. Moreover, the aforementioned methods are not designed to assess causality: as we explain in Section 3, there exist other methods to apply causal analysis in conjunction with complex networks, which we apply in Section 6.

2.3.2 Link attribution

Once the statistical similarity between every node pair is established, only those connections that are statistically significant are kept to attribute links.

Generally, to test whether an observed value x is significant, one can check if $|x-\mu| > n\sigma$, assuming that the data are sampled from a normal distribution with mean μ and standard deviation σ and tuning n based on how strict the significance criterion should be. However, many natural phenomena and their correlations do not follow a normal distribution, and thus it is not immediately possible to estimate μ and σ from the data.

Hence, a more appropriate approach is to test the significance against surrogate data, which are used to build a null model of correlation/synchronization values without making any assumption on the background distribution. Surrogates can be generated via different methodologies (see Lancaster et al. (2018) for a complete overview). The random shuffle technique is a model-free approach, according to which surrogates are generated from random permutations of the original data, preserving their probability distribution and destroying internal correlations. Other methods include Fourier surrogates (which preserve the auto-correlation of the original data but destroy the probability distribution), the amplitude adjusted Fourier transform (which preserves both the auto-correlations and the probability distribution, but it is time consuming and requires long enough time series), and bootstrap surrogates, which is similar to simple random shuffling, except the data are permuted in blocks (see section 5). In all these cases a significant threshold α must be selected to filter out non-significant correlations.

Considering a correlation (or synchronization) $N \times N$ matrix $\mathbf{S}$, the significant test to determine the adjacency matrix $\mathbf{A}$ is:

$$A_{ij} = \mathcal{H}(S_{ij} - \theta), \tag{2.18}$$

where A_{ij} is an entry of the adjacency matrix, S_{ij} is the observed value of correlation between i and j, $\mathcal{H}$ is the Heaviside function, and θ is the correlation threshold corresponding to the significance level α.

The choice of θ is based on a trade-off between the statistical significance of links and the richness of network structure to be revealed. In particular, it is desirable to include long distance links with high similarity/interaction value which are responsible for many interesting and non-trivial features of climate networks, such as the small world property or hubs, and may potentially be associated with teleconnections. It is also possible to choose W in order to construct a network with a desired density ρ, which can be useful for maintaining consistency across different networks when comparing their structures.

Climate networks of this kind are built by performing multiple statistical tests on the same set of observations. Therefore, it is crucial to account for a non-negligible false discovery rate. False discovery rate can be corrected by using several approaches, like the Bonferroni (Benjamini and Hochberg, 1995), the Benjamini-Hochberg (Benjamini and Yekutieli, 2001), or the Storey's method (Storey, 2011). We use a statistical significance test based on surrogates and false discovery rate correction in our work described in Section 5.

Links can be also attributed by using other approaches. For instance, one may be interested in preserving those connections which are robust in time, as we do in our work described in Section 4, where more details can be found.

2.3.3 Correction due to spatial embedding

A key issue concerning spatially embedded graphs is that the spatial patterns displayed by any network measure might depend on the artificial boundaries arbitrarily introduced when setting the domain of the study. These boundaries cut all the possible links that would connect the considered grid points with regions which are not included in the analysis. This artificially reduces the degree of the nodes and the number of long links, and also influences the spatial patterns of any other network measure. This cause the emergence of boundary effects which artificially modify the spatial patterns of every network measures and thus it is necessary to correct their impacts. Boundary effects depend on the distribution of link lengths and on the network measures themselves. For instance, as more links are cut for nodes closer to the boundaries than those deep inside the region, the degree of the nodes near to the boundaries has a stronger reduction compared to those in the interior.

Following the work by Rheinwalt et al. (2012), it is possible to correct network measures by constructing spatially embedded random networks (SERNs) surrogates, whose links are assigned based on the probability of observing a link of the same length in the original graph. Afterwards, the boundary effects for a certain network index are estimated using the average of that specific network measure over the SERNs. The corrected measure is finally obtained by dividing the original index by the corresponding average one of the SERN surrogates, node-wise. The corrected measure represents the value of the network index relative to the expected value from the spatial embedding, and thus it is dimensionless.

3 Causal networks

Abstract In this chapter, we introduce causal discovery, a methodological framework based on Granger causality which is used to detect causal links among climate variables. Next, we outline the assumptions underlying causal discovery and subsequently we introduce time graphs and causal effect networks. The final section discusses the Peter and Clark momentary conditional independence algorithm, which we apply in our work.

3.1 Introduction

One of the most critical challenges in science is finding reliable methods to uncover causal relationships among variables. Experiments are extremely helpful if the system under study can be fully reproduced and controlled. However, more often than not, conducting active experiments is not feasible due to the complexity of the phenomena being analyzed. Today, we are witnessing the massive growth of data availability, thanks to the collection of vast amounts of observations in the form of time series data. This is particularly true for the Earth system, whose processes are continuously monitored with refined spatio-temporal resolution, especially with the advent of satellite data (Hollmann et al., 2013; McCain et al., 2006). Moreover, computational resources are rapidly improving, enabling the efficient processing of massive amounts of data. As a result, it is now possible to infer causal relationships directly from high-quality observations, without the need to conduct experiments. Of course, this requires a deep understanding of the system under study and a robust statistical framework to assess the significance of the identified relationships.

Although being a well established and known tool to study time series relationships, correlation analysis fails in identifying causality and thus different methods have emerged to perform causal discovery from observational time series. Two time series can appear to be correlated even though there is no causal relationship among them. This typically happens because of three main reasons (see Figure 3.1): (i) the presence of autocorrelation in one or both variables; (ii) the presence of a common driver; (iii) the presence of indirect links (Runge et al., 2014; McGraw and Barnes, 2018). Causal discovery tools can help identify and remove spurious correlations, retaining only causal connections.

Here, we refer to causal link as defined by Granger causality (Granger, 1969), i.e. a relationship between two processes $X_0 \longrightarrow X_1$ such as a change in X_0 has a direct effect

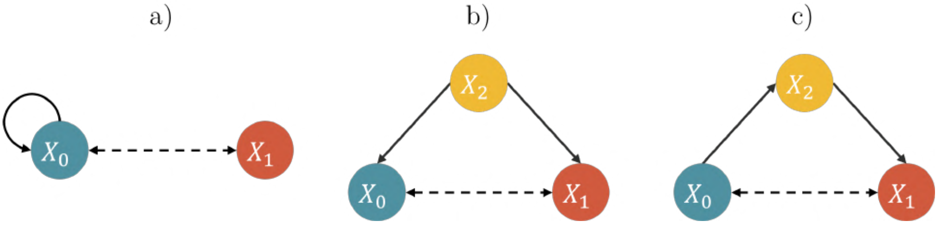

Figure 3.1: **Common causes of spurious relationships.** **a)** The connection between X_0 and X_1 is due to the autocorrelation of process X_0. **b)** Processes X_0 and X_1 are connected with a spurious link due to the presence of the common driver X_2. **c)** Processes X_0 and X_1 are connected with a spurious link due to the presence of the intermediate process X_2.

on X_1. This definition is based on two main assumptions: (1) the cause occurs before the effect; and (2) the cause contains information about the effect that is unique, and is in no other variable (Granger, 2004). This sense of causality builds upon the notion of incremental predictability (Hlaváčková-Schindler et al., 2007).

The standard test for (bivariate) Granger causality is based on linear regression:

$$X_1^t = \sum_{k=1}^{L} \beta_{1k} X_1^{t-k} + \sum_{k=1}^{L} \beta_{0k} X_0^{t-k} + \xi^t, \tag{3.1}$$

where ξ^t are uncorrelated random variables with zero mean and variance σ^2, L is the number of considered time lags, and $t = L + 1, \ldots, N$. If any of the coefficients β_{0k} is different from zero, then we say that X_0 Granger causes X_1 at lag k.

Granger causality has also been extended to nonlinear measures. However, regardless of the specific method used, the test to assess whether two processes X_0 and X_1 are causally linked is based on conditional independence testing, according to the following:

$$X_0 \not\perp\!\!\!\perp X_1 | X_2 \iff I(X_0, X_1 | X_2) \neq 0, \tag{3.2}$$

which reads X_0 and X_1 are not conditionally independent given X_2 if and only if the conditional dependence measure I is different from 0. Notice that in the bivariate case, X_2 stands for the past of either processes X_1 or X_0 (depending on which one is tested as the driver and which one as the response), while in the multivariate framework, it includes other variables as well.

A notable extension of linear Granger causality is transfer entropy (Schreiber, 2000). Transfer entropy is closely related to information theory, being an alternative formulation of conditional mutual information. While mutual information is a measure of general statistical dependence to quantify linear and nonlinear dependencies between variables (see Section 2.3.1), conditional mutual information (and thus transfer entropy) can be used to detect causality. Let us consider processes X_0, X_1 and X_2, where $H(X_i)$ is the Shannon entropy of process X_i, $H(X_i, X_j)$ is the joint Shannon entropy and $H(X_i|X_j)$ is the conditional Shannon entropy. Then, the conditional mutual information $CM(X_0, X_1|X_2)$

between random variables X_0 and X_1 given X_2 is defined as

$$\begin{aligned} CM(X_0, X_1|X_2) &= H(X_0|X_2) + H(X_1|X_2) - H(X_0, X_1|X_2) = \\ &= \iiint p(x_0, x_1, x_2) log\left(\frac{p(x_0, x_1|x_2)}{p(x_0|x_2)p(x_1|x_2)}\right) dx_0 dx_1 dx_2. \end{aligned} \tag{3.3}$$

As we can see, conditional mutual information is based on conditional independence testing as well. This framework is based on several assumptions and it is necessary to systematize it with a suitable algorithm in order to apply it to real datasets. We discuss these aspects in the remainder of this Chapter. In Section 3.2 we describe the assumptions of causal discovery from observational time series. In section 3.3 we define time series graphs and causal effect networks. Finally, in Section 3.4 we introduce the Peter and Clark momentary conditional independence algorithm, which we apply to detect causal relationships in our work described in Section 6.

3.2 Assumptions of causal discovery from observational data

Causal discovery lays on the assumptions under which the underlying causal dependencies can be inferred from observational data. Notice that in our case the data are in the form of time series, which implies that the causal relationships can only point forward in time and not backwards. Other assumptions include causal sufficiency, the causal Markov condition, faithfulness, stationarity, instantaneous effects, and any additional assumptions specific to the statistical method used for conditional independence testing (Runge, 2018). This set of assumptions is reviewed in the following. For a more in-depth overview, we refer the reader to Runge (2018).

3.2.1 Causal sufficiency

In order to get reliable results within the framework of causal discovery, the linkage among variables X_0 and X_1 should be tested conditioned on every other possible variable. In other words, one must be sure that all relevant variables have been included in the conditional independence test, otherwise spurious links may result from the analysis. For instance, suppose that X_2 is a common driver of X_0 and X_1, as depicted in Figure 3.1b. If X_2 is not included in the variables set, then the dependence among X_0 and X_1 can not be tested conditioned on X_2, and thus these two variables will share a statistically significant causal link even if they are simply correlated. For this reason, we must guarantee that there exist no unobserved (or latent) variable that directly or indirectly influences any other quantity in our dataset (Spirtes et al., 2001).

Causal sufficiency can be violated if some unobserved variable exists or even if the time sampling of the variables is sub-optimal. Thus, in order to be sure that all relevant actors in a specific system are accounted for with a proper resolution, it is important to approach causal discovery with an expert knowledge of the system under study. It is essential to combine such framework with explicit hypothesis on the type of physical relationships expected, choosing the right set of variables, parameter settings, timescale and mathematical relationship.

3.2.2 Causal Markov condition and faithfulness

The causal Markov condition and faithfulness establish a close relationship between the analysed processes and their time series graph (see next Section 3.3).

The causal Markov condition prescribes that if nodes A and B are separated (i.e. there is no path in the graph which connects them), then the corresponding processes at A and B are independent, i.e.

$$A \bowtie B|S \Rightarrow X_A \perp\!\!\!\perp X_B|X_S. \tag{3.4}$$

This includes its contraposition

$$X_A \not\perp\!\!\!\perp X_B|X_S \Rightarrow A \not\bowtie B|S. \tag{3.5}$$

which reads if X_A and X_B are not conditionally independent given X_S, which is the set of all other variables, then the corresponding nodes A and B are connected.

Faithfulness complements the causal Markov conditions by prescribing that if processes X_A and X_B are independent then A and B are separated in the graph

$$X_A \perp\!\!\!\perp X_B|X_S \Rightarrow A \bowtie B|S, \tag{3.6}$$

and the contraposition according to which from connectedness follows dependence

$$A \not\bowtie B|S \Rightarrow X_A \not\perp\!\!\!\perp X_B|X_S. \tag{3.7}$$

Both conditions constitute important assumptions for causal discovery algorithms, as discussed in Spirtes et al. (2001). Intuitively, faithfulness together with the causal Markov condition allow us to conclude that a measured statistical dependency is actually due to some (not necessarily direct) causal mechanism and, conversely, a measured independence (given any set of conditions) implies that no direct causal mechanism exists (Runge, 2018).

3.2.3 Stationarity

The assumption of stationarity requires that the causal links among the variables remain constant over time. Thus, causal links are estimated from the entire time series, resulting in a set of relationships that do not change over time. Note that this differs from assuming the processes themselves are stationary— indeed, it is possible for the statistical properties of the time series to vary, while the causal links remain unchanged. If this assumption does not hold for the entire period, the time series can be divided into blocks to analyze how the causal links evolve over time, provided they remain constant within each block and that the original series is long enough for such division.

3.2.4 Instantaneous effects

As prescribed by Granger causality, the causal relationships are directed in time and imply that the cause occurs before the effect. Thus, this methodology does not contemplate the possibility of instantaneous effects. Notice that instantaneous does not mean immediate, i.e. at light speed, but it indicates that the effect evolves on a timescale which is shorter than the time resolution at which the time series are sampled. Therefore, in order to be sure that the assumption regarding the absence of instantaneous effect is realistic, it is crucial to sample the process with sufficient resolution. Notice that there exist some causal discovery algorithms which allow for the identification of instantaneous links, for instance in Runge (2020), but here we apply causal discovery without the possibility of having such links.

3.2.5 Additional assumptions

As previously said, causal discovery is performed by applying test 3.2 using a conditional dependence measure I of choice. Therefore, each specific measure I implies further assumptions on the detected causal relationships.

The most common statistical methods are often based on the assumption of linearity, which has the advantage of being computationally simple and easy to interpret. Nonlinear mechanisms can also be captured using more advanced techniques, which do not require any model assumptions. There are primarily two approaches to conditional independence testing: regression-based and model-free methods.

Regression-based conditional independence tests are based on first regressing out the influence of X_2 from X_0 and X_1 and then testing the dependence between the residuals, according to the following:

$$\begin{aligned} X_0 &= f_{X_0}(X_2) + \xi_{X_0}, \\ X_1 &= f_{X_1}(X_2) + \xi_{X_1}, \end{aligned} \tag{3.8}$$

where ξ_{X_0,X_1} are i.i.d. From the estimated f_{X_0} and f_{X_1}, it is possible to find the residuals

$$\begin{aligned} r_{X_0} &= X_0 - f_{X_0}(X_2), \\ r_{X_1} &= X_1 - f_{X_1}(X_2). \end{aligned} \tag{3.9}$$

The causal dependence between X_0 and X_1 is therefore checked by statistical tests between the residuals r_{X_0} and r_{X_1}.

The functional form of f_{X_0,X_1} has to be decided based on the assumptions made on the causal relationships. For instance, it is possible to assume linearity and use a simple partial correlation test (Runge et al., 2015), or it is possible to use non-parametric regressions (Rasmussen and Williams, 2006; Runge et al., 2019). It is also possible to use model-free methods to test the conditional independence, as done with conditional mutual information (3.3). Moreover, the dependence between the residuals r_{X_0} and r_{X_1} can be tested with different pairwise association tests. For partial correlation this is a t-test, while the dependence between the residuals of a non-parametric regression can be tested with non-parametric tests (Székely et al., 2007; Gretton et al., 2007). If it is possible to assume linearity, at least in a first order approximation, then linear partial correlation is a suitable metric to perform causal discovery, as it is done in our study described in Section 6.

3.3 Time series graphs and causal effect networks

The causal dependencies of a multivariate process $\mathbf{X}$ can be visualized by using graph models. In our specific case, since the processes are structured in the form of time series, a suitable choice of a graph model is the time series graph. In a time series graph, the set of nodes consists of all the components of the involved processes at each time step t. The links are the causal dependencies among the processes and are directed forward in time, as it is not possible to define a causal relationship in which the cause follows the effect. In principle, such graph should be infinite in time, but because of the stationarity assumption, it can be defined up to a certain time lag τ_{max}, only depending on the timescale at which the causal dependencies (are supposed to) develop.

In general, we say that variables $X_i^{t-\tau}$ and X_j^t (also referred to as actors) are connected by a lag-specific directed link if and only if

$$X_i^{t-\tau} \not\perp\!\!\!\perp X_j^t | \mathbf{X}^{\mathbf{t}}_{\mathbf{past}} \setminus X_i^{t-\tau}, \tag{3.10}$$

i.e., if they are not statistically independent given the past of the whole process $\mathbf{X}^{\mathbf{t}}_{\mathbf{past}}$ minus the cause variable $X_i^{t-\tau}$.

The parents of actor X_j^t are defined as

$$\mathcal{P}(X_j^t) = \{X_k^{t-\tau} : X_k \in \mathbf{X}, \tau > 0, X_k^{t-\tau} \to X_j^t\}. \tag{3.11}$$

For instance, let us consider the following multivariate process composed of three variables X_1, X_2 and X_3

$$\begin{cases} X_1 = \beta_1 X_1^{t-1} + \beta_2 X_3^{t-1} + \xi^t_{X_1} \\ X_2 = \beta_3 X_1^{t-1} + \beta_4 X_2^{t-1} + \xi^t_{X_2} \\ X_3 = \beta_5 X_3^{t-1} + \xi^t_{X_3} \end{cases}. \tag{3.12}$$

The time series graph corresponding to process 3.12 is depicted in figure 3.2. From the time graph we immediately see that the parents of actor X_1 are X_3^{t-1} and X_1^{t-1}, since direct causal links point from X_3^{t-1} and X_1^{t-1} to X_1.

The information provided by the time series graph can be condensed in a causal effect network. In this type of depiction, the nodes represent the different processes, and are connected by the causal link relative to a certain time lag. For instance, the causal effect network corresponding to process 3.12 and time series graph 3.2 is shown in Figure 3.3.

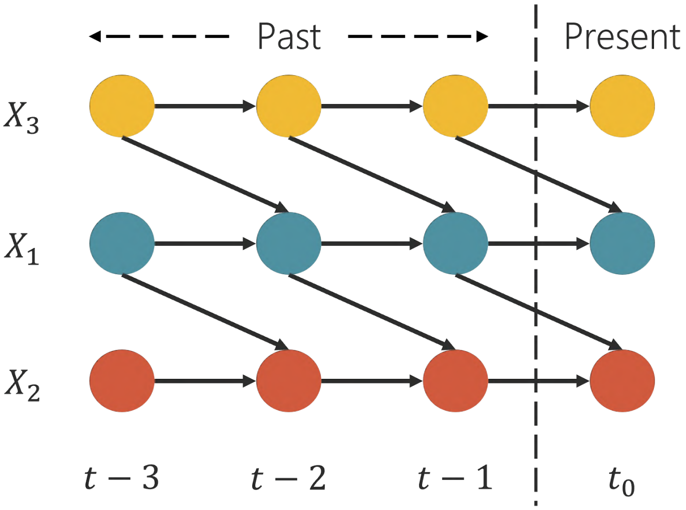

Figure 3.2: **Example of a time series graph.** Time series graph corresponding to the multivariate process 3.12.

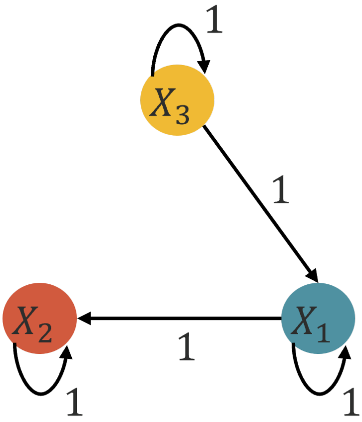

Figure 3.3: **Example of a causal effect network.** Causal effect network corresponding to the multivariate process 3.12. The number attached to each link represent the lag at which the causal relation takes place. The link arrows can be colored according to their strength β.

3.4 The Peter and Clark momentary conditional independence algorithm

The final objective of any causal dependence measure is to find a set of causal parents $\mathcal{P}$ for each actor X_i^t of the multivariate process $\mathbf{X}$ with N processes and $i = 1, ..., N$.

The set of parents is determined through iterative independence testing among the variables, analyzing different time lags. In practice, since time series are finite, the maximum time lag considered for the analysis is selected based on physical reasoning about the system under study.

The Peter and Clark Momentary Conditional Independence (PCMCI) algorithm is a two-step method based on a modified version of the Peter and Clark (PC) scheme (Spirtes et al., 2001; Runge et al., 2014, 2019). Compared to the PC algorithm, PCMCI is designed to deal with autocorrelation and high-dimensional sets of actors (Runge et al., 2019).

The PC step is a condition selection stage designed to identify a provisional set of causal parents $\hat{\mathcal{P}}(X_i^t)$ for every X_i^t via iterative independence testing at a certain significance threshold α. In the following, we describe the algorithm steps with linear partial correlation used as causal dependence measure:

1. Unconditional correlation check: for every considered lag τ and every pair i, j, the algorithm first checks if the unconditional cross correlation $\rho(X_j^{t-\tau}; X_i^t)$ is significant. If this is the case, a causal path between the two variables is inferred, though it may not necessarily be direct.

2. Conditional correlation with one condition: the algorithm tests the significance of the conditional cross-correlation $\rho(X_j^{t-\tau}; X_i^t | X_i^{t-1})$. However, this test is not performed for each possible condition, meaning that not all actors $\mathcal{X} \setminus \{X_j^{t-\tau}\}$ are used as a condition, but only those with the strongest absolute correlation with X_i^t. For this reason, the algorithm converges very quickly compared to a full conditional independence test (Runge et al., 2019).

3. Progressive conditional independence testing: the conditional independence test is repeated by progressively increasing the number of conditioning variables. This continues until the number of possible causal parents equals or exceeds the number of conditions required to calculate the next partial correlation. At this stage, if the cross-correlation between X_i^t and $X_j^{t-\tau}$ is still significant, $X_j^{t-\tau}$ is identified as a provisional parent of X_i^t: $X_j^{t-\tau} \in \hat{\mathcal{P}}(X_i^t)$.

At the end of the PC step, each actors has its own set of provisional parents.

The objective of the second MCI stage is to get a definitive set of parents for each actor. This is done by verifying whether an actor and each of its provisional parents are still conditionally dependent given both their set of parents:

$$X_j^{t-\tau} \not\perp\!\!\!\perp X_i^t | \mathcal{P}(X_i^t) \setminus \{X_j^{t-\tau}\}, \mathcal{P}(X_j^{t-\tau}). \tag{3.13}$$

The condition $\mathcal{P}(X_i^t) \setminus \{X_j^{t-\tau}\}$ is sufficient to establish conditional independence, while the additional condition on the lagged parents $\mathcal{P}(X_j^{t-\tau})$ accounts for the possible presence of autocorrelation in the driver actor (Runge et al., 2019). The significance of the definitive causal links is based on the p-values of the MCI test.

Finally, it is possible to construct a causal effect network by using standardized multiple regression of each actor onto its causal parents identified via PCMCI (Kretschmer et al., 2016). In this case, the strength of a causal link $X_i^{t-\tau} \to X_j^t$, which we call β, represents the change in standard deviation units of node X_j^t due to an increase of 1 standard deviation of $X_i^{t-\tau}$, with all other actors constant.

Part II

* * *

Applications

4 Meteorological droughts spatial patterns across Europe

Adapted from *Giaquinto, D., Marzocchi, W., and Kurths, J.: Exploring meteorological droughts' spatial patterns across Europe through complex network theory, Nonlin. Processes Geophys., 30, 167–181, https://doi.org/10.5194/npg-30-167-2023, 2023.*

Abstract In this study we investigate the spatial patterns and features of meteorological droughts in Europe using concepts and methods derived from complex network theory. Using event synchronization analysis, we uncover robust meteorological drought continental networks based on the co-occurrence of these events at different locations within a season from 1981 to 2020 and compare the results for four accumulation periods of rainfall. Each continental network is then further examined to unveil regional clusters which are characterized in terms of droughts geographical propagation and source–sink systems. While introducing new methodologies in general climate network reconstruction from raw data, our approach brings out key aspects concerning drought spatial dynamics, which could potentially support droughts forecast.

4.1 Introduction

Droughts are among the most severe climate extremes, negatively affecting environments as well as societies and economies (Taufik et al., 2017; Feng et al., 2021; Doughty et al., 2015; Walthall et al., 2013). As reported by the World Meteorological Organization (WMO, 2021), they were one of the most impactful natural hazard in terms of human losses during the period 1979–2019, accounting for 34% of disaster-related deaths. To make matters worse, droughts are expected to grow and become more severe in the near future due to human-related climate change (Spinoni et al., 2021). Additionally, although different drought types respond differently to increasing greenhouse gas concentrations and distinctions among geographic regions should be made, there is high confidence that water stress is increasing globally according to the Sixth Assessment Report of the Intergovernmental Panel on Climate Change (IPCC) (Wehner et al., 2021).

Despite the high scientific interest and effort towards a better understanding of this crucial topic, there are still substantial discrepancies concerning the assessment of droughts trends for specific regions. As for Europe, significant impacts have been extensively reported over the years, e.g., on ecosystems (Bastos et al., 2020), economy (Naumann et al., 2021), and agriculture (Beillouin et al., 2020). This climate phenomenon is closely monitored and studied both under present and future climate conditions (Spinoni et al., 2016; Marinho Ferreira Barbosa et al., 2021). When it comes to future scenarios, some studies claim that the entire continent will suffer under the increase of droughts' frequency and severity (Spinoni et al., 2018; Cook et al., 2020). Others are more cautious in drawing such a conclusion, pointing to the critical role of internal climate variability and associated uncertainties (Zhao and Dai, 2017; Vicente-Serrano et al., 2021). There are multiple reasons for these incongruences.

First of all, droughts are characterized by ample spatial variability (Vicente-Serrano et al., 2021): subcontinental or sometimes even subnational areas behave discordantly than their neighbors, and different studies place emphasis on different territories (Spinoni et al., 2016; Vicente-Serrano et al., 2021; Spinoni et al., 2018; Böhnisch et al., 2021). In addition, we lack a unique and standardized definition of regions: each scientific team outlines the subcontinental area of interest discretionally, following political or economic boundaries, according to the obtained results, or using external classifications (Spinoni et al., 2016, 2015a, 2018). Although they are completely understandable procedures, they make comparisons among studies difficult, if not unfeasible.

On top of that, there is not a unique definition of drought. Depending on causes and impacts, droughts are classified into different types, i.e., meteorological, agricultural, hydrological, and economic (Wilhite and Glantz, 1985; Seneviratne et al., 2012). These typologies are characterized by an increasing level of complexity, with impacts ranging from atmosphere to land, ecosystems, and even social and economic systems: an absolute definition could result in a misleading oversimplification (Lloyd-Hughes, 2014). Numerous indices have been proposed to classify, monitor, and assess this complex climate event (Wei et al., 2021). Some are defined in terms of anomalies of a single variable, while, for the most complicated cases, multiple atmospheric variables are taken into account (Marinho Ferreira Barbosa et al., 2021). Each of them has its strengths and limitations (Mishra and Singh, 2010; Zargar et al., 2011; Wei et al., 2021; Mukherjee et al., 2018), behaving differently when it comes to projections of future climate scenarios (Böhnisch et al., 2021; Vicente-Serrano et al., 2021). Using a hydrological and water-use model, Naumann et al. (2021) conclude that hydrological droughts' damage in Europe could strongly increase with global warming and cause a regional imbalance in future impacts. On the other hand, Vicente-Serrano et al. (2021) show that trends of meteorological droughts over western Europe are statistically non-significant from a long-term perspective.

Finally, the reference period used to identify the anomalies of the drought variable of interest, be it precipitation, soil humidity, or streamflow, etc., represents another important source of inhomogeneity between different studies (Spinoni et al., 2017). Just as an example, Vicente-Serrano et al. (2021) use the period 1871–2018 to compute the Standardized Precipitation Index (McKee et al., 1993), while Spinoni et al. (2018) choose

1981–2010 to compute the frequency of drought events.

In this study we focus on meteorological droughts, defined as a period with a precipitation deficit in relation to the long-term average condition for a given region. Being simply related to precipitation, meteorological droughts are the basis for every other drought class. A lack of precipitation may be the first precursor of soil humidity's reduction (agricultural drought) as well as the cause of streamflow shortage (hydrological drought) (Bevacqua et al., 2021).

The approach we propose in this study is based on complex networks, and it is designed to address some of the criticalities described before, while detecting unknown spatial features of European meteorological droughts. Complex networks have been applied for many different purposes, e.g., to study social dynamics, power grids, and epidemics. They are a powerful tool in systems composed of many units, where the interactions' structure is closely linked to system's dynamics (Boccaletti et al., 2006). Over the last 2 decades, complex network theory has been successfully applied to climate science too, proving to be an efficient method both to deepen our general understanding of various complex climate processes and to predict the occurrence of extremes (Boers et al., 2019; Tsonis et al., 2006; Ludescher et al., 2021). Complex networks have been applied to droughts too. Ciemer et al. (2020) developed a forecasting scheme to predict the occurrence of meteorological droughts in the Central Amazon basin, while Konapala et al. (2022) develop a method to assess droughts' propagation in North America.

Our main objective here is to uncover spatial features of meteorological droughts in Europe, highlighting underlying mechanisms and patterns which could potentially support drought's forecast in the future. We aim at distinguishing regions in Europe whose main feature lies in drought occurrence and propagation's coherence. Identifying such territories could be of a great importance to further investigate this phenomenon within those areas where its characteristics are homogeneous. Indeed, droughts display a high spatial and temporal variability, and it is thus fundamental to study their evolution accounting for these irregularities to possibly lower uncertainties. Furthermore, with our model we are able to describe the average historical patterns in droughts' evolution which could be a starting point for future climate studies to identify the spatial tracks that are followed by this climate hazard, building a forecasting scheme.

This study is based on climate complex networks and on the concept of event synchronization (ES), a nonlinear statistical similarity method useful to determine the correlations among spatial locations in terms of event co-occurrences. Using these tools we are able to identify drought regions in Europe based on the process itself and not depending on any external classifications, bringing out key aspects concerning drought dynamics at a regional scale for different rainfall accumulation periods from 1981 to 2020, while introducing new methodologies in general climate networks reconstruction from raw data. The understanding and ability of describing droughts as a complex phenomenon is still in a preliminary stage, but climate complex networks prove to be a powerful tool to reveal hidden features of this climatic process.

The remainder of the Chapter is organized as follows: in Section 4.2 we describe the data and the methodology we adopted to construct the meteorological drought networks; in Section 4.3 we present the results; in Section 4.4 we conclude the Chapter.

4.2 Methods

4.2.1 Data and spatial domain

We follow the procedure described in Ludescher et al. (2021) and Fan et al. (2021) to reconstruct our meteorological droughts networks from data (see also Section 2.3 of this dissertation), using the Standardized Precipitation Index (SPI) (McKee et al., 1993; Edwards, 1997; Guttman, 1999). The SPI measures precipitation anomalies at a given location, based on a comparison of observed total rainfall for a certain accumulation time interval of interest (denoted SPI-1, SPI-3, SPI-6, SPI-9, and SPI-12 months) with the long-term historic record for that period and specific area (European Drought Observatory, 2020). SPI values are positive (negative) for precipitation greater (less) than the median. The SPI is provided by the European Drought Observatory (European Drought Observatory, 2020), computed from the monthly precipitation data of the Global Precipitation Climatology Centre. We focus on the time interval 1981–2020 and analyze four different accumulation periods, namely the SPI-3, SPI-6, SPI-9, and SPI-12, building one continental network for each of these cases, assessing their similarities and differences. The SPI-1 month is not considered, since it may not be accurate for regions with high probability of zero accumulated rainfall during 1 month (European Drought Observatory, 2020), which is the case of some areas of northern Africa included in our study.

Our spatial domain is defined based on the Sixth Assessment Report of the IPCC (Jian and Hao-Ming, 2021; Iturbide et al., 2020): the regions NEU, WCE, and MED are taken as representation of Europe (Figure 4.1). Notice that meteorological droughts are defined on land, and thus sea is not considered.

The spatial domain is discretized with a resolution of $0.25° \times 0.25°$ (latitude × longitude). Each grid point is associated with four SPI series (one for each accumulation period) and will serve as a node of the graph.

4.2.2 Meteorological droughts identification

To identify meteorological droughts in the SPI time series we refer to McKee et al. (1993), where the author proposes a functional and quantitative definition of drought using the SPI as indicator: a meteorological drought is an event that occurs whenever the value of the SPI ≤ -1, whatever the accumulation period is. This definition and the related drought classes (Table 4.1) are still accepted and widely used (Spinoni et al., 2016; WMO, 2021). The event sequences from the complete SPI time series are recovered by selecting those occurrences with SPI ≤ -1, and consecutive events are removed, keeping only the first of successive drought conditions (see Figure 4.2).

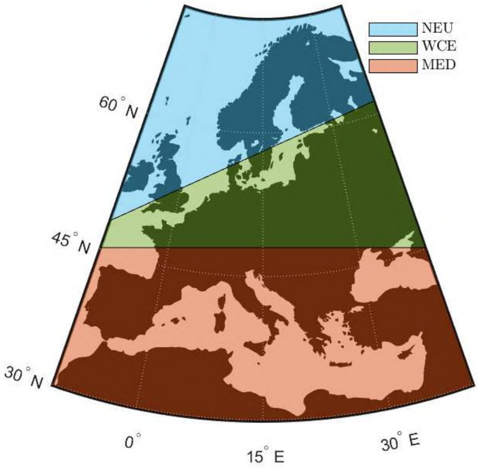

Figure 4.1: **Spatial domain of this study**. The domain is composed by using the IPCC regions NEU, WCE and MED (only land is considered). Latitude from 30° to 72.6° and Longitude from $-10°$ to 40°.

Table 4.1: Meteorological drought categories defined for values of the SPI from McKee et al. (1993).

SPI values	Drought category
-1 to -1.49	moderate drought
-1.50 to -1.99	severe drought
$\leq$ -2	extreme drought

4.2.3 Network construction

According to the event-like nature of this process, we use event synchronization (Quiroga et al., 2002; Malik et al., 2012) as statistical similarity measure to construct each of the four continental drought networks. Event synchronization is a powerful nonlinear method to assess the similarity of event series with unequal spacing between successive occurrences, and thus it is especially appropriate for studying extreme events (Fan et al., 2021). The degree of synchronicity of two event series is measured based on the relative timings of events, and it is obtained from the number of quasi-simultaneous occurrences. We summarize the advantages of this method as follows: (i) ES is designed to treat event-like time series; (ii) by using ES there is no need to set a specific time lag; (iii) ES has both a symmetric and asymmetric formulation, eventually being able to show driver–response relationships; and (iv) ES has been extensively used as a tool to construct climate extreme events' networks, proving to be enough efficient and informative (Malik et al., 2010; Agarwal et al., 2017; Boers et al., 2019; Strnad et al., 2023). The detailed algorithm is described in Section 2.3.1. The edges derived through event synchronization

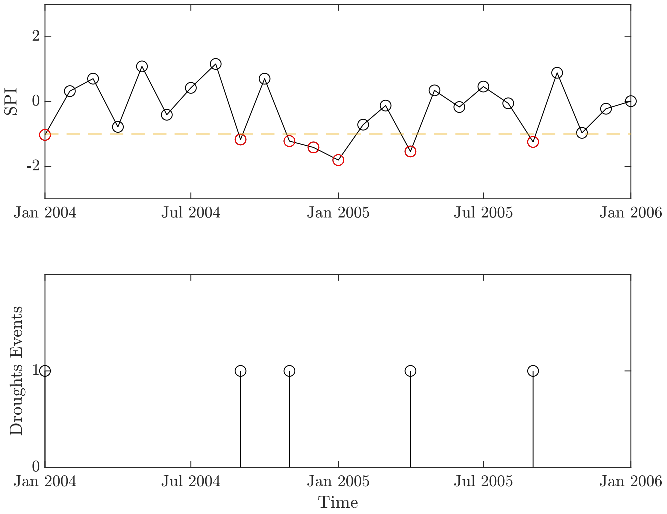

Figure 4.2: **Construction of event series.** From the complete SPI time series (top panel) we select those realizations with SPI ≤ -1 to form the droughts event series (bottom panel). Notice that consecutive events are removed, keeping only the first occurrence. This procedure is carried for every node of the space domain and for the entire time period 1981 - 2020.

represent the synchronicity in droughts occurrences between the nodes of the graph. In this preliminary stage, we are not concerned with the direction of synchronicity: two locations are linked if they display a co-evolution of meteorological drought events; therefore, the resulting four continental networks are undirected. Notice that we set a maximum time lag $t_{max} = 4$ months, above which the detected synchronizations are disregarded. This means that the synchronicity between two locations is considered as such if it happens at most in the timescale of a season.

4.2.4 Links attribution

It is possible to organize the synchronicity measure $Q(i, j)$ (see Eq. 2.17) between each pair of nodes i and j in an $N \times N$ matrix, where N is the number of nodes of our spatial domain. Each entry of the matrix lies between 0 and 1 and represent the strength of synchronization of node i and j. In principle, the synchronization between a node with itself is equal to 1, but we set it to 0 since self-loops are not meaningful in this context.

The connections contained in the four continental networks have different strengths, i.e., different values of synchronicity score $Q(i, j)$. Given the large extension and the high resolution of these graphs, it is not essential to carry the information of links weights: instead, it is more convenient to select only the strongest edges and derive an unweighted representations of each network (see Eq. 2.18), which still preserves the main structures of the original graphs.

Extracting the connections with the highest statistical similarity from the complete weighted graph is a very common procedure in general functional network reconstruction from raw data (Zanin et al., 2012), and it is well known in climate network science too (Ludescher et al., 2021; Gupta et al., 2021; Ciemer et al., 2020). In this field, the strongest links are considered to be the backbone structure of the climatic process under examination: indeed, when a climate correlation or synchronization network is built, it often resembles an all-to-all connected graph, giving no useful information about the main underlying structure which remains hidden under the great number of links. Cutting off the weakest edges is thus a fundamental step to get a clearer and meaningful representation of any climatic process, but it is not a trivial task. Scientists often tend to choose the threshold θ in Eq. 2.18 discretionally on a case-by-case basis (Kurths et al., 2019), generally optimizing the ratio between high correlation and sufficient number of events for comparison (Stolbova et al., 2014). Here we propose a rigorous way to choose the lower bound of synchronicity below which a connection is discarded.

Instead of constructing one 1981–2020 drought network for each accumulation period, we divide the complete dataset into two sub-databases (one with data from the period 1981–2000 and one with data from 2001–2020) and build two independent sub-networks for each of the two time intervals and for every possible cutoff threshold in terms of percentage of strongest preserved links (from 1 to 100). Notice that the two sub-databases are independent from each other, deriving from observations sampled in different periods of time.

Hence, we obtain 200 different undirected and unweighted drought networks for Europe. Since our aim is to build a single network as representative as possible of Europe's base meteorological drought conditions for the whole studied period, we assume the differences between the two sub-networks 1981–2000 and 2001–2020 to be minimum, since they are reproducing the same processes using independent data. In other words, if two locations i and j are drought-synchronized, this should result in both sub-networks. The underlying assumption we make here is that even if the frequency and duration of meteorological drought events may be changing due to climate change, the physical mechanism that shapes the locations' synchronization in drought event occurrences does not change in time, and the resulting spatial structure modeled with the climate network remains reasonably stable.

For every cutoff threshold we count the differences between the two sub-networks via the Hamming distance, which measures the global probability of non-equal entries in the two adjacency matrices:

$$H(A^{1981-2000}, A^{2001-2020}) = \frac{1}{N^2} \sum_{i,j} XOR(A_{ij}^{1981-2000}, A_{ij}^{2001-2020}), \tag{4.1}$$

where

$$XOR(A_{ij}^{1981-2000}, A_{ij}^{2001-2020}) = \begin{cases} 1 & \text{if } A_{ij}^{1981-2000} \neq A_{ij}^{2001-2020} \\ 0 & \text{else.} \end{cases} \tag{4.2}$$

The procedure is depicted in Figure 4.3. The Hamming distance is not the only possible choice to compare the topology of two networks (Zager and Verghese, 2008; Ullmann, 1976; Fernández and Valiente, 2001). However, the reason why we employ this metric is threefold: the networks we are comparing are undirected and unweighted and have the same link density. For this specific case, this method gives a sufficiently informative result, and it is also computationally easy. For more complicated scenarios, one should look into other more refined graph edit distances (Gao et al., 2010) or into spectral methods (Jurman et al., 2011) to capture the changes of a graph as a whole.

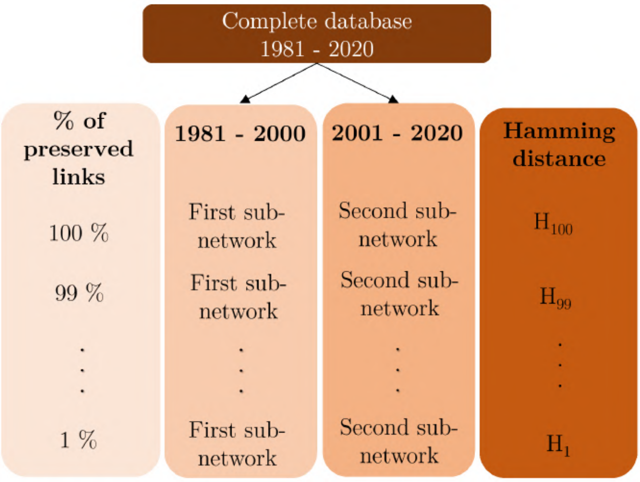

Figure 4.3: **Procedure to select the percentage of strongest links to preserve.** The original database is split symmetrically into two sub-databases. For each of them and for every cut-off threshold an undirected and unweighted Event Synchronization network is constructed. Every pair of sub-networks is used to compute the Hamming Distance. Finally, the % of links to preserve is chosen corresponding to a Hamming distance below 5%.

Even if we expect the two sub-networks to be similar for each cutoff threshold, they can never be identical due to noise and climate's internal variability. Therefore, we select the one for which the Hamming distance is below 5 % as the definitive cutoff threshold θ_{def}:

$$\theta_{def} : H(\theta_1) < H(\theta_2) < \dots < H(\theta_{def}) \leq 0.05 < H(\theta_{def+1}). \tag{4.3}$$

This requirement is satisfied for each of the four continental networks if we preserve the top 4% of links (Figure 4.4). Consequently, an unweighted and undirected link is placed every time the value of synchronization between two nodes is above the 96th percentile of the synchronization values distribution. This threshold is set equal for the four cases in order to compare the resulting networks, which in this way are characterized by approximately the same link density.

The definitive continental networks are therefore constructed for each of the four

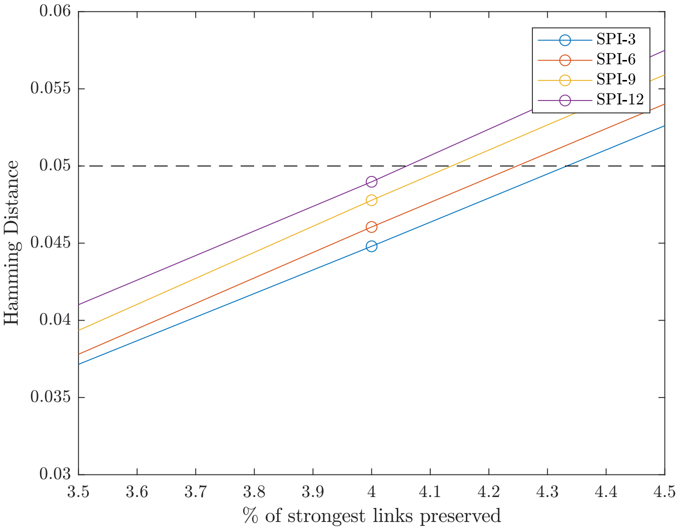

Figure 4.4: **Hamming Distance as a function of the percentage of strongest link preserved.** By choosing the 96-th percentile as cut-off threshold (preserving the top 4% of links) the differences between the two sub-networks are below 5% in each of the four cases.

accumulation periods as follows: (a) two undirected and unweighted sub-networks are retrieved from the data, one corresponding to 1981–2000 and the other to 2001–2020, taking the 96th percentile as cutoff threshold, and (b) the two sub-networks are intersected, taking only the common links between the two to form the final 1981–2020 Europe meteorological drought network.

With this procedure we not only identify the best cutoff threshold, but we have the additional advantage of selecting the connections which are significant and robust in time because they arise from independent sets of data: this constructed network does indeed retain the long-lasting backbone structure of the process, discarding the majority of the spurious synchronizations caused by internal variability and noise.

4.2.5 Community detection

After having built the four unweighted and undirected European networks, we proceed in partitioning them into regional clusters. This procedure is followed in Konapala et al. (2022) as well, where the authors use a distance-weighted synchronization to construct the graph. This filter strengthens the synchronicity among close locations, while penalizing any potential connection between distant areas. Moreover, the distance weight introduced by Konapala et al. (2022) is a relative metric, tuned on the extent of the studied domain. Even assuming that droughts propagation is influenced by geographical distance and therefore bounded to a certain level, this sensitivity should at least be fixed, not changing with the size of the studied area. Whereas according to the majority of studies in climate networks long connections can not be ignored, on the contrary, teleconnections play a crucial role in transferring climate information across the globe (Donges et al., 2009b; Tsonis et al., 2008, 2006; Boers et al., 2013, 2019; Stolbova et al., 2014). These considerations prompt us to identify regional clusters from the event synchronization network without introducing any distance weight.

To find the regional clusters for each of the four networks, we use the Louvain algorithm (Blondel et al., 2008), a heuristic method that is based on modularity optimization (Newman, 2006). The Louvain algorithm finds a local maximum of modularity, which depends on the order the nodes are picked (see Section 2.2.2). Therefore, we apply it 10,000 times for each continental network, taking the partition with the overall highest modularity. The communities found represent the regions in which a drought event is more likely to propagate once started: intra-connections are maximized over inter-connections, meaning that the nodes grouped together are characterized by a high cooperativity in terms of synchronization in meteorological droughts occurrences.

4.2.6 Regional networks

To analyze the synchronizations patterns of meteorological droughts, we build regional spatial networks for each community. This time, unlike what was done before for the four continental networks, once the nodes of one specific community are extrapolated, we use event synchronization to build weighted and directed graphs, using the anti-symmetrical score $q(i, j)$ in Eq. 2.17. This time, since we carry the links weight, it is not necessary to apply a link attribution procedure as previously described for the unweighted continental networks.

4.3 Results

The partitions of the four European drought networks resulting from 10,000 different realizations of the Louvain algorithm are shown in Figure 4.5.

We notice important similarities and differences between the four networks. The most relevant features that arise are the following: (i) the regional clusters of the Scandinavian Peninsula are quite comparable, with the western part of Norway always standing alone as one community, separated from Sweden, which forms another compact block, and Finland, often divided into several parts alongside the Kola Peninsula; (ii) the eastern part of the continent is split into latitudinal regions, well visible for the shortest accumulation periods while more and more fragmented in the 9- and 12-month cases; (iii) Turkey often forms one cluster; (iv) the Iberian Peninsula is connected to northwest Africa, except for the SPI-12 network; (v) the northern part of Italy is joined with the north of the Balkan Peninsula; and (vi) the increase of the fragmentation of the communities with the accumulation period does not translate into an increment of the communities number (see Table 4.2) but to the disruption of the spatial continuity of the clusters from the shortest accumulation periods to the longest one.

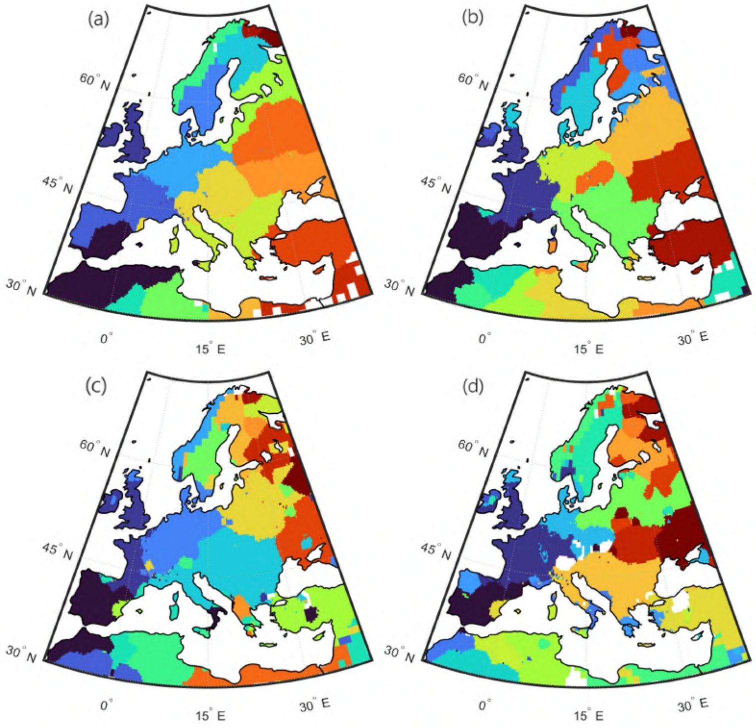

Figure 4.5: **Communities detected with the Louvain algorithm**. SPI-3 Network (a), SPI-6 Network (b), SPI-9 Network (c) and SPI-12 Network (d). Each color represents a different community while white areas are either part of the sea or consist of nodes belonging to clusters with less than 100 nodes.

We find that the latter characteristic is due to the presence of long links, which are more numerous the higher the accumulation period: we register 25,565 long links in the SPI-12 network, 1 order of magnitude more than the 2,722 long links in the SPI-3 network (see Figure 4.6 and Table 4.2). In Boers et al. (2019) the extreme precipitation global climate network was characterized by two different weather systems, a regional power-law-distributed one and a super-power-law distributed global pattern. This latter system was detected from network links longer than 2,500 km. In our analysis, these features seem to emerge again, even if we focus on droughts and not precipitation extremes, and Europe is not big enough to contain a statistically adequate number of possible long connections (≥ 2,500 km). Nevertheless, if we look at Figure 4.6, we see a shift in the distribution of the number of links when this critical 2,500 km length is passed. Moreover, the number of long links increases with the accumulation period, even when the total number of connections does not change sensibly among the four cases (see Table 4.2).

This exhibits the primary role of long connections in the context of climate networks.

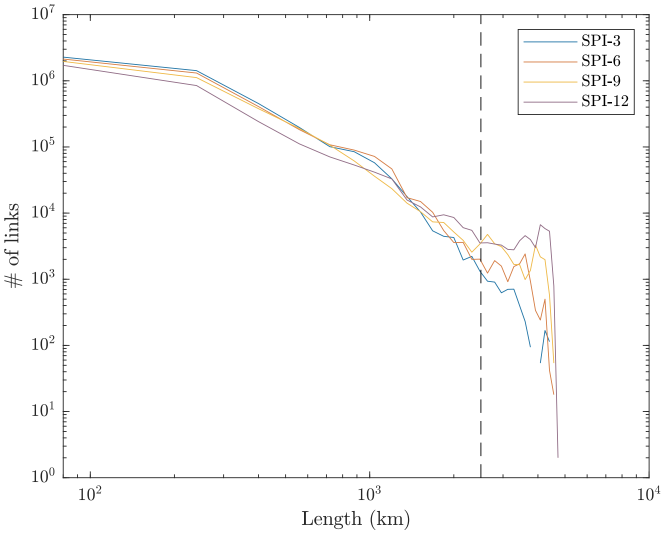

Figure 4.6: **Links length distribution.** Distribution of the number of links with their length (great circle distance of the two nodes connected by the link) for each of the four Europe's meteorological drought networks (colored lines). The dashed line represents the 2500 km distance.

The presence of these long links is typically due to large-scale atmospheric patterns which could act as common drivers of climate extremes of distant regions. This feature would not emerge if we used a distance weighted network's construction: in fact, we would have lost long connections, being left with four partitions that are very similar to one another. We argue that short meteorological drought events (with accumulation period up to 6 months) are driven by regional climate systems, while long ones (with accumulation period from 9 months onward) are due to large-scale patterns that affect an ample portion of the continent. Rossby wave trains could be a potential reasonable candidate for connecting the distant area in the longitudinal direction. Follow-up studies could better clarify the climate precursors responsible for the appearance of these long connections for high-accumulation periods.

Once we identify the clusters of each of the four continental networks, we proceed in studying each regional community separately, constructing weighted and directed graphs. The anti-symmetrical score $q(i, j)$ (Eq. 2.17) which results from the application of event synchronization to the regional clusters can be used to derive the average out-degree k_i^{out} and the average in-degree k_i^{in} of each node i in its community c and, consequently, its overall degree centrality k_i:

$$k_i = k_i^{out} + k_i^{in} = \frac{1}{N_c - 1} \sum_{j \in \Gamma_i} q(i, j) + \frac{1}{N_c - 1} \sum_{j \in \Gamma_i} q(j, i), \tag{4.4}$$

Table 4.2: Number of total and long links ($\geq 2,500$ km) in the four Europe's meteorological drought networks and number of found communities.

	Total Links	Long Links ($\geq 2,500$ km)	% of long links	Communities
SPI-3 Network	2,340,806	2,722	0.12	19
SPI-6 Network	2,210,586	7,074	0.32	19
SPI-9 Network	1,979,005	14,599	0.74	19
SPI-12 Network	1,615,415	25,565	1.58	21

where N_c is the total number of nodes belonging to community c, and Γ_i denotes the neighbors of node i. The degree centrality k_i lies between -1 and 1. Here, a node i with $k_i < 0$ is defined as a sink, otherwise as a source. Each community of each of the four continental networks can thus be studied under this framework, identifying a source–sink system.

Here we show some interesting source–sink systems found in each of the four continental networks.

In the SPI-3 network, Portugal essentially acts as a source for its community (Figures 4.7a,b), suggesting that the lack of humidity could move from the coast towards inland. The role of Portugal as a source could be explained by two main points: on the one hand, this area is on average the rainiest in the Iberian Peninsula, and thus it is more sensitive to dry conditions; on the other hand, it is more affected by the North Atlantic Oscillation and the East Atlantic pattern, two important atmospheric processes which influence the Iberian precipitation regime (Benito et al., 1996). A different situation is depicted in the central Europe community (Figures 4.7c,d), where the internal part of the region drives droughts' occurrences to the coast. As shown by Hofstätter et al. (2018), precipitation patterns over central Europe are largely controlled by atmospheric cyclones: consequently, the evolution of meteorological droughts in this region may be directed along cyclones tracks. A further investigation into the average patterns of the various cyclone types may help in clarifying this matter better.

In the SPI-6 networks, it is interesting to notice the connection between Northern Ireland and the Norwegian mountains (Figures 4.8a,b). As we already pointed out looking at Figure 4.5, the western part of Norway is always separated from the rest of the Scandinavian Peninsula in every of the four accumulation periods networks, but in the specific case of the SPI-6 network, Northern Ireland is synchronized with this mountainous chain, and in particular it uniformly acts as a sink. While it seems clear that the separation of Norway from the rest of the Scandinavian Peninsula arises from the blocking action of the Norwegian mountains, the linkage between Northern Ireland and Norway at this accumulation period is unforeseen; nevertheless we anticipate the prominent role of atmospheric rivers moving through the Norwegian Sea and the Scandinavian pattern, which leads to dry conditions over the northern part of the continent

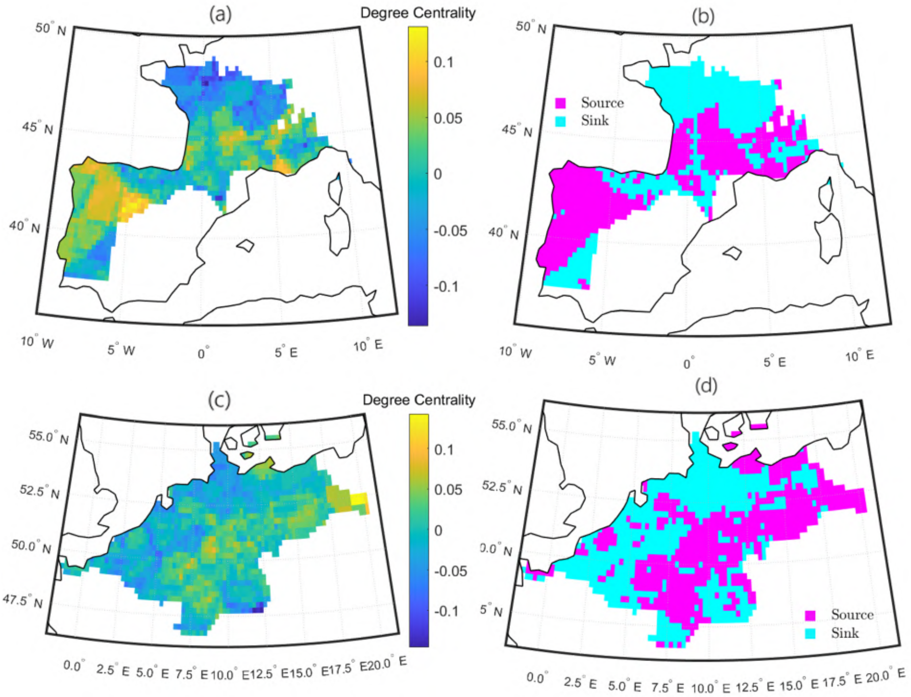

Figure 4.7: **Two regional spatial networks from the SPI-3 Europe meteorological drought network.** Degree centrality (a, c) and source-sink system (b, d).

during its positive phase (Bueh and Nakamura, 2007). Another regional spatial network derived from the SPI-6 graph that we show here is the Turkey one. We mentioned that this region often consistently form one sole cluster, displaying a certain stability over the different accumulation periods cases. In the SPI-6 network the western and central regions of Turkey precede the east in the occurrence of meteorological droughts events (Figures 4.8c,d). While the North Atlantic Oscillation represents a remote driver of precipitation over Turkey, the Mediterranean and the marine polar air masses are direct causes of rainfall in this region (Sariş et al., 2010), and their west–east direction suggests a key role in droughts' diffusion as well.

For the SPI-9 network we show two communities which are somehow complementary to each other (Figure 4.9): the first one (Figures 4.9a,b) includes the majority of the Iberian Peninsula with a small region of Turkey, while in the second one (Figures 4.9c,d) we see the remaining part of Turkey with a small region of Spain. The only difference between the two communities, which may cause the distinction of this two regional clusters, is the fact that in the first case a portion of northern Africa and south Italy come into the picture as well. Looking at these two examples, we highlight two main features: (i) Portugal is still a big source (Figures 4.9a,b), as happened in the SPI-3 case, and (ii)

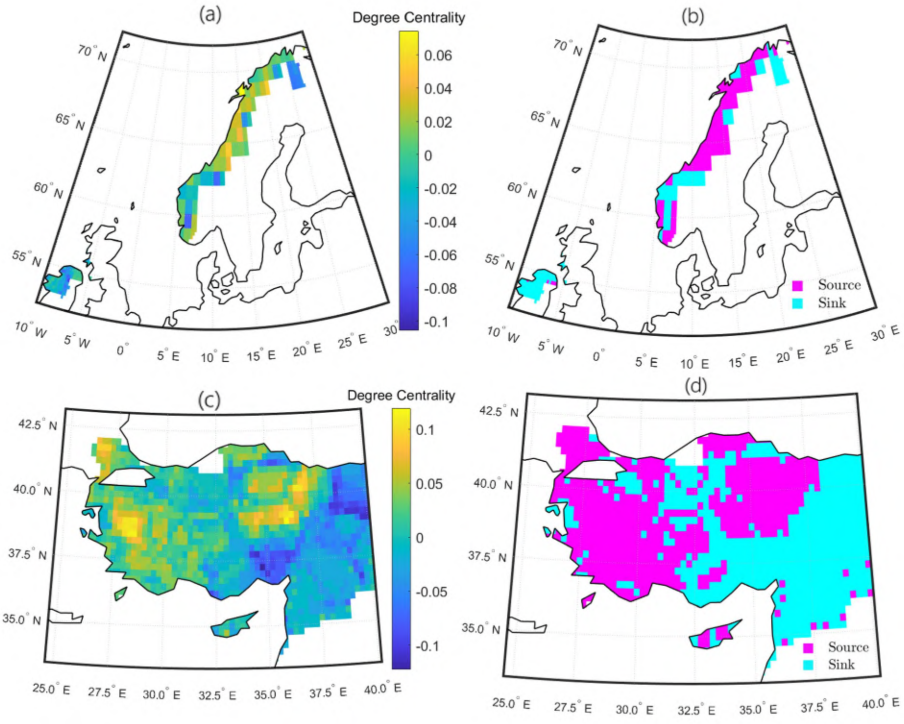

Figure 4.8: **Two regional spatial networks from the SPI-6 Europe meteorological drought network.** Degree centrality (a, c) and source-sink system (b, d).

long connections strongly contribute to shaping the clusters' landscape, linking distant regions which are not generally related to the short accumulation periods' networks.

This latter characteristic is even accentuated in the SPI-12 community structures. In Figure 4.10 we show two examples taken from this last network. In the first one (Figures 4.10a,b) we see a community very similar to the one seen in Figure 4.10c: the majority of Turkey is still connected to the same nodes of eastern Spain, but, differently from before, this time the Spanish region is a source for the rest of the community. This shows that the same nodes may play different roles in different accumulation periods: in fact, they may belong to different communities, or, as this latter examples show, they can still be part of similar clusters but with a shift in the proportion of incoming links versus outgoing ones. As we already pointed out previously, the presence of long links in higher accumulation period networks contributes to connecting distant regions in longitudinal direction more than latitudinally, and the reason may lie in the propagation of Rossby waves. In Figure 4.10c and d there is a clear vertical separation in the source-sink system: the west part of both Great Britain and France is a source for the eastern regions of these two territories. The cluster also includes a small region of the Scandinavian Peninsula. The role of western France as a source for the eastern part of the country seems to be

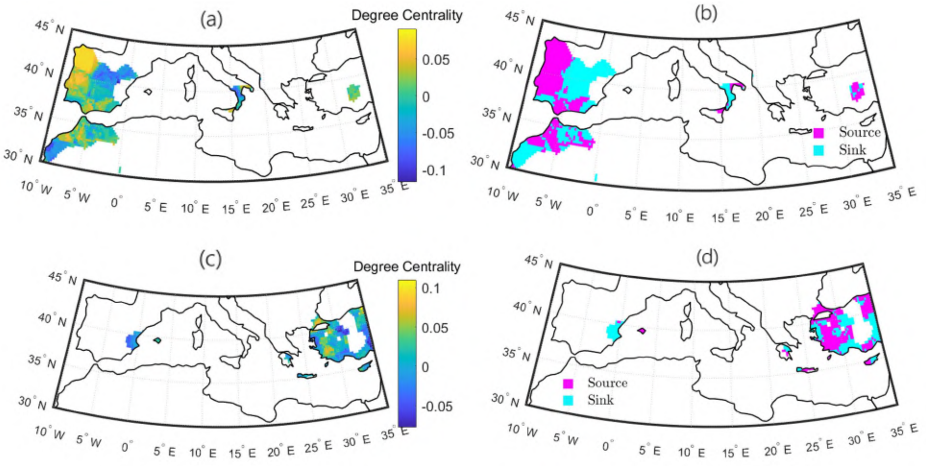

Figure 4.9: **Two regional spatial networks from the SPI-9 Europe meteorological drought network.** Degree centrality (a, c) and source-sink system (b, d).

confirmed by the increasing trend in meteorological drought events in this region, as reported in Spinoni et al. (2016) too. Vidal et al. (2010) also show that the majority of meteorological drought events at the 12-month timescale are located over the south and the eastern coast of France. As for Great Britain, the north and the central and southern part of the country consistently belong to different clusters in the SPI-6, 9, and 12 networks (see Figure 4.5). This could be related to the NAO's impact in the UK, with positive correlation to precipitation in the north and negative in the south (Rahiz and New, 2012). Moreover, the source's role of Wales and south England displayed here (Figure 4.10d) is consistent with previous studies (Phillips and McGregor, 1998; Fowler and Kilsby, 2002).

Finally, we point out that every region has its own precipitation regime, which is in turn affected by different atmospheric processes and patterns, whose influence also changes according to the specific timescale. For this reason, each of the showed regional source–sink system should be studied separately in the future in more detail.

4.4 Conclusion

In this study we propose a method to build robust climate networks from data and to identify meteorological drought regions and related source–sink systems in Europe.

Our networks are based on the synchronicity of droughts occurrences within a season and are constructed based on the Standardized Precipitation Index for four accumulation periods, 3, 6, 9, and 12 months, highlighting similarities and differences between them. The features of meteorological droughts for different timescales have never been investigated before through the lens of network theory. Here, we find that long connections play a crucial role in shaping drought regions and become more and more important

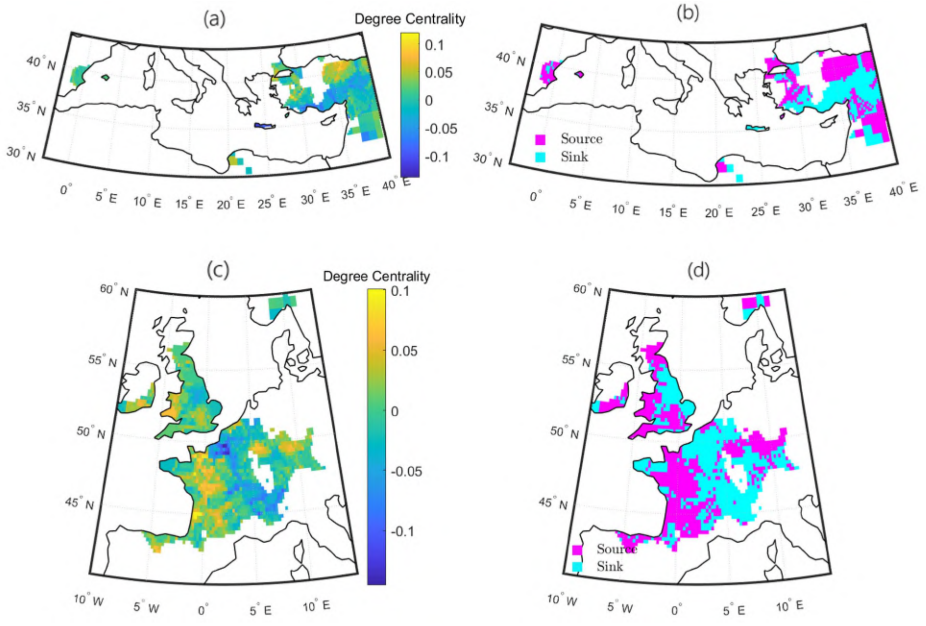

Figure 4.10: **Two regional spatial networks from the SPI-12 Europe meteorological drought network.** Degree centrality (a, c) and source-sink system (b, d).

when long accumulations are considered. This suggests that, while short periods of precipitation's deficiency (1 to 6 months) tend to evolve in confined regions, long-lasting droughts (9 to 12 months) are likely to propagate across large portions of the continent. Short meteorological drought events could be driven by regional climate systems, while long ones could be driven by large-scale patterns, like Rossby waves, but further studies are needed to better clarify the atmospheric precursors of these long connections.

The Hamming procedure that we introduce here offers a new way to reduce the uncertainty of link attribution in unweighted and undirected networks reconstruction from raw data, when there is no previous knowledge about the system under study. This method could be potentially applied to different areas of study and also be extended to weighted and directed graphs. From these more reliable continental networks, we uncover regional communities by applying the Louvain algorithm, a well recognized method for cluster identification. We believe that this way of partitioning a certain geographical area via network theory concepts could be helpful in climate region identification, shaping them not via external classification or general climatic variables but based on the specific climate process under study.

Meteorological drought regions are separately studied identifying source–sink systems. These systems highlight the spatial patterns along which the drought events have developed on average during the period 1980–2020. Moreover, they could be a useful tool to use in forecasting these events in the sink nodes when the sources experience a drought condition.

5 Compound hot and dry extremes synchronizations in Europe

Adapted from *Giaquinto, D., Di Capua, G., Marzocchi, W., and Kurths, J.: Spatio-temporal evolution of compound hot and dry extremes synchronizations in Europe*, accepted for publication by Climate Dynamics.

Abstract The probability of incidence of compound extreme climate events is increasing due to human-induced climate change: in particular, there is high confidence that concurrent hot and dry extremes will become more frequent with increased global warming. In this context, Europe is no exception. Understanding the aggregated impact of synchronized compound hot and dry events at different locations is a pressing issue, especially when it comes to predicting these extremes. We use concepts and methods derived from network theory to highlight hotspot regions in Europe where these spatially compound extremes are increasing and analyse the atmospheric precursors driving these anomalous conditions. Using ERA5 reanalysis data and focusing on the summer and winter seasons of the period 1941-2020, we construct evolving networks constituted by 51 consecutive blocks, encoding the spatial synchronization structure of compound hot and dry events. Next, we highlight the regional and seasonal differences of compounds occurrences and synchronizations, unravelling the main changes in the graphs structure, identifying hotspot regions and, finally, describing the atmospheric conditions behind compound events. The increase of compounds frequency and spatial synchronizations do not always match: synchronizations increase in Southeastern Europe during winter and in some locations in Finland, north of Poland and the Baltic states in summer, although, in both cases, we do not detect a corresponding trend in compounds occurrences. Moreover, we show that most of the synchronizations evolution can be explained by atmospheric pressure dynamical changes, including NAO and SNAO intensity. This work brings out key aspects concerning the underlying spatio-temporal dynamics of concurrent hot and dry events.

5.1 Introduction

Global warming sets new unprecedented temperature records every year, with 2023 identified as the hottest year on record (Copernicus, 2024) and June 2024 being the thirteenth warmest month in a row compared to the respective months in the past (Copernicus Climate Change Service, 2024a). As a direct consequence, the increase in intensity and duration of climate and weather extremes poses serious societal and environmental threats, such as biodiversity loss (Habibullah et al., 2022), water scarcity for most of the population (Zhang et al., 2019), impacts on human health and mortality (Yadav et al., 2023). Thereby, the increase of such events has been reported by several studies over the last decades (AghaKouchak et al., 2020; Fischer et al., 2021; Seneviratne et al., 2021), with the aim of understanding and predicting future occurrences to reduce risk and implement adaptation strategies. Still, many scientific challenges are ahead of us.

Single extremes located in distant regions could be statistically related, due to numerous and often nonlinear mechanisms, including feedbacks. In such circumstances, the superposition principle does not hold, and when multiple events hit, the associated impacts are larger than the sum of the single ones (Zscheischler et al., 2018). These phenomena are referred to as *climate and weather compound events* (Zscheischler et al., 2020a), which have been the topic of several recent research papers. Climate compound events have been classified into different types (Zscheischler et al., 2020a), e.g., (i) spatially compounding climate events, where multiple locations are affected by climate hazards within a short time window, or also (ii) temporally compounding events, in case of a temporal sequence of extremes at one location. Whereas about the specific involved hazards, several examples have been brought to the attention in the literature: hot-humid (Li et al., 2020) or hot-dry (Ha et al., 2022) extremes, extreme precipitation and storm surge (Bevacqua et al., 2019), wet–windy (Leeding et al., 2023) and hot–windy (Tavakol et al., 2020) extremes. Thereby, compound events research calls for an interdisciplinary approach, owing to the different processes involved at various spatial and temporal scales, as well as to the implications for society at different levels (Tabari and Willems, 2023).

Europe has been reported as one of the major heatwaves hot-spots in the northern hemisphere, also due to the persistence of double jet states over Eurasia (Rousi et al., 2022). Here, heatwaves have been the most impactful climate hazard in terms of human fatalities (Douris and Kim, 2021), e.g., in summer 2003 (Di Napoli et al., 2018; Fink et al., 2004), when more than 70,000 deaths were caused by strong temperatures (Robine et al., 2008), or the more recent 2022 heatwave (Ballester et al., 2023), which induced water shortages and wildfires across large parts of western and southern Europe (Tripathy and Mishra, 2023). Concerning dry extremes (Spinoni et al., 2015a), several studies agree that while the north of the continent is experiencing wetter than average conditions, the Mediterranean has seen more severe and frequent drought states (Spinoni et al., 2017; Copernicus Climate Change Service, 2024b). This is mainly due to the increased precipitation over northern latitudes, and the simultaneous temperature increase and precipitation decrease over the Mediterranean area (Spinoni et al., 2015b). The occurrence of both extreme flooding and droughts with high spatio-temporal variability has been once more confirmed by the recently published European State of the Climate 2023

(Copernicus Climate Change Service, 2024c). The prolonged persistence of precipitation deficiency represent a warning signal for the development of other types of droughts too, such as agricultural or hydrologic droughts (Wilhite and Glantz, 1985; Seneviratne et al., 2012). For instance, just consider the high correlation between 2023 precipitation (Copernicus Climate Change Service, 2024d) and soil moisture (Copernicus Climate Change Service, 2024e) anomaly in Europe. River discharge may also be affected by low precipitation, like in the case of the Po River, which experienced below-average flow throughout the entire year (Copernicus Climate Change Service, 2024f).

As for compound hot and dry extremes, it has become evident that these events will become more frequent and severe due to global warming across large areas of Earth (Yin et al., 2023; Seneviratne et al., 2021). Potential feedback mechanisms linking these two conditions further exacerbate the risk (Seneviratne et al., 2021, 2010). For instance, temperatures in high-latitude regions may be critically influenced by the snow-albedo feedback (Hall and Qu, 2006), while soil moisture-temperature feedbacks (Seo and Ha, 2022) are thought to contribute to the additional warming observed over mid-latitude land areas compared to the global mean temperature increase (Vogel et al., 2017; Seneviratne et al., 2018). Using a climate model ensemble, Lorenz et al. (2016) demonstrate the influence of soil moisture variability on the intensity, frequency, and duration of temperature extremes, as well as its connection to precipitation extremes. They report that precipitation deficiency in the mid-latitudes is likely linked to soil moisture variability. Both atmospheric processes and land surface mechanisms contribute to the observed negative temperature–precipitation correlation (Berg et al., 2015).

Simultaneous hot and dry extremes impact the European continent in multiple ways, affecting primary production (Ciais et al., 2005; Zscheischler et al., 2017), increasing wildfire risk (Gudmundsson et al., 2014; Ruffault et al., 2016; Sutanto et al., 2020), and raising mortality rates (Stott et al., 2004; Ionita et al., 2017). Several studies agree that the rise in compound hot and dry extremes in Europe is primarily driven by atmospheric conditions (Manning et al., 2019; De Luca and Donat, 2023). Rising temperatures promote the transition from meteorological drought to soil moisture depletion by enhancing evapotranspiration (Manning et al., 2019), especially in wetter regions (Manning et al., 2018). In these areas, reduced precipitation, commonly linked to decreased cloud cover and anticyclonic circulation patterns, leads to higher net radiation, which, in turn, increases evapotranspiration and exacerbates water scarcity by depleting soil moisture (Teuling et al., 2013). Higher temperatures further intensify this process, particularly in northern and central Europe, where rainfall levels have not significantly declined (De Luca and Donat, 2023). However, this mechanism is limited in drier regions where soil moisture is already low. This is particularly true for western Europe and the Mediterranean above all, where both decreasing precipitation and rising temperatures contribute to extreme compound hot and dry conditions (Zhao et al., 2024).

Nonetheless, regardless of the specific mechanisms involved, it is clear that the frequency of hot and dry extremes across Europe is generally increasing. However, little has been done to assess whether co-occurring hot and dry extremes in different locations—i.e., spatially compound hot and dry extremes (SCHADEs)—are also on the rise. Previous studies associated spatially compound extremes to amplified planetary waves (Kornhuber et al., 2020), modes of climate variability (De Luca et al., 2020) or large-scale variability patterns (Ye and Messori, 2020). Hereby, assessing the trends and atmospheric conditions driving simultaneous compound hot and dry events across multiple locations is essential, particularly for improving the predictability of these extremes and implementing tailored adaptation strategies in hotspot regions.

For these reasons, we aim to assess if and how the synchronizations of SCHADE events are changing in Europe. Complex networks represent a promising tool in this perspective. Various real-world systems such as power grids (Arianos et al., 2009), the internet (Maslov et al., 2004), human contacts (Goh et al., 2007), and more (Ausloos et al., 2017; Bardoscia et al., 2021), can be conceptualized as the result of the interactions of many dynamical units, whose relationships structure often encodes and influences the system's overall dynamics (Boccaletti et al., 2006). Over the past two decades, the study of the climate system has been approached through network theory as well, complementing the well established methodologies of physical modeling (Tsonis and Roebber, 2004; Ying et al., 2020). Under this framework, climate is assumed to be approximated via a grid of low dimensional nonlinear dynamical units (Donges et al., 2009a). In this study, we employ spatially embedded climate networks, whose nodes are constituted by geographical sites on a regular latitude-longitude grid, while the links are established based on the degree of statistical similarity between processes occurring at different locations. Once the network structure is established, it is possible to study its topology to get new insights into the statistical relationships and/or spatial patterns of the analysed phenomena. Spatially embedded climate networks have been used to describe numerous climate processes at different spatio-temporal scales (Boers et al., 2019; Gupta et al., 2021; Giaquinto et al., 2023), and to study climate extremes in particular (Vallejo-Bernal et al., 2023; Ludescher et al., 2021). Therefore, using ERA5 reanalysis data (Hersbach et al., 2023a), we model the European SCHADEs synchronization structure as an evolving climate complex network, constructing one evolving network for the boreal summer season (June, July and August) and one for the boreal winter season (December, January and February) of the period 1941-2020. This approach allows us to describe synchronization trends at the local and regional scale, highlighting hot-spot regions for synchronized compounds and connecting the graph structure to atmospheric circulation patterns.

5.2 Methods

5.2.1 Data and spatial domain

In this study, we focus on hot and dry extremes on European land grid points, defined as the territory between 30° and 72.6° N latitude and -10° and 40° E longitude. This area results from the merging of the IPCC Sixth Assessment Report regions North Europe (NEU), West and Central Europe (WCE) and Mediterranean (MED) (Iturbide et al., 2020); the latter is further subdivided in East (EMed) and West Mediterranean (WMed), as reported in Figure 5.1. Furthermore, since we define dry states based on precipitation regimes, desert locations (according to the Köppen-Geiger climate classification (Peel et al., 2007)) are excluded, given their low rainfall levels (Figure 5.1).

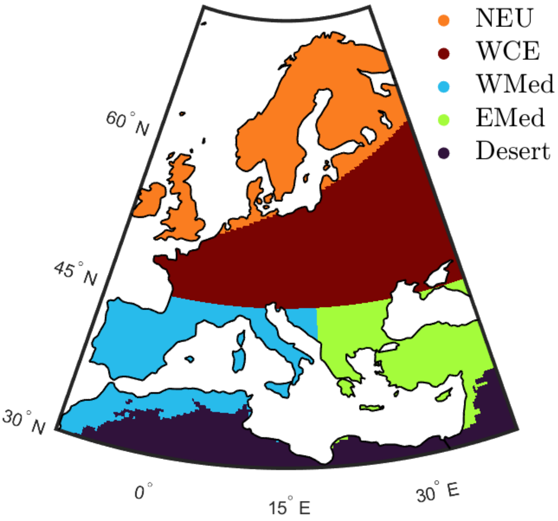

Figure 5.1: **Spatial domain and subregions used in this study.** Desert and sea locations are not considered.

We use ERA5 reanalysis data (Hersbach et al., 2023a) for the period 1941-2020 for the summer (June, July and August, JJA) and the winter (December, January and February, DJF) seasons separately. For the DJF season, leap days are removed. We employ the daily maximum temperature at 2m T_{max} [°C], the daily cumulated precipitation P [m] and the geopotential height at 500 hPa $Z500$ [m]. For each of the mentioned fields used in this study and at each time step, we estimate the trend from the best-fit line using least-squares and remove it, assuming it linear in a first-order approximation at least. While T_{max} and P are collected with a spatial resolution of 0.25°x0.25° for the land area shown in Figure 5.1, $Z500$ is collected for the entire globe at resolution 1°x1°. Finally, we also collect mean sea level pressure data SLP [Pa] at resolution 1°x1°, which we use to compute daily North Atlantic Oscillation (NAO) and Summer NAO (SNAO) indices for the winter and summer seasons, respectively (for more details, please see Appendix A, Section A.1).

5.2.2 Hot, dry and compound extremes identification

The 30-year period from 1941 to 1970 is used as reference to determine the historical distributions of maximum temperatures and cumulated precipitation for each location i of our spatial domain, i.e. grid points on the regular 0.25°x0.25° European lattice (19,425 nodes in total). We select this 30-year period as a reference following the convention of using climate normals as baseline conditions for assessing climate states at a given location (World Meteorological Organization, 2017).

A hot extreme occurs at grid point i on day d if the observed maximum daily temperature is higher or equal than the 90th percentile of the historical distribution, defined as the set of maximum daily temperatures of the 31 days cantered around d from the reference period:

$$T_{max}(i,d) \geq \{(T_{max}(i,[d-15,d+15]))_{[1941,1970]}\}_{90th}. \tag{5.1}$$

In practice, for each location i and calendar day d, we collect the maximum temperature of that day and of the 15 days which precede and follow d, during the 30-year reference period from 1941 to 1970. This selection results in a total of $31 * 30 = 930$ values, which constitute the historical distribution of maximum daily temperature of day d and location i. The 90th percentile of this set is used as the threshold (right hand-side of Eq. 5.1) to identify hot extremes.

A dry extreme is detected at location i on day d if the observed cumulated precipitation during the last 31 days including d is lower or equal than the 10th percentile of the historical distribution, defined as the set of cumulated precipitation from the reference period:

$$\sum_{t=d-30}^{d} P(i,t) \leq \left\{\left(\sum_{t=d-30}^{d} P(i,t)\right)_{[1941,1970]}\right\}_{10th}. \tag{5.2}$$

In this latter case, since we use cumulated precipitation, the historical distribution from which we take the 10th percentile to asses dry extremes at location i on day d is constituted by 30 values.

Notice that each calendar day is assigned to specific thresholds to define the hot and dry extreme occurrences respectively, and, since our data are detrended, we also account for the higher temperature baseline of recent times compared to the past. Our results are thus based on detrended anomalies and both the climatological and seasonal cycles are removed (Di Capua et al., 2020b).

In principle, since our definition of extremes is percentile-based, stationary time series should have the same number of single hot (dry) extremes. However, although we remove the linear trend from the data prior to identify the extremes, we do not observe a uniform spatial distribution of single extremes (see Figure A.2 in Appendix A). This is due to the non-stationary variance of the temporal series: even if the trend is removed from the mean, a trend in the extreme values of the distribution still remains for some nodes.

Finally, for each location i on the regular 0.25°x0.25° European lattice, a compound event is detected on day d if both a hot and a dry extremes occur at i on day d. This way, we get binary event series of compound events for each location i of our spatial domain for the entire analysed period 1941-2020.

5.2.3 Network construction

The SCHADEs network is established following the climate network reconstruction from data approach described by (Fan et al., 2021) and in Section 2.3, and applied in several studies in the recent past (Boers et al., 2019; Vallejo-Bernal et al., 2023; Giaquinto et al., 2023; Gupta et al., 2021; Ludescher et al., 2021). Given the event-like time series of compound events, we use Event Synchronization (ES) (Quian Quiroga et al., 2002; Malik et al., 2012) as statistical similarity measure to estimate the compound events synchronizations between each pair of nodes. The degree of synchronicity among nodes i, j is measured based on the number of quasi simultaneous events occurrences between the associated event series. Event l occurring at i at time t_l^i is considered to be synchronized with event m occurring at j at time t_m^j if $|t_l^i - t_m^j| < \tau_{lm}^{ij}$, where

$$\tau_{lm}^{ij} = min\{|t_{l+1}^i - t_l^i|, |t_l^i - t_{l-1}^i|, |t_{m+1}^j - t_m^j|, |t_m^j - t_{m-1}^j|, t_{max}\}/2. \tag{5.3}$$

By setting $t_{max} = 14$ days, we ensure that only concurrences developing in a time window of maximum 7 days are counted as synchronizations. We choose this maximum lag considering that hot extremes are usually detected on timescales of at least three days (Russo et al., 2015; Perkins and Alexander, 2013), while precipitation deficiency could last for several months (Spinoni et al., 2014). Therefore, the duration of a compound hot and dry event, the way we define it, is limited by the temperature anomaly and it is restricted to few days. Thus, it makes sense to assume that SCHADEs synchronizations take place in the space of no more than 7 days.

Here we use the undirected version of ES, since we are not concerned with the direction of synchronicity; that is why Eq. 5.3 differs from Eq. 2.14. Therefore, $Q(i, j) = Q(j, i)$ and the resulting synchronization network is undirected (see Section 2.3 for further details about the ES algorithm).

ES is particularly suited for our purposes because it is specifically designed to treat event-like time series, and indeed, it has been extensively used to construct climate extreme events networks, proving to be enough efficient and informative (Giaquinto et al., 2023; Malik et al., 2010; Agarwal et al., 2017; Strnad et al., 2023). Moreover, since the maximum time lag τ_{lm}^{ij} is specific to each event pairs and it is dynamically computed, there is no need to set it a priori (Quian Quiroga et al., 2002).

5.2.4 The evolving network approach

We employ evolving networks to analyse the temporal evolution of SCHADEs synchronizations. This evolving framework is appropriate to detect temporal changes in the graphs structure and thus in the synchronizations patterns. The general framework to construct our evolving networks, one for the JJA and one for the DJF season, is depicted in Figure 5.2.

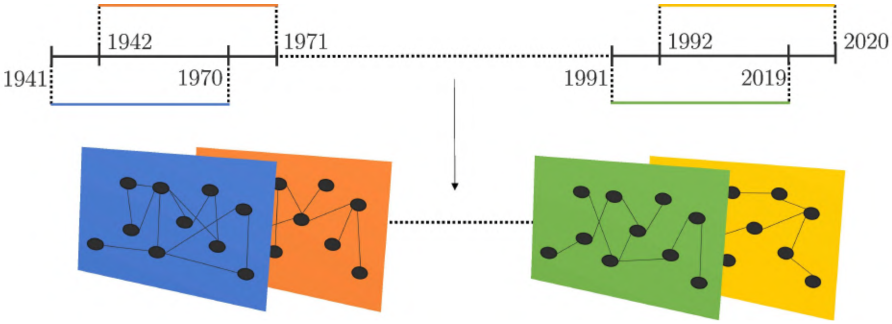

Figure 5.2: **General framework to construct the evolving network.** The entire time period is divided in intervals of 30 years using a time window moving with a one year step, obtaining a total of 51 intervals. For each of the 51 30-year intervals, one different network block is built for the analysed European land area. This procedure is separately carried for the JJA and DJF seasons.

The 80 years period from 1941 to 2020 is divided in 51 blocks using a 30-year time window, moving with a one year step. For each of the 51 30-year time windows, one network block is established using the procedure described in Section 5.2.3. Notice that the nodes are not changing from one block to the next, being the 19,425 fixed grid point on the regular European 0.25°x0.25° lattice, while the links depend on the different SCHADEs synchronizations taking place during each 30-year block.

5.2.5 Link attribution

Once we get all synchronization scores $Q(i, j)$, we test their significance to filter out spurious interactions. For each node pair i and j, we construct 500 surrogate series of j by uniformly and randomly shuffling block of events year-wise; afterwards, we calculate the null-model distribution of $Q(i, j)$ by performing ES for the 500 i and j pairs. By uniformly and randomly redistributing year-blocks rather than events themselves, we preserve any seasonal serial correlation, which we assume to be meaningless across seasons. We test the sensitivity of our results to a higher number of surrogates (up to 2000), and decide to keep the numerosity of the null model to 500 shuffled series for computational reasons, since we do not find major variations. Similar approaches to null model construction have been used in previous climate networks studies (Boers et al., 2019; Vallejo-Bernal et al., 2023; Rheinwalt et al., 2016).

For each observed value of synchronization $Q(i, j)$, we compute its associated p-value using the respective null model. Subsequently, the p-values are corrected using the Benjamini-Hochberg false discovery rate approach (Benjamini and Hochberg, 1995; Benjamini and Yekutieli, 2001) to take into account multiple significance testing, since we perform $\simeq 10^8$ comparisons. Finally, a link between nodes i and j is defined if their observed synchronization score $Q(i, j)$ is significant at $\alpha = 0.01$. Different choices of significance levels for link attribution are possible (Boers et al., 2019; Gupta et al., 2021; Vallejo-Bernal et al., 2023; Ludescher et al., 2021), leading to different network densities. We choose $\alpha = 0.01$ to limit the density of the network, but keeping enough links to get informative results.

The resulting network is undirected and unweighted. Since the links model the significant synchronizations shared between nodes, we use the terms link and significant synchronization, or more simply synchronization, interchangeably.

5.2.6 Network indices

Next, to extract valuable information from the two evolving networks, we characterize the graphs by looking at some indices derived from network theory. There are numerous network measures that can be used to assess the properties of a graph (Boccaletti et al., 2006), several of which have been applied in climate networks studies (Donges et al., 2009a), e.g. local measures like the degree centrality (Gupta et al., 2021), mesoscale measures like the clustering coefficient (Gupta et al., 2021), global measures like the closeness (Donges et al., 2009b) and the betweenness centrality (Boers et al., 2013), or even community detection algorithms (Giaquinto et al., 2023). In this study, we employ the regional and cross-regional link densities (ρ), the degree centrality (k) and the clustering coefficient (C) to get insights into the main features of the evolving networks.

The regional link density ρ_S of region S is defined as the ratio between the total number of links connected to nodes belonging to region S, $e(S)$, and the maximum possible number of links that could be connected to nodes of region S, $e(S)_{max}$, also including the intra-connections of region S:

$$\rho_S = \frac{e(S)}{e(S)_{max}}. \tag{5.4}$$

The cross-regional link density $\rho_{S,T}$ between regions S and T is defined as the ratio between the total number of links connecting region S and T, $e(S, T)$, and the maximum possible number of links that could connect S and T, $e(S, T)_{max}$:

$$\rho_{S,T} = \frac{e(S,T)}{e(S,T)_{max}}. \tag{5.5}$$

Notice that both densities are normalized and thus range between 0 and 1. This normalization is necessary for comparing regions of different sizes, as larger regions are likely to have more links than smaller ones.

For an undirected and unweighted graph, the degree centrality k_i of node i is expressed as

$$k_i = \sum_{j=1}^{N} A_{ij}, \tag{5.6}$$

where N is the total number of nodes in the network and A_{ij} is the entry of the network adjacency matrix $\mathbf{A}$, which equals 1 if nodes i and j are connected, while it is 0 otherwise. The degree centrality is the number of links attached to a given node, i.e. the number of neighbours of the node, and thus represent the significant synchronizations the specific grid point has with the rest of the graph. Thus, nodes with higher degree are characterized by more connections, and, since a link is attributed when a significant synchronization between two locations is detected, nodes with higher degree have more synchronizations.

The clustering coefficient measures the degree to which nodes tend to cluster, i.e. to form closed triangles with their neighbours:

$$C_i = \frac{e(\Gamma_i)}{\frac{k_i(k_i-1)}{2}}, \tag{5.7}$$

where $e(\Gamma_i)$ is the number of existing edges in Γ_i, which is the set of neighbours of node i, and $\frac{(k_i(k_i-1))}{2}$ is the maximum number of possible edges in Γ_i. Thus, the clustering coefficient is normalized between 0 and 1, with $C_i = 1$ meaning that i and its neighbours form a clique, and $C_i = 0$ meaning that there are no links connecting the neighbours of i, i.e. i is the centre of a star graph with its neighbours.

A key issue concerning spatially embedded graphs is that the spatial patterns displayed by any network measure might depend on the artificial boundaries arbitrarily introduced when setting the domain of the study. These boundaries cut all the possible links that would connect the considered grid points with outside regions or with locations at sea or desert not included in the present work. This cause the emergence of boundary effects which artificially modify the spatial patterns of every network measures and thus it is necessary to correct their impacts. Following the work by (Rheinwalt et al., 2012), for every block of the two evolving networks, we construct 1,000 spatially embedded random networks (SERNs) surrogates where each link is assigned based on the probability of observing a link of the same length in the original graph (Giaquinto et al., 2023; Rheinwalt et al., 2012). Afterwards, the boundary effects are estimated for the degree and the clustering coefficient respectively using the average of that specific network measure over the SERNs. The corrected measure is obtained by dividing the original index by the corresponding average one of the SERN surrogates, node-wise. The final corrected measure represents the value of the network index relative to the expected value from the spatial embedding, and thus it is dimensionless.

We assess the evolution of the network indices by looking at their trend across the 51 network blocks. Since the blocks are constructed from overlapping time windows (Figure 5.2), the independence assumption is not satisfied for each node degree and clustering coefficient series. For this reason, we apply the sieve bootstrap method (Kreiss, 1997; Bühlmann, 1997) to test the significance of the detected trends. First, the data are filtered using an autoregressive (AR) process whose order is estimated via the Akaike information criterion form the original data; subsequently, the obtained residuals are repeatedly resampled and used as generating noise of the previously estimated AR process to derive bootstrapped time series. The new bootstrapped time series are designed to have a temporal structure similar to the original data and thus they can be used to perform any statistical test of choice. In our specific case, for each node we simulate 1,000 bootstrapped series of degree centrality and clustering coefficient which we then use to perform a standard t-test to assess the significance of the observed trends (Noguchi et al., 2011).

5.2.7 Geopotential Height composites

To analyse the atmospheric conditions corresponding to the occurrence of compound hot and dry extremes in Europe, we use climate composites. A climate composite represents the average condition of a climate field over specific time periods.

We investigate the Z500 fields during high compound days (HCD), i.e., the top 10% of days, ranked based on the total number of compound events occurrences for each of the regions depicted in Figure 5.1. For instance, the Z500 JJA composite of NEU for the period 1941-1970 is computed as follows: among the 2,760 days (92 days for each of the 30 years), we extract the 276 days for which the number of compound events happened in NEU is highest; the corresponding composites is then obtained by averaging the Z500 field of these selected HCD.

Besides, when the composite is derived for two regions, the set of days used is the one resulting from the intersection of the HCD of the two regions. For instance, the Z500 JJA composite of NEU&WCE for the period 1941-1970 is computed as follows: the 276 HCD selected for NEU and the 276 HCD selected for WCE (as previously described) are intersected to identify the common time steps which are finally chosen to compute the Z500 field average. If the two sets are independent, the common time steps should be ~27, i.e., 1% of the initial 2,760 days.

5.3 Results

5.3.1 Spatial distribution of compound hot and dry extremes

Figures 5.3a-b show the distribution of compound extremes for the JJA and DJF seasons. Summer shows a higher number of compound extremes compared to winter, especially in the center and in the north of the continent. During summer, most locations record 200 events or more, with peaks exceeding 260 occurrences. In contrast, during winter, only a few nodes, primarily in the Mediterranean, reach 200 events, while the rest of the continent generally shows fewer than 100 events per node. Great Britain and southern Scandinavia are major hotspots in JJA, followed by the Po valley, the Hungarian plain and western Russia. During DJF, northern and central Europe are less affected by compound extremes, while the Mediterranean region experiences higher occurrences. If we look at the annual trends (Figures 5.3c-d), most of the significant increasing trends are detected in the Mediterranean in JJA (with the notable exception of eastern Spain). Few locations display a substantial increase of compounds in DJF, while a significant negative trend is detected in western Russia and in some locations in northwestern France, England, Finland and Italy. Since all used time series are detrended (see Section 5.2.1), these observed trends are related to compound events themselves and not to temperature or precipitation increase/decrease. The *p*-values of the observed compound trends are shown in Appendix A, Figure A.1, while the spatial distribution of hot and dry extremes separately are shown in Figure A.2.

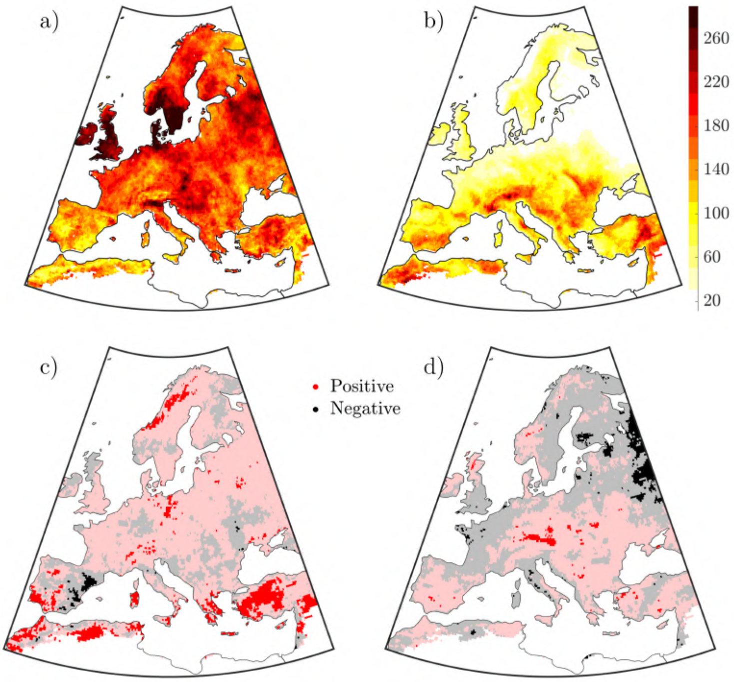

Figure 5.3: **Spatial distribution and trend of compound events.** Number of compound events during 1941 – 2020 for **a)** the JJA season and **b)** the DJF season. Seasonal trend of compound events for **c)** the JJA season and **d)** the DJF season. The fully opaque colour represent a significant trend with $\alpha = 0.05$, while the lighter, semi-transparent colour denotes a non-significant trend.

5.3.2 Evolution of significant synchronizations

Figure 5.4 exhibits the evolution over the 1941-2020 period of the regional link density (the ratio between the number of links connected to the region and the maximum possible number of links that could be connected to the region) and the cross-regional one (the ratio between the number of links connecting two regions and the maximum possible number of links that could connect them) computed from the links attributed in the 51 blocks of the JJA and DJF evolving networks.

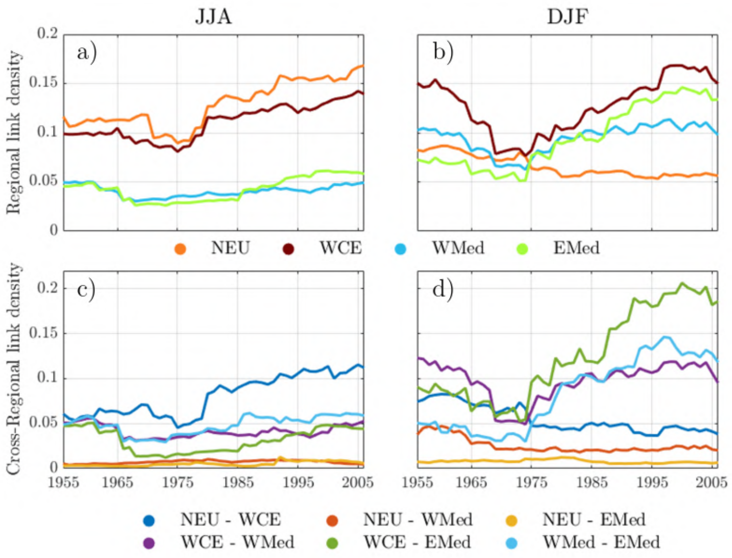

Figure 5.4: **Evolution of link density.** Regional density of the 51 evolving networks blocks for the **a)** JJA and **b)** DJF season. Cross-regional density of the 51 evolving networks blocks for the **c)** JJA and **d)** DJF season. The central year of each network block is used as reference on the x-axis.

The regional density of significant synchronizations rises during summer in the second part of the analysed time period, in particular for NEU and WCE (Figure 5.4a). For these two regions, the density is higher and more rapidly increasing ($\rho_{NEU}, \rho_{WCE} \approx 0.1 - 0.15$) compared to the Mediterranean ($\rho_{EMed}, \rho_{WMed} \approx 0.05$). During winter, the Mediterranean density is higher, as expected from Figure 5.3b, and it is comparable to the WCE one (Figure 5.4b), while NEU shows a decreasing density ($\rho_{NEU} \approx 0.08 - 0.05$), being the only region with a clear negative evolution of significant synchronizations (Figure 5.4b).

During JJA, NEU is strongly connected to WCE with increasing cross-regional density ($\rho_{NEU,WCE} \approx 0.05 - 0.1$), but it shares few synchronizations with the Mediterranean ($\rho_{NEU,WMed}, \rho_{NEU,EMed} \lessapprox 0.01$). WCE maintains a rather stable connection with both WMed and EMed ($\rho_{WCE,WMed}, \rho_{WCE,EMed} \approx 0.05$), which are also well tied together ($\rho_{WMed,EMed} \approx 0.05$, Figure 5.4c); in this latter case, after an initial drop, the cross-regional density increases after the year 1975. During winter, the cross-regional densities evolution changes substantially (Figure 5.4d). WCE and the Mediterranean remain coupled but with more links compared to summer ($\rho_{WCE,WMed} \approx 0.1$) and a stronger increasing trend in the case of WCE-EMed ($\rho_{WCE,EMed} \approx 0.1 - 0.2$). WMed and EMed also show a stronger connection and increasing trend during DJF compared to JJA ($\rho_{WMed,EMed} \approx 0.05 - 0.15$). Conversely, NEU is isolating from the rest of the continent: the NEU-WCE connections decrease and the NEU-EMed and NEU-WMed bonds remain low.

The previous observations are in line with the spatial distributions shown in Figures 5.3a-b: the higher link density of central and northern Europe matches the higher number of compounds for these regions during JJA, while the few occurrences of hot and dry compounds in the north is reflected in the small and decreasing density of NEU during DJF.

5.3.3 Evolution of degree centrality

The average and the evolution of the degree centrality across the 51 network blocks during JJA and DJF over the 1941-2020 period is shown in Figures 5.5 and 5.6, respectively. During summer, northern Europe appears to be the region characterized by the highest number of synchronizations: here, the average degree is higher (Figure 5.5a) with peak values of $k = 2$, while $k = 1$ on average for the rest of the continent. This partly confirms what we observed in the spatial distribution of compound events depicted in Figure 5.3a: a higher number of events results in higher average degree centrality, i.e. more link density and thus significant synchronizations occurrences. Indeed, the regional link density of NEU during JJA is the highest, reaching values above 15% (Figure 5.4a). As for the average degree centrality in DJF, most of the Mediterranean, central western Europe and Great Britain stand out (Figure 5.5b). Some meaningful parallelisms with the distribution of events shown in Figure 5.3b are possible: for instance, we notice the high number of events affecting eastern Turkey and the corresponding large degree ($k \approx 1.4 - 2$), or the similarities concerning the Italian peninsula, where the alpine and Apennines regions are characterized by more events and higher degree ($k \approx 2$) than the Po valley (where $k \approx 1.2$). Nevertheless, the comparison between the number of events and the average number of synchronizations is less trivial in the case of Great Britain, North France and Germany: in this case, the degree centrality appears to be relatively high even if few compounds occurrences are formed. This shows that spatial synchronizations and number of events do not always match. Although being a counter-intuitive scenario from a purely statistical perspective, we should note that the climate system does not operates fully at random, and thus similar mixed situations can be expected (i.e., few events with high synchronicity or numerous events with low synchronicity). More details on this matter can be found in Appendix A (Section A.2). The higher degree centrality which characterizes WCE and the Mediterranean in DJF depicted in Figure 5.5b is also reflected by the relatively high link densities in Figure 5.4b.

Figures 5.6a-b show the detected value of the linear trend for each node across the 51 network blocks for the degree centrality. An increasing degree centrality (positive trend value in Figures 5.6a-b) means a growing number of significant synchronizations

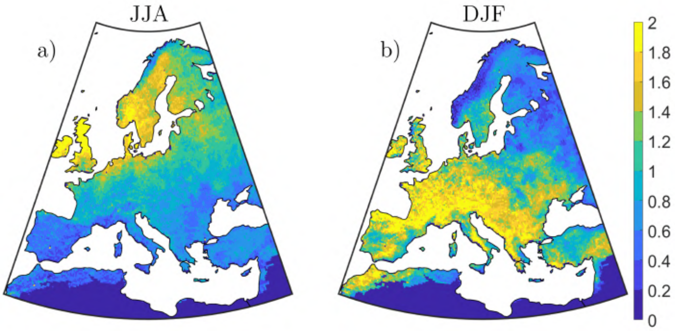

Figure 5.5: **Average degree centrality.** Average value of degree centrality across the 51 network blocks for **a)** JJA and **b)** DJF. The degree centrality is dimensionless because of the correction of bias due to spatial embedding.

for the specific node; conversely, a decreasing degree centrality (negative trend value in Figures 5.6a-b) is indicative of a reduction of synchronizations for the analysed node. Thus, while the regional and cross-regional link densities in Figure 5.4 give us regional information about synchronizations variations, by looking at the degree centrality trends, we are able to assess the evolution of spatially compound events on a local scale. Among the locations characterized by an increasing degree centrality trend during JJA (Figure 5.6a), those located in Finland, northern Poland and the Baltic states particularly stand out (with increases of degree centrality between 2-4%), since in these cases we do not detect a corresponding trend in compounds occurrences (Figure 5.3c). Similarly, some areas display an increasing number of compound (Figure 5.3c), which is not followed by increasing synchronizations (Figure 5.6a), such as in the case of southern Portugal, southern Spain and Northwest Africa. During winter, the differences between compound events and synchronizations evolution is even more pronounced: if on the one hand the negative trend of events in western Russia (Figure 5.3d) is reflected by the decreasing degree centrality trend in the same region (with decreases between 1-2%, Figure 5.6b), on the other hand the degree centrality strongly increases in central southern Europe (with increases up to 5%, Figure 5.6b). Finally, the isolation of NEU in DJF suggested from Figure 5.4d is confirmed by the significant negative degree centrality trend, up to -5% for some locations in NEU (Figure 5.6b). More details on the degree centrality trend significance are given in panels 5.6c-d.

We also analyse the evolution of degree centrality via the empirical distributions depicted in Figures 5.6e-l, for JJA and DJF and for the European regions separately. The EMed distributions are shifting towards higher values of degree centrality both in summer and winter (Figures 5.6k-l). A negative shift is visible in the case of the WMed region during JJA and DJF (Figures 5.6i-j), although not substantial in the latter case. The WCE distribution remains stable in JJA (Figure 5.6g), while it tends to become bimodal in the last period of DJF (Figure 5.6h): indeed, as we can also see in Figure 5.6b, in WCE

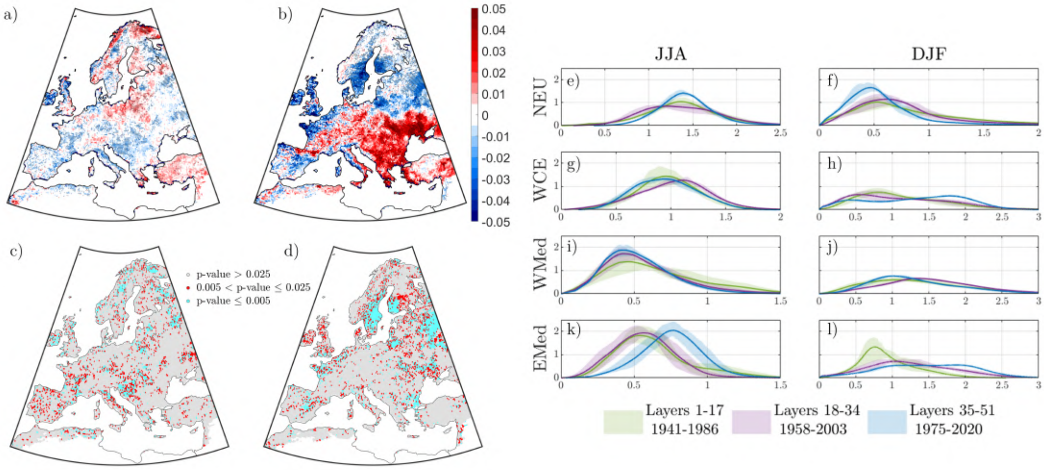

Figure 5.6: **Evolution of degree centrality.** Degree centrality trend for **a)** JJA and **b)** DJF. Dots are drawn if the trend is significant at $\alpha = 0.05$ (two-sided sieve bootstrap t-test). P-values of the detected degree centrality trends for **c)** the JJA season and **d)** the DJF season. **e-l)** Pdfs (empirically estimated via Gaussian-Kernel distributions) of the degree centrality for JJA and DJF and for every European region. The 51 distributions are divided in 3 groups for which we show the average value (solid lines) and 1 s.t.d. confidence bound (shades). The degree centrality is dimensionless because of the correction of bias due to spatial embedding.

we observe nodes with both a significant negative trend (mainly in the northern part of the region) and significant positive trend (in the southeastern part). Finally, in the case of NEU, the degree centrality distribution shifts towards higher values during summer (Figure 5.6e), while the shift is opposite in winter (Figure 5.6f).

Similar results on the evolution of the clustering coefficient index are shown in Appendix A (Figures A.5 and A.6), where we see a higher clustering coefficient during DJF for the entire continent compared to JJA, suggesting a denser and more interconnected synchronizations structure during winter.

5.3.4 Synchronizations and atmospheric conditions

Here we assess the atmospheric conditions during hot and dry compound events by linking Z500 fields composites to the network structure for each European region.

First, we focus on the summer period for NEU and WCE, since these experience most of the events during JJA (see Figure 5.3a).

In Figures 5.7a-d, we present the Z500 composites during HCD – the top 10% of days for number of compound events occurrences – in the first 30 years of our study period, namely 1941-1970, for NEU (Figure 5.7a) and for NEU together with the other regions

(Figures 5.7b-d); Figure 5.7e shows the number of links directed to NEU found in the 1941-1970 network block for each node in Europe, bridging the gap between atmospheric patterns and spatial synchronizations. For the 1941-1970 NEU composite (Figure 5.7a), the Z500 field shows a significant positive anomaly over NEU, with two more ridges over eastern Canada and northeastern Russia, while negative anomalies are shown over northern Canada, Greenland, North Atlantic and western Russia. In the NEU&WCE composite (Figure 5.7b), the positive anomaly over Europe shifts southwards and the previously described high pressure systems intensify, while the negative anomalies over northern America, Greenland and western Russia reduce (Figure 5.7b). Moreover, a trough over Eastern Mediterranean appears. The NEU&WMed composite (Figure 5.7c) displays a bigger European ridge, which extends southwards to western Mediterranean, while relatively negative pressure is still present on eastern Mediterranean; high pressure over western North America and negative pressure over Greenland and western Russia still exist. In the case of NEU&EMed (Figure 5.7d), ridges are located over Scandinavia and northeastern Asia; low pressure is detected over North Pacific, central US, eastern Canada and western Russia. A significant high-low dipole is located over the North Atlantic. Most of NEU synchronizations are shared with WCE (Figure 5.7e); indeed, the corresponding high pressure located over these two areas is significantly high (Figures 5.7a-b). On the other hand, not many links connect NEU with WMed and EMed: while in the case of eastern Europe this is reflected in the composite structure, where the high pressure over NEU is not coupled with a significant pressure over EMed (Figure 5.7d), in the case of NEU&WMed the high pressure, albeit present (Figure 5.7c), does not cause a large number of synchronizations between NEU and WMed (Figure 5.7e).

The 1991-2020 composites (Figures 5.7f-i) show interesting differences in comparison to the 1941-1970 ones (Figures 5.7a-d). While the composites related to events occurred in NEU are quite similar (Figures 5.7a,f), for the NEU&WCE ones the positive anomaly over Europe is stronger in the more recent period by approximately +20 m, and it is also coupled to a +40 m higher pressure in the North Atlantic, as well as a more distinct lower pressure over Greenland (around -70 m compared to the initial period, Figures 5.7b,g). Moreover, while during 1941-1970 compound events in NEU and WCE come with low pressure over Northwest America and high pressure over Northeast Asia, in 1991-2020 the opposite happens (Figures 5.7b,g). As for the NEU&WMed composites, the ridge over WMed gets lower (Figures 5.7c,h). The NEU&EMed composite shows a stronger positive anomaly over high latitudes (up to +100 m compared to 1941-1970) coupled with a more pronounced low pressure over western Europe (about -70 m compared to 1941-1970), and a stronger positive anomaly over Turkey (+20 m, Figures 5.7d,i). The synchronizations patterns in Figure 5.7j reflect the changes of Z500 fields: while NEU and WCE appear to share more connections, synchronizations between NEU and WMed decrease, while there appears an increase of connections between Turkey and NEU and a decrease between the Balkans and NEU. Overall, the atmospheric patterns revealed by these composites confirm what we already outlined in Figure 5.4c: NEU becomes more strongly coupled to WCE in recent time, while getting less connected to the Mediterranean area.

As for the WCE composite of the period 1941-1970 (Figure 5.7k), positive pressure

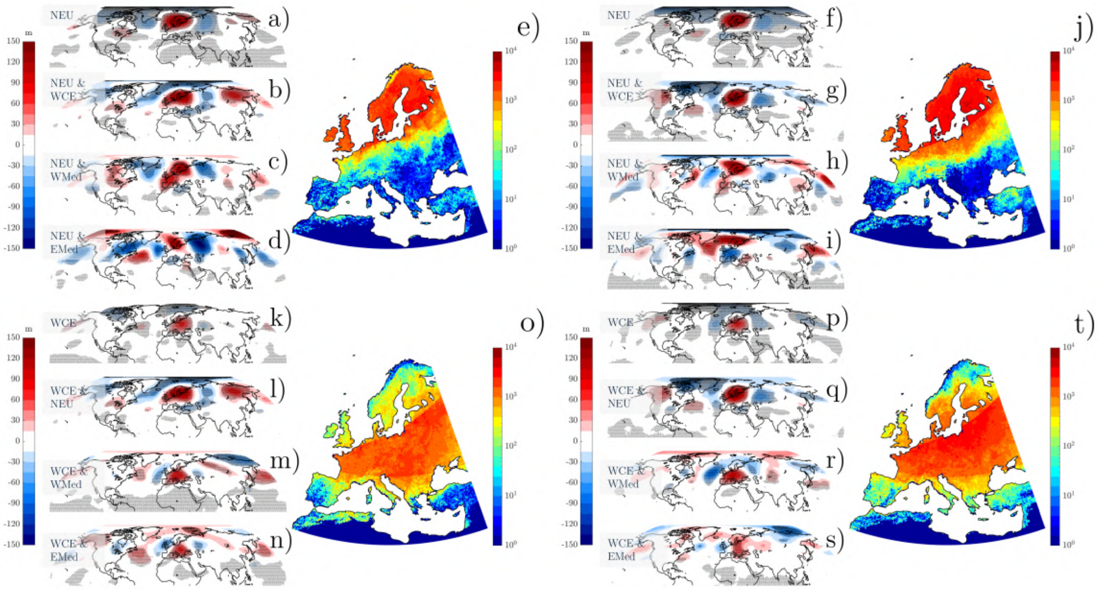

Figure 5.7: **Geopotential height composites and links variations during JJA. a-d)** Z500 composites during HCD for the indicated regions and for the period 1941-1970. **e)** Number of links directed to NEU found in the 1941-1970 network block for each node. **f-j)** Same as panels (a-e), but considering the last 30 years of the analysed period, i.e., 1991-2020. **k-t)** Same as panels (a-j) but with respect to WCE. For all the composites, black dots are drawn if the Z500 anomaly is significant at $\alpha = 0.05$.

anomalies are located over central-eastern Europe, North Atlantic and North Pacific, with low-pressure systems over the Arctic Sea and northern Canada. The WCE&WMed and WCE&EMed composites (Figures 5.7m-n) share key structure similarities: notwithstanding the positive anomaly over central and southern Europe, we notice a positive anomaly over western North Atlantic coupled with a negative one over eastern North Atlantic; other similarities are the positive anomaly over North Pacific and the negative one over western Russia. Some interesting differences are the negative pressure over northern eastern Asia in the WCE&WMed composite and the positive-negative dipole over North America in the case of the WCE&EMed composite. Panels 5.7l and 5.7b, corresponding to the NEU&WCE composites, are the same.

Regarding the WCE composites corresponding to 1991-2020 (Figures 5.7p-s), their structure remains quite similar to the one related to 1941-1970 (Figures 5.7k-n), although with slightly stronger positive anomalies over Europe during the last 30 years (about +30 m higher). Nevertheless, a northeastern Atlantic low-Europe high pattern seems to more prominently emerge (Figures 5.7p-s) compared to what observed during 1941-1970 (Figures 5.7k-n). When looking at the network structure (Figures 5.7o,t), we notice a general increase of WCE connections during the last 30 years compared to the past, which is in line with the stronger positive anomalies found during 1991-2020.

The Z500 composites and links variations for EMed and WMed during JJA are shown in Appendix A (Figure A.7).

Concerning the winter period, we show the results for EMed and WMed, as these appear to be the most severely affected by compound occurrences in DJF (Figure 5.3b) and the regions with a stronger increasing synchronizations trends in this period (Figures 5.4d and 5.6b).

Figures 5.8a-d show the Z500 composites for the period 1941-1970 for EMed (Figures 5.8a) and for EMed together with the other regions (Figures 5.8b-d). The observed patterns are quite similar, with few differences concerning the precise location of ridges and troughs, which however do not change the overall structure: high pressure anomalies are located over central-southern Europe, North Atlantic, northeastern America and North Pacific; low pressure is detected over higher latitudes in Europe, Greenland and northeastern Asia. It is worth mentioning that even for the EMed&NEU composite, the low-high north-south pressure dipole remains, with high anomalies confined in central-southern Europe, reaching Great Britain and Denmark at most. This separation between the South and the North of the continent is reflected in the EMed links structure shown in Figure 5.8e, where we clearly see few connections between NEU and EMed.

During the last 30 years, i.e., 1991-2020, the EMed composites (Figures 5.8f-i) are similar to those related to 1941-1970 (Figures 5.8a-d), but the low-high north-south dipole located over Europe and the Atlantic is more pronounced, except for the NEU&EMed case (Figures 5.8b,g). The connections in 1991-2020 (Figure 5.8j) are higher compared to the initial period (Figure 5.8e), except for those shared between NEU and EMed.

The western Mediterranean composites for 1941-1970 (Figures 5.8k-n) and 1991-2020 (Figures 5.8p-s) show similar features to the EMed ones (Figures 5.8a-d,f-i), with few exceptions. We generally observe high pressure systems over central southern Europe, northeastern America, eastern Russia and North Pacific, while troughs are located over northern Canada, Greenland and western Russia. The major difference between the initial and the last period is the enhanced low-high north-south dipole located over Europe and the North Atlantic during 1991-2020. In terms of synchronizations, in recent times (Figure 5.8t), WMed appears to share more links with EMed and southern WCE, and less with NEU and northern WCE with respect to 1941-1970 (Figure 5.8o). Thus, for both EMed and WMed, their spatial synchronizations increase in the south and decrease with northern regions; this is accompanied by a strengthened negative pressure in northern Europe and North Atlantic and positive pressure over central and southern Europe.

The Z500 composites and links variations for NEU and WCE during DJF are shown in Appendix A (Figure A.8).

The described changes in compound synchronizations structure due to large scale atmospheric patterns are most likely related to the impact of pressure anomaly on temperature and precipitation due to land-atmosphere feedbacks. Indeed, the consequent increase and/or decrease of temperature and precipitation intensity drive the occurrence of compound hot and dry events. Hence, we explore the connection between the atmo-

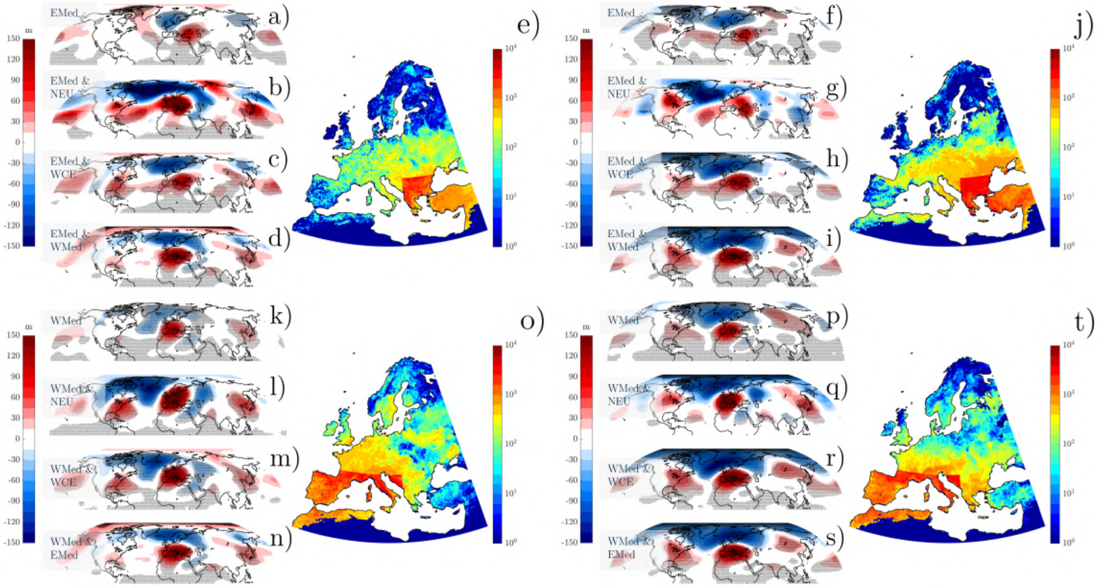

Figure 5.8: **Geopotential height composites and links variations during DJF. a-d)** Z500 composites during HCD for the indicated regions and for the period 1941-1970. **e)** Number of links directed to EMed found in the 1941-1970 network block for each node. **f-j)** Same as panels (a-e), but considering the last 30 years of the analysed period, i.e., 1991-2020. **k-t)** Same as panels (a-j) but with respect to WMed. For all the composites, black dots are drawn if the Z500 anomaly is significant at $\alpha = 0.05$.

spheric patterns described here and temperature and precipitation intensity changes in the next Section 5.3.5.

5.3.5 Temperature and precipitation conditions during high compound days

To clarify how atmospheric patterns associated with Z500 anomaly are connected to the intensity of compound extremes, we analyze temperature and precipitation anomalies during HCD for each studied region. Specifically, we conduct this analysis for compound events in NEU and WCE during JJA, and for compound events in WMed and EMed during DJF. Thereby, we are able to connect the atmospheric regime to the intensity of compound events in two ways: (i) examining changes in temperature and precipitation distributions during HCD compared to the entire JJA or DJF season, and (ii) analyzing temperature and precipitation composites during HCD, so to get a spatial information of temperature and precipitation changes. The analysis is conducted for both the first and last 30 years of the study period, following the same approach used to derive Figures 5.7 and 5.8, to facilitate comparison between the two periods.

In Figure 5.9, we focus on temperature and precipitation intensity in JJA for the NEU region. In the first 30 years (top panels), NEU temperature anomalies during HCD (Figure 5.9a, red histograms) are shifted towards higher values compared to all JJA seasons (black histograms). The 95th percentile of the temperature anomaly across all JJA seasons, T^*, is exceeded by definition 5% of the time. However, during HCD, the exceedance frequency of T^* increases to 18%. This is reflected in the temperature composite shown in Figure 5.9b, where temperatures are substantially higher over NEU and northern WCE, while significant low values are observed over EMed.

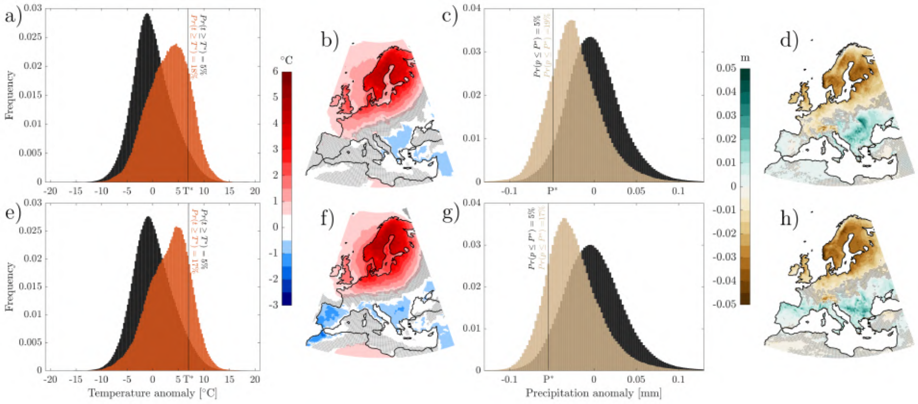

Figure 5.9: **Temperature and precipitation anomalies for NEU in JJA. a,c)** Normalized histogram plots of temperature (a) and precipitation (b) for the JJA season in 1941-1970 (black histograms) and for HCD (temperature in red and precipitation in brown). The black line indicates the 95th (5th) percentile T^* (P^*) of the complete JJA temperature (precipitation) distribution. The probability of exceeding this temperature (precipitation) level during HCD is shown in red (brown). **b,d)** Temperature (b) and precipitation (d) composites during HCD. Black dots are drawn if the anomaly is not significant at $\alpha = 0.05$. **e,h)** Same as (a-d) but for 1991-2020.

Regarding NEU precipitation during the first 30 years, drier conditions are detected during HCD, with the probability of precipitation falling below the 5th percentile of the full period, P^*, reaching up to 19% (Figure 5.9c). Consistently, the precipitation composite indicates dry conditions over NEU (Figure 5.9d), particularly in southern Norway, Sweden, and southern Finland, as well as in parts of the Alpine region. Conversely, significantly high precipitation is observed over EMed.

In the last 30 years (bottom panels of Figure 5.9), both temperature and precipitation anomalies over NEU exhibit more extreme conditions. Probabilities of exceeding T^* and falling below P^* remain elevated (Figures 5.9e,g), though they are lower compared to the 1941–1970 period. In this regard, we highlight that the background distributions (black histograms) slightly differ between the first and last 30 years. While the original data are detrended (see Section 5.2.1), differences persist in the distribution tails, with the more recent period generally showing higher variance. For further details, please see Figure A.12 for NEU and Figures A.13–A.15 for other regions in Appendix A.

The temperature anomaly is higher over NEU during 1991–2020 (Figure 5.9f) compared to 1941–1970 (Figure 5.9b). However, cooler conditions are detected over Mediterranean regions, particularly in the west. Precipitation decreases over NEU during 1991–2020 (Figure 5.9h) compared to 1941–1970 (Figure 5.9d). This highlights the direct connection between the high-pressure systems shown in Figures 5.7a,f and the intensity of extremes during HCD, as illustrated in Figure 5.9. Indeed, large-scale atmospheric circulation patterns can drive the occurrence of both hot and dry extremes (Ionita et al., 2021a), with high-pressure systems often leading to elevated temperatures and reduced precipitation (Kautz et al., 2022a), as we also discuss in more details in Section 5.4. This connection is further reflected in the structure of NEU compound synchronizations: during more recent times, NEU shows stronger coupling with WCE and weaker connections to the Mediterranean area, consistent with the changes in temperature and precipitation composites depicted in Figures 5.9b,f and 5.9d,h.

We find similar results for the other regions. Indeed, it is possible to notice strong connections between Z500 composites, temperature and precipitation intensities, and network structure. The figures showing temperature and precipitation intensities for WCE in JJA and for WMed and EMed in DJF are included in Appendix A (Figures A.9–A.11).

5.3.6 NAO and SNAO patterns during high compound days

We further check the relationship between NAO intensity and compound occurrences during DJF in WMed and EMed regions, as well as between SNAO intensity and compound occurrences during JJA in NEU and WCE regions.

First of all, we notice that while the intensity of the daily NAO index in DJF increases during 1991–2020 compared to 1941–1970 (Figure 5.10a), the daily SNAO index does not show a similar trend during JJA, being characterized by more negative extremes and only few more positive events during recent times (Figure 5.10b).

When comparing the NAO intensity in 1941–1970 with NAO intensity during high compound days (HCD) in the same period for WMed and EMed, we only notice minor differences (see yellow and blue distributions in Figures 5.10c,e). Conversely, in more recent times, these differences increase both in the case of WMed and EMed, with a clear increase of NAO+ conditions during HCD happening in WMed and EMed (violet and red distributions in Figures 5.10c,e).

Figure 5.10d shows the SNAO intensity during NEU HCD, both in the case of 1941–1970 (yellow and blue distributions) and 1991–2020 (violet and red distribution). We notice that during HCD the daily SNAO is more likely to be in a positive phase for both period compared to average conditions. In the case of WCE HCD (Figure 5.10f), we do not find considerable differences between SNAO average intensity and SNAO intensity during HCD, although few more SNAO+ events during recent times are detected during HCD (right tail of the distributions in Figures 5.10f).

We also explore the prevalence of high compound days during months with high NAO/SNAO intensity, as reported in Figures 5.11 and 5.12. Here, we call $\overline{HCD_m}$ the

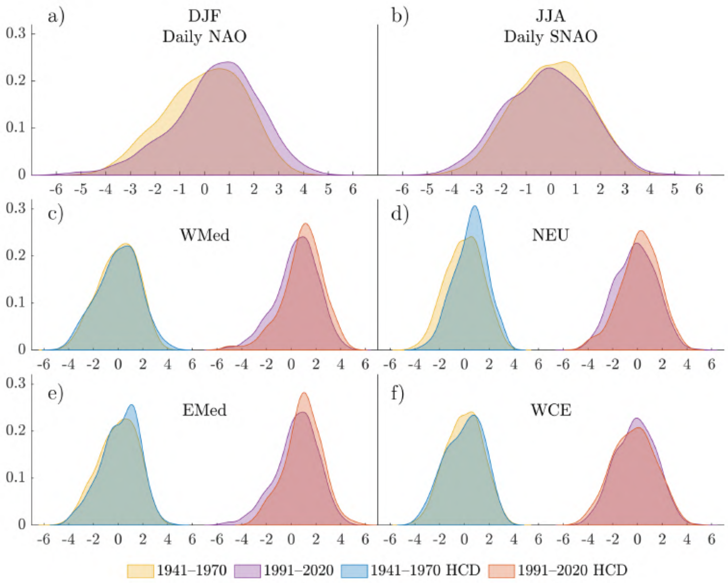

Figure 5.10: **The evolution of daily NAO and SNAO indices and their realtion with high compound days.** **a)** Daily NAO intensity evolution in DJF between 1941–1970 (yellow distribution) and 1991–2020 (violet). **b)** Same as (a) but for the SNAO daily index in JJA. **c)** Comparison between daily DJF NAO intensity during 1941–1970 (yellow) and daily DJF NAO intensity during WMed HCD in 1941–1970 (blue) and analogously for 1991–2020 (violet) and WMed HCD in 1991–2020 (red). **d-f)** Same as (c) but for JJA SNAO index and NEU HCD, DJF NAO index and EMed HCD and JJA SNAO index and WCE HCD, respectively.

expected number of HCD occurring in a month if HCD were uniformly distributed in time. Red dots represents months whose number of HCD $HCD_m \geq \overline{HCD_m}$, while blue dots are months where $HCD_m < \overline{HCD_m}$. In Figure 5.11, the HCD_m is plotted against the value of the DJF monthly NAO index for the WMed and EMed regions and distinguishing between 1941–1970 and 1991–2020, showing the dependence of HCD to NAO intensity. In Figure 5.12 we do the same but for NEU and WCE regions and for the JJA monthly SNAO index.

In the case of WMed and EMed, we see that while during the initial 30 years there is not a clear distinction between months with numerous HCD and months with low HCD with respect to NAO intensity (Figures 5.11a,c), during 1991–2020 months with numerous HCD are also characterized by higher NAO compared to lower HCD months (Figure 5.11b,d).

In the case of NEU and WCE and SNAO, this relationship is less prominent for both periods. In particular, while for NEU is it possible to notice a slight increase of SNAO monthly intensity during months with higher number of HCD (Figures 5.12a-b), in the case of WCE there is a negligible, if ever, difference (Figures 5.12c-d).

The same approach used to derive Figures 5.11 and 5.12 is applied by using a season based procedure. The results are similar and are displayed in Appendix A (Figures A.16-A.17).

5.4 Discussion

By now, many scientific works have identified Europe as one of the major heatwave hotspot in the Northern Hemisphere (Kornhuber et al., 2019; Mitchell et al., 2019; Robine et al., 2008; Ballester et al., 2023). However, wet and dry conditions and their evolution due to global warming are less trivial, owing to the high spatio-temporal variability of extreme precipitation and droughts in Europe (Copernicus Climate Change Service, 2024c). For this reason, when dealing with hot and dry extremes and their concurrences, it remains challenging to untangle the numerous drivers involved. Thermodynamic mechanisms are usually not enough to explain what we observe and dynamical processes, such as anomalous circulation patterns, play a key role in this context (Coumou et al., 2014; Di Capua et al., 2021; White et al., 2022).

Large-scale atmospheric patterns can act as dynamic drivers of hot and dry conditions. As a matter of fact, high-pressure systems are typically associated with subsidence and clear-sky conditions. This has a twofold effect: (i) the incoming solar radiation increases, resulting in higher surface temperatures (Tian et al., 2023), and (ii) precipitation reduces due to decreased cloud cover. Under these conditions, the atmospheric circulation coupling (Lesk et al., 2021) –the negative correlation between temperature and precipitation– is intensified, also due to the role of soil moisture (Berg et al., 2015). The lack of precipitation caused by clear skies reduces soil moisture (Seneviratne et al., 2010), which in turn enhances surface sensible heat fluxes (Bartusek et al., 2022), further elevating surface temperatures (Trenberth and Shea, 2005). All these mechanisms contribute to the direct physical relation between high pressure and temperature and precipitation extremes, thus enhancing compound hot and dry events.

Our findings are in line with previous studies where atmospheric patterns are identified as drivers behind different types of spatially compound events (De Luca et al., 2020; Kornhuber et al., 2020; Ye and Messori, 2020), as we show in the case of European regions (Figures 5.7-5.9 and Figures A.7-A.11 of Appendix A). In addition, we quantify and locate the evolution of hot and dry compound synchronizations at the continental, regional and local scale in Europe, distinguishing between the boreal summer and winter seasons. This distinction is crucial, since the climatological features and the atmospheric patterns related to these two seasons are fundamentally different, as it is also highlighted by our findings.

We find that, during summer, Great Britain, south Scandinavia, the Po valley, the Hungarian Plain and western Russia are the major hotspots for compound events (Figure 5.3a), while the Mediterranean exhibits most of the significant increasing occurrences trends (Figure 5.3c). This is partly reflected in the synchronizations detected in the JJA evolving network: Scandinavia and Great Britain are indeed affected by a large link density (Figure 5.4a, NEU) and a high average degree centrality (Figure 5.5a); in terms of synchronizations trends, a positive degree centrality trend is detected for England, Scandinavia and the Baltic states (Figures 5.6a), albeit neither strong nor significant in most cases. In the Mediterranean, the East shows a degree centrality increase while the West shows a slightly decrease (Figures 5.6a).

NEU and WCE appear to be the two regions more strongly connected, with a high and increasing cross-regional link density, especially in the second half of the analysed period (Figures 5.4c). To corroborate the strengthened NEU and WCE linkage in summer, we find that the geopotential height anomaly corresponding to HCD in these two regions gets stronger in recent times over Europe by approximately 25-30 m (Figures 5.7b,g and 5.7l,q). This is directly associated to temperature and precipitation extreme conditions: during HCD, the frequency of temperature and precipitation extremes increases from 5% to 17% in NEU and from 5% to 13% in WCE in 1991–2020 (see Figures 5.9 and A.9 of Appendix A). The geopotential height composite also reveal dynamical changes, with higher pressure in the North Atlantic and lower pressure over Greenland (Figures 5.7b,g and 5.7l,q). This tendency closely resembles the positive phase of the summer North Atlantic Oscillation (Folland et al., 2009) (SNAO+), which is associated with summer climate variability over Europe and, in particular, with warm and dry conditions over the UK and Scandinavia (Folland et al., 2009; Linderholm et al., 2009). SNAO+ was indeed one of the major drivers behind the 2018 summer European heatwave (Rousi et al., 2023). Several studies (Folland et al., 2009; Bladé et al., 2012; Rousi et al., 2021) agree on the increase of SNAO+ during the recent past, which would explain the stronger pressure anomaly we observe in Figure 5.7g compared to Figure 5.7b, leading to more compound synchronization between NEU and WCE (Figures 5.7e,j and 5.7o,t). The increase in SNAO+ could be also the reason behind the relatively low number of connections between NEU and the Mediterranean (Figure 5.7e), which decreases even more in the last 30 years (Figure 5.7j), especially in the case of WMed and the Balkans. SNAO+ is in fact associated with wet conditions in southern Europe, especially in the Eastern Mediterranean region (Mariotti and Arkin, 2007; Folland et al., 2009; Linderholm et al., 2009), and this relation is expected to increase (Bladé et al., 2012). In point of fact, by comparing the composites in Figures 5.7a-b with the respective ones in Figures 5.7f-g, we notice that the negative pressure anomaly over the Mediterranean becomes stronger (decreasing by approximately 20-25 m) and more significant in recent times. As for the atmospheric conditions related to WCE events in JJA (Figures 5.7k,p), we still observe lower pressure over Greenland and higher pressure over northern Europe in the last 30 years, which could still indicate a stronger SNAO+ condition. However, we do not observe a clear temporal trend in SNAO daily index between 1941–1970 and 1991–2020 (Figure 5.10b), and yet we do find it to be more intense during HCD in NEU during both time periods (Figure 5.10d), with NEU HCD more frequent during months with stronger SNAO (Figure 5.12a-b). Regarding the Mediterranean, thermodynamical effects and local land-atmosphere feedback could be more important to explain hot and dry extremes and their trends compared to northwestern Europe (Suarez-Gutierrez et al., 2020; Rousi et al., 2022).

During winter, the Mediterranean appears to be the most affected region by hot and dry events (Figure 5.3b). Indeed, the regional link density is higher in southern and central

Europe (Figure 5.4b) as well as the degree centrality (Figure 5.5b), especially on the west. Moreover, EMed and many nodes in WCE are dominated by an increasing degree centrality (Figure 5.6b), although few of these locations display a compound increase (Figure 5.3d). NEU appears to be the only region with a clear decrease of significant synchronizations: its regional link density declines (Figure 5.4b) together with the NEU-WCE cross-regional link density (Figure 5.4d). Indeed, a low and decreasing degree centrality is detected in NEU, except for Great Britain, where, although decreasing, the degree centrality appears high on average (Figures 5.5b and 5.6b).

By looking at the atmospheric conditions related to compound events during DJF in the Mediterranean, we notice that the increase of EMed and WMed spatial synchronizations (Figures 5.8e,j and 5.8o,t) comes along with a lower pressure in North Europe and North Atlantic and a higher pressure over central southern Europe and tropical North Atlantic, with a more pronounced low-high north-south dipole located over Europe (Figures 5.8a-d,f-i and 5.8k-n,p-s). This pattern could be related to winter NAO, and in particular to its positive phase. NAO+ is associated with lower winter precipitation and higher temperatures over the Mediterranean (Rousi et al., 2020) and it is also expected to have a positive trend (Rousi et al., 2020, 2017, 2021; Linderholm et al., 2009). Moreover, since NAO+ has an opposite effect over northern latitudes, causing higher than usual precipitation (Rousi et al., 2020), it could explain the few detected compound synchronizations between NEU and the south and the associated negative trends (Figures 5.4d, 5.6b and 5.6f). In our study, we do find a positive trend of NAO intensity during the 1991–2020 compared to 1941–1970, as we show in Figure 5.10a. On top of that, we show that while NAO intensity is stable in 1941–1970 if we consider HCD in both WMed and EMed, during 1991–2020 NAO+ conditions are more frequent during HCD in the Mediterranean (Figures 5.10c,e). This is also confirmed by the higher number of Mediterranean HCD in 1991–2020 during months with stronger NAO (Figure 5.11).

Several atmospheric variability patterns could potentially influence wintertime climate in Europe together with NAO. For instance, (Madonna et al., 2021) explore in details the association and the impacts of NAO, blocking and jet streams over Europe, showing that these could be coupled to amplify hot and dry conditions at the surface or, conversely, cause opposite effects. In their study, (Mellado-Cano et al., 2019) explore the interactions between east Atlantic (EA) pattern and NAO and their impacts on Europe climate variability. They show that the simultaneous occurrence of EA and NAO positive phases in winter is significantly correlated with higher than average temperatures over most of central and southern Europe, low precipitation over most of the Mediterranean and high precipitation over the British Isles and Scandinavia. This is in line with our findings and demonstrate that the interplay among different atmospheric patterns is also relevant for extremes occurrences.

Climate change and its impacts on atmosphere dynamics could potentially foster the simultaneous occurrences of hot and dry extremes at different locations. As previously discussed, the NAO plays a key role in shaping weather and climate conditions in Europe, and previous studies indicates that its changes in amplitude and centre location may result from human induced climate change (Rousi et al., 2020). The weakening of the Atlantic meridional overturning circulation could also cause the increase of compound events, by triggering extreme heatwaves over central Europe in summer and enhanced storm track activity toward northwestern Europe in winter (Rousi et al., 2021). Another important mechanisms to take into account is the persistence of double jet streams over Europe, which (Rousi et al., 2022) found to have an upward trend responsible for the accelerated heatwave increase in western Europe. Finally, Artic amplification (the accelerated warming of the Artic) is connected to persistent weather patterns in mid-latitudes, which lead to an increased probability of extreme weather events (Francis and Vavrus, 2012).

All these examples show, on the one hand, how intricate the relations between different atmospheric patterns may be, but, on the other hand, they demonstrate the clear connection between global warming, atmosphere dynamics and weather extremes in Europe. With our study, we further expand these observations, linking them to the consequent rise of SCHADE events synchronizations. Our approach allow us to identify and quantify the synchronizations of these extremes for different regions in Europe and seasons. The evolving network framework is key to analyse the temporal and spatial variations of hot and dry extremes concurrences and locate them to the continental, regional and local scale.

5.5 Conclusions

In this study, we explore the evolution of spatially compound hot and dry extremes in Europe for boreal summer (JJA) and winter (DJF) during the period 1941-2020 in ERA5, using concepts and methods derived from network theory. Our results show that the distributions of compound extremes and their synchronizations strongly vary between the two seasons and European regions as well. We reveal that the increase of compounds frequency and synchronizations do not always coincide. Some locations are exposed to an increasing number of extremes which are not becoming more synchronized. For other areas the spatial concurrences are growing although compounds frequency is not significantly rising.

This work highlights spatio-temporal features of compound hot and dry extremes, specifically focusing of the co-occurrences of these events at different locations. This is crucial to distinguish the effects of climate change on the spatial relations among these events, more than on the extremes themselves, and to understand more about compounds dynamics, given their intrinsically higher risk due to the combinations of the impacts. We applied our framework to hot and dry events in Europe and analyse their characteristics, but the same approach could be employed for other types of compound weather and climate events.

In the future, this analysis could be further expanded by explicitly considering the intensity and duration of the studied extremes, and see how these aspects impact the spatio-temporal structure of synchronizations. Moreover, our approach could be easily applied to future climate projections, in order to assess if and how compounds features are going to change under different Shared Socioeconomic Pathways for specific regions. This could not only improve our understanding of these phenomena, but potentially support in extreme events predictions, improving forecasting schemes and adaptation strategies at key locations.

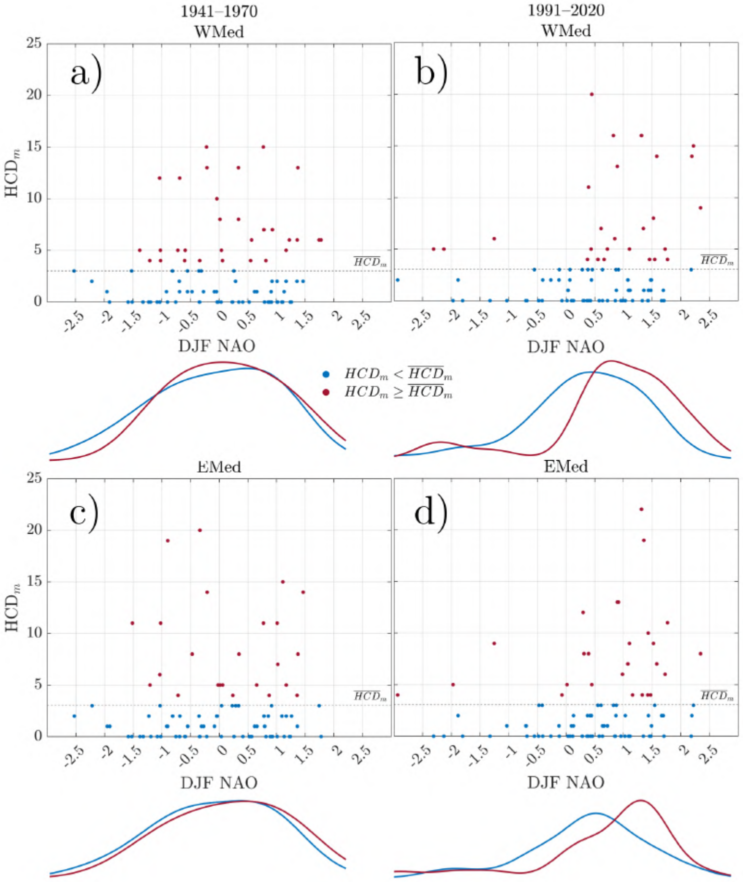

Figure 5.11: **Monthly HCD Vs. monthly NAO index.** **a)** Scatter plot of the number of HCD in WMed during one month (HCD_m) and the corresponding value of the DJF monthly NAO index for the 1941–1970 period. Red dots are months whose HCD_m is higher than the expected number of HCD if HCD where uniformly distributed in time ($\overline{HCD_m}$). Marginal distributions of the NAO index of red and blue dots are depicted below the graph. **b)** Same as (a) but for WMed during 1991–2020. **c)** Same as (a) but for EMed during 1941–1971. **d)** Same as (a) but for EMed during 1991–2020.

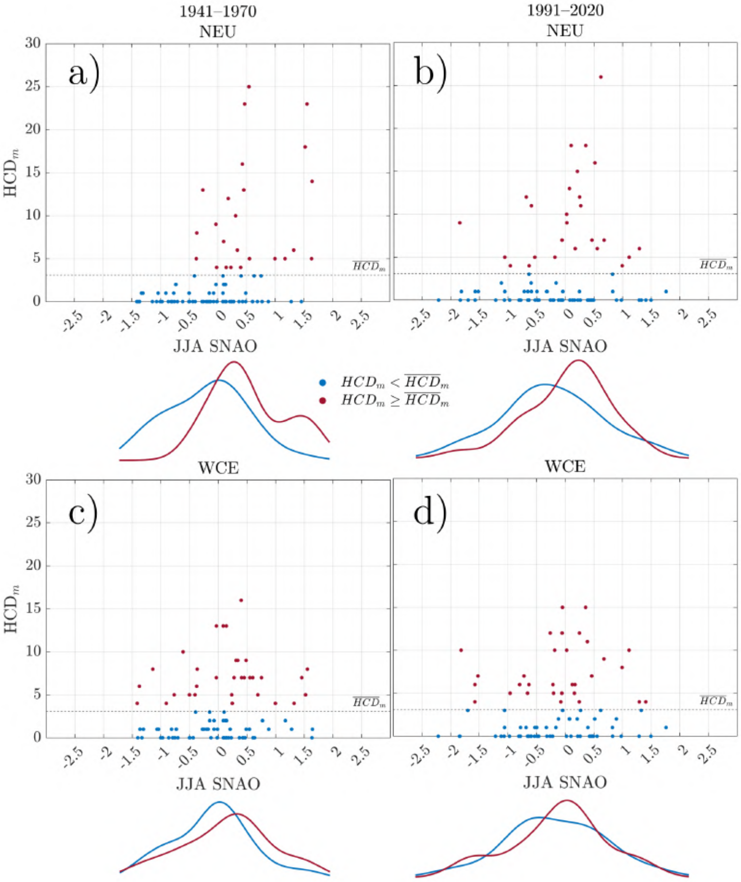

Figure 5.12: **Monthly HCD Vs. monthly SNAO index.** **a)** Scatter plot of the number of HCD in NEU during one month (HCD_m) and the corresponding value of the JJA monthly SNAO index for the 1941–1970 period. Red dots are months whose HCD_m is higher than the expected number of HCD if HCD where uniformly distributed in time ($\overline{HCD_m}$). Marginal distributions of the SNAO index of red and blue dots are depicted below the graph. **b)** Same as (a) but for NEU during 1991–2020. **c)** Same as (a) but for WCE during 1941–1971. **d)** Same as (a) but for WCE during 1991–2020.

6 Causal effect networks of compound hot and dry extremes in central Europe

Adapted from *Tian*, Y., Giaquinto*, D., Di Capua, G., Claassen, J., Ali, J., Li, H., De Michele, C.: Historical changes in the Causal Effect Networks of compound hot and dry extremes in central Europe*, accepted for publication by Communications Earth & Environment.

*These authors contributed equally to this work.

Abstract Changes in hot and dry extremes in central Europe have been attributed to atmospheric circulation anomalies and land-atmosphere interactions. However, the strength of the underlying causal links and their historical trends have not been quantified. Here, we use Causal Effect Networks (based on the Peter and Clark momentary conditional independence algorithm) and show that hot extreme events in central Europe are driven primarily by anomalous atmospheric patterns and soil water deficiency. Dry extreme events are mainly induced by anomalous atmospheric patterns and soil moisture memory, and only marginally by temperature changes. We find that in the period 1979-2020, the influence of dry soil on temperature has been amplified by 67% during compound hot and dry extremes, while the impact of atmospheric drivers on soil moisture has intensified by 50% (36%) during compound (single) extremes. This work highlights the strengthened causal links of compound hot and dry extremes with their underlying drivers under global warming, which can lead to non-linear interactions and increase adaptation challenges.

6.1 Introduction

Anthropogenic global warming continues to set new records. 2023 was the warmest calendar year on record: for the first time, the mean global surface temperature has exceeded every day 1°C above the pre-industrial level (Copernicus, 2024). Accordingly, 2023 boreal summer (June, July, and August) was the warmest season, with August and July 2023 being the warmest months in the ERA5 data record (Copernicus, 2024). In Europe, while the 2022 summer was the hottest ever recorded, summer 2023 was the fifth warmest, with temperatures 0.83°C higher than average (Copernicus, 2023a).

Heatwaves pose a serious threat to human health, as shown by the increase of high temperature-related fatalities in Europe (Baldwin et al., 2019). According to the World Meteorological Organization, heatwaves are the most impactful weather hazard in Europe by far, being responsible for up to 93% of deaths resulting from weather-, climate- and water-related extremes in the 1970-2019 period (WMO, 2021). Furthermore, the occurrence of European heatwaves has increased almost four times faster compared to the rest of the northern midlatitudes over the past 42 years, making Europe one of the main heatwave hotspots worldwide (Rousi et al., 2022). According to Zschenderlein et al. (2019), the most prominent physical mechanisms that lead to the occurrence of heatwave are adiabatic heating following subsidence, advection of warm air at the surface level, and diabatic heating due to surface sensible heat fluxes or incoming solar radiations (Röthlisberger and Papritz, 2023). The combination of adiabatic warming and high radiative heating due to clear-sky conditions could lead to persistent and intense anomalous Rossby waves, thus enhancing the increase of surface temperatures (White et al., 2022).

If on the one hand it is straightforward to understand that a warmer atmosphere leads to higher surface temperatures, its impact on wet–dry conditions is more complex. According to thermodynamics principles, air moisture holding capacity increases with warmer temperatures (Robinson et al., 2021; Lehmann et al., 2015), thus assuming constant relative humidity and neglecting dynamical aspects, more rainfall extremes due to global warming are expected. Nevertheless, high temperatures often sustain dry conditions as well, leading to water scarcity and soil moisture depletion, following a positive soil moisture–temperature feedback process (Vogel et al., 2018; Miralles et al., 2014). The dual increase of these extreme conditions was manifested in Europe during 2023, where high temperatures led to dry soils and drought conditions in the southern part of the continent, with the spreading of numerous wildfires across the Mediterranean region, while a large part of central Europe and Scandinavia suffered from intense precipitation, often followed by flooding (Copernicus, 2023b).

Therefore, given the numerous mechanisms behind drought developments, it is crucial to distinguish among different types of water scarcity, whether they are related to a lack of precipitation, soil humidity, water or groundwater discharge, and freshwater availability for society. The aforementioned drought definitions are associated with different variables and could be driven by different atmospheric processes (Seneviratne et al., 2012; Wilhite and Glantz, 1985). A direct impact of climate change on precipitation decline has been detected for the Mediterranean region (Spinoni et al., 2020), while dry conditions over central and northern Europe are likely more related to the increased evaporative losses and reduced soil moisture caused by warmer temperatures (Cook et al., 2018; Vogel et al., 2018).

The impacts and cascading effects of drought events also depend on the timescales at which these events develop. Generally, droughts are slowly evolving phenomena, which are usually evaluated on a monthly basis (Spinoni et al., 2015a). However, low levels of precipitation combined with extreme temperatures can result in fast transitions to dry conditions on sub-monthly scales, leading to flash droughts (Otkin et al., 2018). These dry extremes recently gained attention due to their devastating and sudden impacts on crop yields and water supply all around the globe (Hoerling et al., 2014; Yuan et al., 2018; Wang et al., 2016), as soil water content is strongly affected due to the abrupt increase of evaporative demand (Mo and Lettenmaier, 2020). To capture the short duration of flash droughts, previous studies have analysed these events setting the temporal resolution to the pentad scale, i.e. a series of 5 consecutive days (Mo and Lettenmaier, 2015; Christian et al., 2021), also in line with the typical duration of hot extremes, which develop on timescales of at least 3 days (Russo et al., 2015; Perkins and Alexander, 2013). Therefore, the pentad timescale is also adopted in this study to capture both hot and dry conditions.

When heatwaves and droughts co-occur, their impacts can be exacerbated, leading to more serious negative effects both on the ecosystem and society. For instance, co-occurring heatwaves and droughts can lead to a higher likelihood of crop failures, tree mortality, wildfires, reduced steamflow, and greater water shortage (Bevacqua et al., 2022). Such co-occurring extremes have been classified as compound events, i.e. situations where two or more hazards/drivers co-occur and are responsible for enhanced weather and climate-related impacts (Baldwin et al., 2019; Ionita et al., 2021b; Zscheischler et al., 2020b).

Throughout the last decade, an increase in hot and dry events has been observed globally (Ionita et al., 2021b; Mukherjee et al., 2023), and this increasing trend is expected to continue with global warming (Vogel et al., 2019). Therefore, it is urgent to quantify the joint occurrence of these hazards, as highlighted in the IPCC 6th assessment report (IPCC, 2023; Tripathy et al., 2023), and to investigate the interdependencies between different drivers of hot and dry compound events, aiming at reducing their impacts with more accurate predictions and early warning systems (Mukherjee et al., 2023).

Compound hot and dry events can be triggered by both local and large-scale drivers on a variety of temporal scales. Mukherjee et al. (2023) identify local conditions such as vapor pressure deficit, potential evaporation, and precipitation as important variables. Next to thermodynamic ones, dynamic drivers such as large-scale atmospheric circulation patterns have been identified (Ionita et al., 2021b) as precursors of hot and dry events as well: the prevalence of long-lasting high-pressure systems often leads to prolonged hot conditions and reduced precipitation (Kautz et al., 2022b). However, the complex interactions between local thermodynamic effects and large-scale remote atmospheric drivers may also influence the intensity and duration of compound hot and dry extremes (Lesk et al., 2021). Hence, understanding the causal relationships between both local and larger-scale climate drivers for a specific region can provide a holistic understanding of these events.

Recent studies have investigated the drivers of compound hot and dry events by using probabilistic methods to assess the dependence between the two (Zscheischler and Seneviratne, 2017; Bevacqua et al., 2022). A clear distinction between the mechanisms behind single and compound extremes could be beneficial to improve sub-seasonal to seasonal forecasts and to implement appropriate adaptation measures. Moreover, the detection and quantification of causal pathways of compound events remains an open question.

Causal analysis has been gaining attention in the field of climate science as it has shown to be useful to deepen our understanding of the physical relationships among various processes and variables of the Earth system. Indeed, causal algorithms are capable of detecting directional dependencies ruling out spurious correlations resulting from random coincidence (Docquier et al., 2024). Several causal methods have been applied to Earth System Science (Su et al., 2023). For instance, traditional Granger causality (Granger, 1969; Bach et al., 2019) is based on linear auto-regressive models to address bivariate causal associations. If on the one hand this interpretation of the model is straightforward, on the other hand it is limited to linear and stationary bivariate time series (Su et al., 2023). Moreover, if the system under study is made by weakly coupled subsystems, Granger causality may fail (Yang et al., 2023). In this case, more refined methodologies, like convergent cross mapping (CCM) (Sugihara et al., 2012; Vannitsem and Ekelmans, 2018) may help, enabling the detection of causality in deterministic nonlinear dynamic systems with weak to moderate couplings and non-separable variables (Wang et al., 2024).

Here, we employ Causal Effect Networks (CENs) obtained with the Peter and Clark momentary conditional independence (PCMCI) algorithm (Runge, 2018), a method based on the conditional independence framework which allows to investigate causal associations in large time series datasets. In the context of our analysis, PCMCI offers several strengths with respect to other methodologies like CCM. First of all, it is suited to handle conditioning on multiple variables without excessive computational cost, making it a practical choice for complex, large-scale data. Moreover, it can be applied both in a linear and nonlinear manner, making it more flexible to different research scenarios. In the present study, we employ it under a linear framework, in conjunction with conditional partial correlation. This is done to allow a clear interpretation of the found relationships, bridging the gap between statistical analysis and physical mechanisms. PCMCI has successfully been applied to detect causal relationships in the Earth system, such as the boreal summer tropical – extratropical links (Di Capua et al., 2020c), the Atlantic hurricane activity (Pfleiderer et al., 2020), polar vortex dynamics (Kretschmer et al., 2017), the North Atlantic Oscillation and Mediterranean winter temperatures (Hatzaki et al., 2023) and the Indian summer monsoon (Sharma et al., 2023).

Hence, in this study we aim to (i) quantify the causal links from potential remote and local drivers to single and compound hot and dry extremes in central Europe, (ii) assess the prediction power of the identified causal drivers, and (iii) investigate the evolution of the causal links with time and varying temperature/soil humidity conditions. In particular, we focus on the causal relationships between Water Surplus/Deficit (WSD), 2m air temperature (T2m), and atmospheric precursors (i.e., Z500 - geopotential height at 500 hPa height). We find that global warming can exacerbate hot and dry extreme conditions by linearly increasing the strength of the causal drivers, as well as impact the strength of causal links in a nonlinear manner.

6.2 Methods

6.2.1 Data and spatial domain

In this study, we focus on hot and dry extremes located in central Europe, defined as the continental region between $45°N - 55°N$, $3°E - 18°E$ (see Fig. 6.1). We analyze daily data from the ERA5 reanalysis dataset (Hersbach et al., 2023b) with a spatial resolution of 1°x1° for summer (June, July, August, JJA) during the 1979-2020 period, including 2m temperature (T2m), 500-hPa geopotential height (Z500), precipitation (Pr), potential evapotranspiration (PET) and sea surface temperature (SST). All mentioned fields are detrended and anomalies are calculated at pentads (5-day averages) time steps, thus removing the climatological cycles.

T2m is selected as a local variable to assess hot conditions, while the Water Surplus/Deficit (WSD) as a local indicator of wet/dry conditions. The WSD is expressed in millimeters per day (mm d^{-1}) and defined as the difference between cumulated precipitation (Pr) and potential evapotranspiration (PET) for a given location i and period t (Li et al., 2021):

$$\mathrm{WSD}(i,t) = \mathrm{Pr}(i,t) - \mathrm{PET}(i,t). \tag{6.1}$$

6.2.2 Standardized Compound Hot and Dry Index

To analyse hot and dry compound extremes, we consider the Standardized Compound Hot and Dry Index (SCHDI). The SCHDI is calculated following Li et al. (2021) using T2m and WSD as variables:

$$\mathrm{SCHDI}_i = \Phi^{-1}\left(F\left(\mathbb{P}\left(\mathrm{T2m} \geq \mathrm{T2m}_i, \mathrm{WSD} \leq \mathrm{WSD}_i\right)\right)\right), \tag{6.2}$$

where Φ^{-1} is the inverse of the standard normal distribution and F is the marginal cumulative distribution of the variable $T = \mathbb{P}\left(\mathrm{T2m} \geq \mathrm{T2m}_i, \mathrm{WSD} \leq \mathrm{WSD}_i\right)$, i.e., $F = \mathbb{P}(T \leq t)$, to remap the joint probability $\mathbb{P}$ into the uniform distribution in $[0,1]$. $\mathrm{T2m}_i$ and WSD_i are T2m and WSD on timestamp i.

We evaluate the association between T2m and WSD using Kendall's τ, checking its statistical significance. Then, we used BiCopSelect, an R function to select the optimal copula function based on the Akaike Information Criterion (AIC), which allows us to calculate the joint cumulative distribution of T2m and WSD. The BiCopSelect function includes 37 potential bivariate copulas, including Gaussian, Student-t copula, Clayton, Gumbel, Frank, Joe, BB1, BB6, BB7, BB8 copulas, as well as the rotated versions of Clayon, Joe, Gumbel, BB1, BB6, BB7, BB8 copulas. Among these families, the Gaussian copula (with $par = -0.68$) is the best fit for our data, which is further validated by the Cramér–von Mises (CvM) goodness of fit (GOF) test. We obtain $CvM_{p-value} = 0.89$

and $CvM_{statistic} = 0.06$. This supports our choice of Gaussian copula to calculate the SCHDI.

Next, we calculate empirically the distribution F (which corresponds to the Kendall distribution function when the variable considered is $\mathbb{P}(\mathrm{T2m} \leq \mathrm{T2m}_i, \mathrm{WSD} \leq \mathrm{WSD}_i))$ to ensure that the joint cumulative distribution is uniformly distributed within the range [0, 1] (Bateni et al., 2017; Salvadori et al., 2007). Finally, we calculate the inverse of the standard normal distribution to obtain the SCHDI.

6.2.3 Definition of extremes and the impact of atmospheric precursors

We define a hot extreme as an event occurring at time t when

$$\mathrm{T2m}(t) \geq \mathrm{T2m}_{95\mathrm{th}}, \tag{6.3}$$

where $\mathrm{T2m}_{95\mathrm{th}}$ is the 95th percentile of T2m anomaly. A dry extreme occurs whenever

$$\mathrm{WSD}(t) \leq \mathrm{WSD}_{5\mathrm{th}}, \tag{6.4}$$

with $\mathrm{WSD}_{5\mathrm{th}}$ the 5th percentile of WSD anomaly. A compound event is detected at t if both conditions defined by Equations 6.3 and 6.4 hold.

Based on the previous definitions, we build Z500 composite fields for T2m, WSD and compound extremes at different lags (see Fig. 6.2). Focusing on a region corresponding to three ridge-trough pairs, we construct precursors time series by computing the linear correlation between the composite field at lag -1 and the Z500 field at each time step. This is done for each of the three composites, obtaining the Z500 precursor time series for T2m extremes $Z500_{\mathrm{T}}$, WSD extremes $Z500_{\mathrm{W}}$ and compound extremes $Z500_{\mathrm{c}}$.

To analyze the influence of atmospheric precursors on the occurrence of weather extremes, the marginal distributions of T2m, WSD, and SCHDI are calculated for both the entire JJA period and for time steps where the atmospheric precursor is amplified, i.e., $Z500_{\mathrm{T}} > Z500_{\mathrm{T,90th}}$, $Z500_{\mathrm{W}} > Z500_{\mathrm{W,90th}}$, and $Z500_{\mathrm{c}} > Z500_{\mathrm{c,90th}}$ (see Figure 6.3).

6.2.4 PCMCI causal discovery algorithm

The Peter and Clark momentary conditional independence (PCMCI) algorithm is a two-step causal discovery tool that allows to distinguish between causal and spurious dependencies among a set of time series, here defined as actors (Runge et al., 2014, 2019). PCMCI considers a time lag among actors, thus detecting the causal influence of one actor on others at a later point in time.

PCMCI relies on several assumptions (see Section 3.2), such as (i) causal sufficiency, (ii) causal stationarity, (iii) the absence of instantaneous causal effects from one variable to another, (iv) the causal Markov condition and faithfulness (Runge, 2018).

The algorithm is described in details in Section 3.4. We perform it by using partial correlation, assuming near-linear interactions between actors at least in a first-order approximation. We focus on lags -1, -2, and -3, covering a period of up to 15 days and show the significant causal links ($p<0.05$).

The significance of the causal link is based on the p-values of the MCI test. To take into account multiple significance testing, the Benjamini-Hochberg false discovery rate (FDR) approach (Benjamini and Hochberg, 1995; Benjamini and Yekutieli, 2001) is used to correct the p-values. To perform PCMCI the Python package Tigramite version 5.0 is used (`https://github.com/jakobrunge/tigramite`).

The analysis results in a causal Effect Network (CEN, see Section 3.3), an object composed of nodes representing each actor, and links, directed from the parent to the actor, weighted by the strength of the causal interaction and specific to the lag τ at which the interaction occurs. The weight of the causal link $X_j^{t-\tau} \rightarrow X_i^t$, i.e. the causal link strength, which we call β value, represents the expected change in X_i in s.d. units at time t when X_j gets perturbed at time $t - \tau$ by one s.d. (Runge et al., 2015).

6.2.5 Statistical hindcast model based on causal precursors

We use the set of identified causal parents to build hindcast models of T2m and WSD by applying multivariate linear regression. Next, we calculate the Area Under the Curve (AUC) score to test the performance of the hindcast models.

The AUC score is an index derived from the receiver operating characteristic (ROC) curve, a graphical representation to illustrate the performance of a binary classifier model across various threshold values (Wilks, 2011). For different threshold settings on a predefined set of observed events, true and false positive rates (i.e., the number of correctly and wrongly predicted events, respectively) are computed from the predicted time series and used to build the ROC curve. The AUC is a commonly used metric to evaluate model predictions in climate science (Di Capua et al., 2019). An AUC = 1.0 indicates perfect predictive skill, while an AUC ≤ 0.5 means no skill.

To avoid over-fitting, we use a fivefold cross-validation test. Fivefold cross-validation means that the dataset is split into 5 equal-sized (or as close to equal as possible) subsets. The hindcast model is trained on 4 of these subsets (training set) but only validated with the remaining one (testing set), based on the AUC score. In this way, every individual data is incorporated into 4 various training sets and used once as the validation set, which ensures our evaluation accurately reflects the model's performance on previously unseen data.

6.2.6 Bootstrapping and significance

To analyze the sensitivity of the strength of the β values to the occurrence of hot, dry, and compound extremes in CEU, we construct multiple CENs for different time windows, going from periods characterized by more intense events to less intense ones. The length of the time window is set to 10 JJA seasons, in order to have enough data for statistical representativeness of the resulting running time series. Thus, consecutive groups of 10 summer seasons (i.e., 33 intervals in the 42 years 1979 to 2020) are unambiguously ranked according to the three extreme scenarios, via the 90th percentile of T2m, the 10th percentile of WSD and the 90th percentile of the SCHDI. This way, we can construct 33 different CENs for each of the three scenarios and, subsequently, assess for each link the β value change going from more extreme to less extreme time periods. The significance of the computed links strength is evaluated by calculating 1000 surrogates of β value obtained by randomly sub-selecting 10 JJA seasons out of the 42 considered years and checking if the obtained value lies outside the 90% confidence interval (two-sided test).

Considering that the time series obtained by the 10 JJA seasons moving window are not independent of one from the other, the significance test should be based on the shuffle of independent blocks of 10 seasons (Di Capua and Coumou, 2016). However, this shuffling would only result in approximately 4 sets of surrogate series, which is insufficient to perform the significance test. Therefore, we also use blocks of 7 and 5 seasons to perform the shuffle, producing 1000 surrogates.

6.3 Results

6.3.1 Atmospheric circulation patterns of hot and dry extremes

In Figs. 6.1a-b we show T2m and WSD anomalies in August 2003 over central Europe (CEU), where we observe a T2m positive anomaly of 3.2 K and a WSD negative anomaly of -2.3 mm per day. During the 1979-2020 period, the frequency of hot extremes ($T2m > T2m_{95th}$) has significantly increased in CEU at the rate of 0.5 events per decade, while their magnitude, i.e. the seasonal-mean T2m anomaly of hot extremes, shows a non-significant slight increase (0.002 K per decade, Fig. 6.1c and d). As for dry extremes ($WSD < WSD_{5th}$, Fig. 6.1e and f), the magnitude, i.e. the absolute seasonal-mean WSD anomaly of dry extremes, has significantly intensified at the rate of $|-0.2|$ mm per day per decade, while the frequency also increased (0.17 events per decade), non-significantly.

Anomalous atmospheric circulation has been suggested as a potential driver of hot or dry extremes. Fig. 6.2 shows composites of 500-hPa geopotential height (Z500) anomalies in the Northern Hemisphere from two pentads before to after single hot (Fig. 6.2a), single dry (Fig. 6.2b), and compound extremes ($T2m > T2m_{95th}$ and $WSD < WSD_{5th}$, Fig. 6.2c) in the CEU region. When comparing the composites shown in Figs. 6.2a-c, a consistent pattern emerges, i.e., a high-pressure system over central Europe together with a low-pressure system in the North Atlantic. However, while during hot extremes the wave shows to propagate eastward,covering the eastern North Pacific, North America, the North Atlantic, central Europe, and central Siberia (lag -1 to lag 1, Fig. 6.2a), during dry extremes the high-pressure system over central Europe persists up to lag 1 (Fig. 6.2b). During compound extremes, both the wave propagation and the persistent high pressure over CEU are observed (Fig. 6.2c). To analyze the atmospheric precursors of single and compound hot and dry extremes, we construct three time series, namely the $Z500_T$, $Z500_W$, and $Z500_c$ indices. These are one-dimensional time series which represent the linear correlation at each pentad time step between the respective composite field at lag -1 (i.e. 5 days prior to the extremes) and the Z500 field over the blue rectangle ($30°N - 60°N$, $170°W - 30°E$) shown in Fig. 6.2. The choice of the representative area of the atmospheric precursors is based on their hindcast ability on T2m and WSD (see Appendix B for further details, Figs. B.1-B.2 and Section B.1). The atmospheric precursors are evaluated only at lag -1 because in this case the composite signals are both intense and significant, especially over CEU, which is not true in the case of lag -2 (see

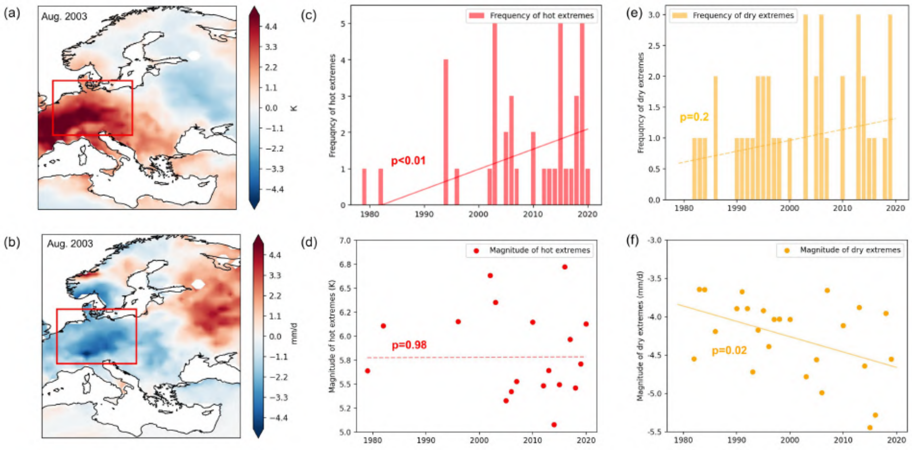

Figure 6.1: **Study region and trends of hot and dry extremes in central Europe. a)** T2m and **b)** WSD anomalies in August 2003 over CEU, marked by the red rectangle. **c-f)** Interannual variations in frequency (**c, e**) and magnitude (**d, f**) of hot (T2m > $T2m_{95th}$) (**c, d**) and dry (WSD < WSD_{5th}) (**e, f**) extremes in CEU. In **c-f**), magnitude is the seasonal-mean T2m (WSD) anomaly of the hot (dry) extremes; solid lines represent a significant linear regression with p <0.05, while dashed lines are non-significant linear regression.

Fig. 6.2).

Next, we investigate the correlation (via the Pearson coefficient and conditional probability) between the atmospheric precursors identified in Fig. 6.2 and the occurrence of hot and dry extremes (Fig. 6.3). Summer T2m and WSD in central Europe show a negative correlation of -0.68 (p <0.01, 6.3a). The co-occurrence of low WSD and high T2m leads to compound hot and dry extremes, which is quantified by the Standardized Compound Hot and Dry Index. The theoretical marginal distributions (normal distributions) reveal that the frequency of hot extremes increases from 5% (by definition) to 28% when only pentads with $Z500_T$ anomalies higher than the 95th percentile are considered. Similarly, during pentads characterized by $Z500_W$ >$Z500_{W,95th}$, the frequency of dry extremes increase from 5% to 23% (Fig. 6.3a). Consistently, a positive correlation is evident between $Z500_c$ and SCHDI (Fig. 6.3b), with a linear regression slope of 0.64 (p <0.01). The frequency of compound hot and dry extremes increases from 5% to 34% when $Z500_c$ > $Z500_{c,95th}$. This is consistent with the atmospheric circulation coupling (Lesk et al., 2021) driving the compound hot and dry extremes, i.e., a high pressure accompanied by less cloud and subsidence, which results in enhanced solar radiation and decreased precipitation (Tian et al., 2023).

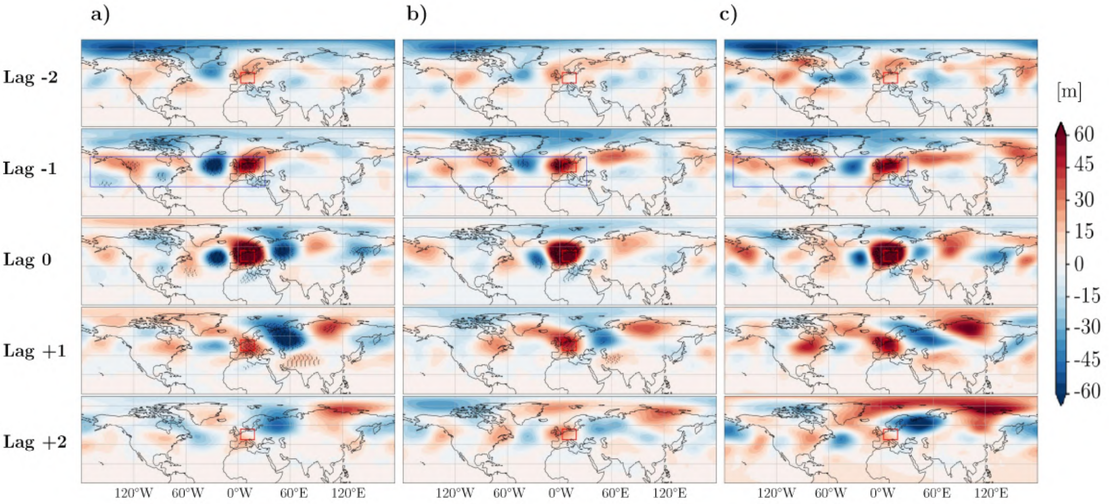

Figure 6.2: **Anomalous atmospheric circulation before and after single and compound hot and dry extremes in central Europe.** Composites of Z500 fields for **a)** single hot extremes (T2m > $T2m_{95th}$), **b)** single dry extremes (WSD < WSD_{5th}), and **c)** compound hot and dry extremes (T2m > $T2m_{95th}$ and WSD < WSD_{5th}) in central Europe (CEU). The composites are computed from 2 pentads before to 2 pentads after the extremes (from the top row to the bottom row). The red box represents the CEU region, while the blue box is the precursor region used to evaluate the atmospheric conditions influencing CEU. Black dots are drawn if the Z500 anomaly is significant at $\alpha = 0.05$.

6.3.2 Causal Effect Networks and hindcast models

To investigate the causal pathways linking T2m and WSD with their atmospheric precursors and surface drivers, we calculate the Causal Effect Networks (CENs) for single and compound hot and dry extremes (Fig. 6.4). When investigating single extremes, both $Z500_T$ and $Z500_W$ are used (Fig. 6.4a), while for compound extremes only $Z500_c$ is considered (Fig. 6.4b). We consider lags of -1, -2, and -3, which align with the typical occurrence of the precursor of hot/dry events, and we only show the significant causal links in the following analysis (p <0.05). In the single extreme CEN (Fig. 6.4a), T2m has two significant causal parents at lag -1, $Z500_T$ ($Z500_T \rightarrow T2m$, β =0.35, i.e., if $Z500_T$ increases by 1 standard deviation (s.d.) at lag -1, T2m will increase by 0.35 s.d. at lag 0) and WSD (WSD→T2m, β =-0.18). These two causal links can be interpreted respectively as (i) $Z500_T \rightarrow T2m$: decreased cloud cover, which leads to increased solar radiation reaching the surface (Tian et al., 2023) and (ii) WSD→T2m: increased sensible heat flux due to suppressed evapotranspiration by limited soil moisture (Seneviratne et al., 2010).

WSD shows three significant causal parents at lag -1: $Z500_{WSD}$ ($Z500_W \rightarrow WSD$, β =-0.39), T2m (T2m→WSD, β =0.17), and WSD itself (WSD→WSD, β =0.16).

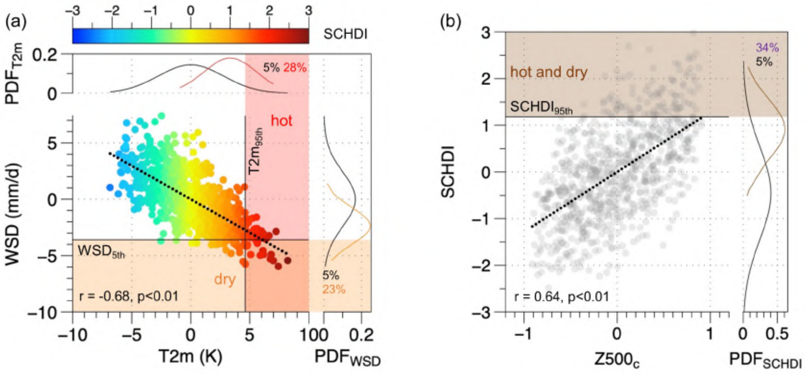

Figure 6.3: **Distribution of T2m, WSD and SCHDI, and their correlations to the atmospheric drivers.** Scatter plots of **a)** T2m and WSD anomalies and **b)** Z500$_c$ anomalies and SCHDI. The dotted lines represent linear regressions of the respective samples. Marginal PDFs are derived for the entire summer (black solid curves), for T2m events when $Z500_T > Z500_{T,95th}$ (red solid curve), for WSD events when $Z500_W > Z500_{W,95th}$ (orange solid curve) and for SCHDI events when $Z500_c > Z500_{c,95th}$ (brown solid curve). The percentages quantify the frequency of T2m, WSD, and compound extremes for the whole summer (in black) and when $Z500_T > Z500_{T,95th}$ for T2m extremes (in red), when $Z500_W > Z500_{W,95th}$ for WSD extremes (in orange), and when $Z500_c > Z500_{c,95th}$ for compound events (in brown).

Z500$_W$→WSD is associated with high pressure and air subsidence, and therefore decreased precipitation (Bárdossy and Caspary, 1990). T2m→WSD can be interpreted as a positive relationship between air temperature and moisture, according to the Clausius-Clapeyron scaling (Drobinski et al., 2018). WSD→WSD indicates the soil moisture memory (Orth and Seneviratne, 2012). Notably, although Z500$_W$ and Z500$_T$ share a linear temporal correlation coefficient of 0.73 (see Table B.1 in Appendix B), distinct links from Z500$_T$ to T2m and from Z500$_W$ to WSD emphasize the necessity of considering these two atmospheric precursors separately.

Compared with single extremes, compound hot and dry events are characterized by two mechanisms, including the atmospheric coupling and the land-atmosphere interaction (Lesk et al., 2021). It is therefore critical to derive the CEN for compound extremes by taking into account Z500$_c$ instead of both Z500$_T$ and Z500$_W$. The peculiar feature of the compound CEN is that Z500$_c$ is identified as the causal parent of both T2m (Z500$_c$→T2m, β =0.36) and WSD (Z500$_c$→WSD, β =-0.34), as shown in Fig. 6.4b. This is motivated by the atmospheric coupling (Lesk et al., 2021) which simultaneously leads to high solar radiation and low precipitation, and thus causes the co-occurrence of hot and dry extremes. The other links maintain the same directions as in the single extreme CEN, though with minor variations in the strength of the β values, including WSD→T2m (β =-0.17), T2m→WSD (β =0.27), and WSD→WSD (β =0.22).

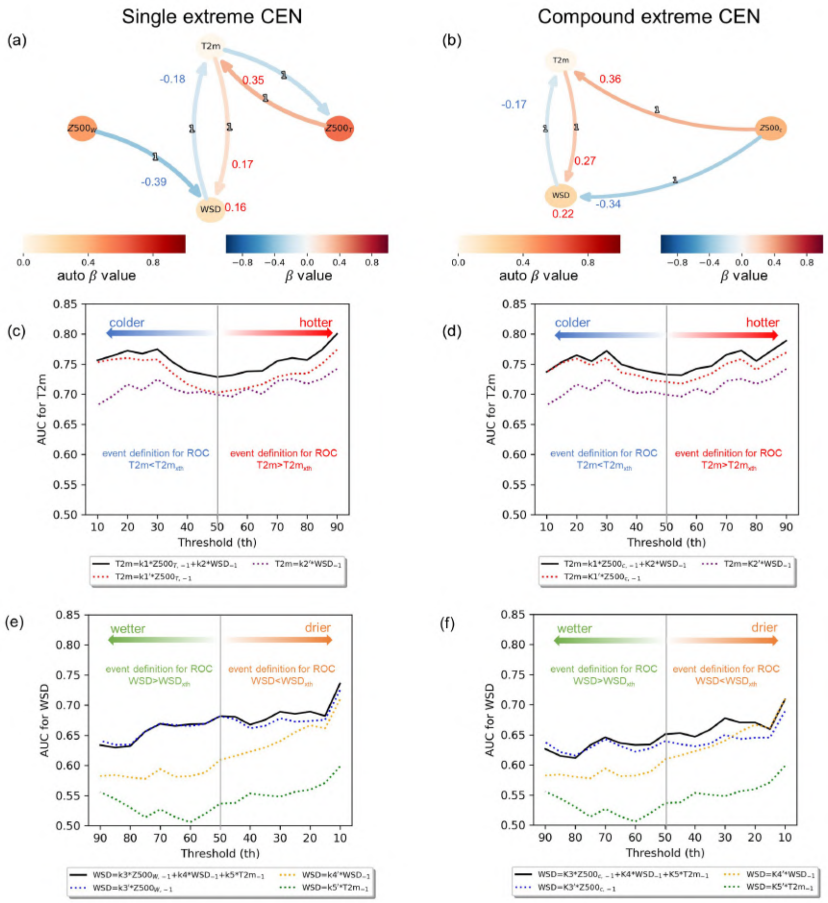

Figure 6.4: **Single and compound extreme CENs and AUC scores of hindcast models**. Left and right panels refer to single and compound extremes, respectively. **a, b)** CENs with significant links; AUC scores for hindcasts of **c, d)** T2m and **e, f)** WSD based on the drivers identified in the single extreme CEN **(c, e)** and based on the drivers identified in the compound CEN **(d, f)**. In **c-f)**, when threshold<50th, the event to compute the AUC score is defined as $WSD<WSD_{threshold}$ and $T2m<T2m_{threshold}$; when threshold≥50th, the event to compute the AUC score is defined as $WSD>WSD_{threshold}$ and $T2m>T2m_{threshold}$. Solid lines represent the hindcast models based on all possible drivers, dotted lines represent the hindcast models based on single drivers. Note that the x-axis ranges from colder to hotter state in Panels (c and d) and from wetter to drier state in Panels (e and f).

Based on the drivers identified in the single extremes CEN (Fig. 6.4a), we hindcast the variations of T2m and WSD using a multivariate linear regression model. To assess the performance of models with different combinations of identified causal drivers we use the area under the receiver operating characteristic curve (AUC) score, as shown in Figs. 6.4c-f. The hindcast model generally exhibits a higher AUC for hot and dry extremes compared to moderate conditions.

From the performance of the hindcast models, we notice that T2m variations are better predicted by $\mathrm{Z500_T}$ than by WSD if a single driver is considered (see dotted lines in Fig. 6.4c). Indeed, the AUC score of the single-driver hindcast model ranges from 0.70 to 0.77 with $\mathrm{Z500_T}$ and from 0.68 to 0.74 with WSD. However, the best hindcast is achieved when both $\mathrm{Z500_T}$ and WSD are included (black solid line in Fig. 6.4c), with the AUC score ranging between 0.73 and 0.80. As for WSD variability, the AUC score of the single driver hindcast model with $\mathrm{Z500_W}$, WSD, and T2m range from 0.63 to 0.73, from 0.57 to 0.70, and 0.51 to 0.60, respectively. Panels 6.4c and 6.4e imply atmospheric precursors are more dominant for both T2m and WSD variability, and our precursors have a stronger hindcast power for T2m than WSD changes.

T2m and WSD variations are also hindcasted using causal drivers identified in the compound CEN (Fig. 6.4b), with the AUC scores shown in Figs. 6.4d and 6.4f. The results are generally consistent with the ones based on the single extreme CEN, with two major differences: (i) when hindcasting T2m, the difference between the hindcast power of Z500 and WSD is larger in the compound case compared to the single case, especially for the middle quantiles (red and blue dotted lines in Figs. 6.4c-d); (ii) when hindcasting WSD, the hindcast power of WSD is higher than the atmospheric precursor if the dry extreme threshold is lower than the 30th percentile based on the compound extreme CEN (Fig. 6.4f), which is not seen in the single extreme one (Fig. 6.4e).

6.3.3 The interannual trend of causal links

Next, we analyze the historical trends of β values by calculating CENs using a 10-year moving window over the 1979-2020 period (see Fig. 6.5). The results show significant changes in T2m and WSD at the rate of 0.7 K per decade and -0.2 mm per day per decade, respectively, with the warming trend more intense than the drying trend (Fig. 6.5a). Moreover, the SCHDI has increased at the rate of 0.16 per decade (Fig. 6.5a). However, no significant trend is detected in the atmospheric precursors, nor in the median or in the extreme values (Fig. 6.5b). In contrast, an increasing strength (in absolute value) of some of the causal links (Figs. 6.5c-f) is evident. β values of $\mathrm{Z500_W}\rightarrow$WSD and $\mathrm{Z500_c}\rightarrow$WSD links present a decrease trend of -0.05 per decade (Figs. 6.5d and 6.5f), while the β value of WSD→T2m shows a significant change at the rate of -0.03 per decade (Fig. 6.5e) in the compound CEN. Thus, we estimate the relative changes of the causal link strength for the analyzed period via

$$\frac{\hat{\beta}_{2010-2020} - \hat{\beta}_{1979-1989}}{\hat{\beta}_{1979-1989}}, \tag{6.5}$$

where $\hat{\beta}$ is the value of the causal strength estimated from the regression lines (see Fig. 6.5f). We find that the absolute impact of dry soil on temperature is amplified by

67% for the compound CEN ($\hat{\beta}^{WSD\rightarrow T2m}_{2010-2020} = -0.25$ and $\hat{\beta}^{WSD\rightarrow T2m}_{1979-1989} = -0.15$, see the purple dashed line of Fig. 6.5e), while the absolute influence of atmospheric drivers on soil moisture is intensified by 50% for compound CENs ($\hat{\beta}^{Z500_\mathrm{C}\rightarrow WSD}_{2010-2020} = -0.42$ and $\hat{\beta}^{Z500_\mathrm{C}\rightarrow WSD}_{1979-1989} = -0.28$, see the blue dashed line of Fig. 6.5f) and 36% for single CENs ($\hat{\beta}^{Z500_\mathrm{W}\rightarrow WSD}_{2010-2020} = -0.49$ and $\hat{\beta}^{Z500_\mathrm{W}\rightarrow WSD}_{1979-1989} = -0.36$, see the blue dashed line of Fig. 6.5d). This implies that the overall warmer and drier climate has a stronger impact on the causal links during compound hot and dry extremes than during single extremes.

We further perform three experiments to check how the background states of seasonal temperature and soil moisture content influence the strength of the causal links (Fig. 6.6). We construct CENs using sub-selections of 10 years based on increasing seasonal $\mathrm{T2m}_{90\mathrm{th}}$, decreasing seasonal $\mathrm{WSD}_{10\mathrm{th}}$ and increasing seasonal $\mathrm{SCHDI}_{90\mathrm{th}}$ (see Appendix B, Figs. B.3a-c). A sensitive test shows that our results are robust to changes of the length of the sub-selection window (see Appendix B, Section B.2 and Figs. B.4-B.6). Here, we only focus on those links for which the influence of the background state is significant at $\alpha = 0.05$ and strong enough (absolute value of correlation coefficient between the causal link strength and corresponding climate variables (i.e., T2m, WSD, or SCHDI) >0.7). The historical intensification of $\mathrm{Z500_W}$→WSD link (Fig. 6.5) is related to soil water content decrease (Fig. 6.6d). The historical stronger WSD→T2m link (Fig. 6.5) can be attributed to both the warmer and drier background conditions (Figs. 6.6a,c,e).

While the aforementioned links variations are consistent with the ones detected in the observations, these experiments show that another causal link, namely WSD→WSD, could undergo a potentially significant variation with higher temperature and lower soil moisture (Figs. 6.6b,d,f). In the single extreme CEN, the WSD→WSD link exhibits a positive correlation with $\mathrm{T2m}_{90\mathrm{th}}$ (linear regression coefficient equal to 0.10 per K) and a negative one with $\mathrm{WSD}_{10\mathrm{th}}$ (linear regression coefficient equal to -0.071 per mm day^{-1}). In the compound CEN, the WSD→WSD link is amplified with increasing seasonal $\mathrm{SCHDI}_{90\mathrm{th}}$ (unitless) at the rate of 0.342 per 1 unit of seasonal $\mathrm{SCHDI}_{90\mathrm{th}}$ (Fig. 6.6f). The two changes in WSD→T2m and WSD→WSD suggest that WSD as a causal driver is the most affected by the seasonal background state.

The change in the strength of the causal link is more pronounced in the compound CEN compared to the single extreme one. Although the WSD→T2m link is amplified in both cases, its β value exceeds the 10% significance test confidence bounds (Fig. 6.6e) only in the compound CEN. For high values of the seasonal $\mathrm{SCHDI}_{90\mathrm{th}}$, the WSD→T2m link reaches twice its average value computed from the entire 42 years set (Fig. 6.6e), which is not observed with varying $\mathrm{T2m}_{90\mathrm{th}}$ (Fig. 6.6a) and $\mathrm{WSD}_{10\mathrm{th}}$ (Fig. 6.6b). This further distinguishes the compound extremes case from the single one apart from the atmospheric circulation coupling: T2m and WSD co-vary more strongly when the background state is both warmer and drier.

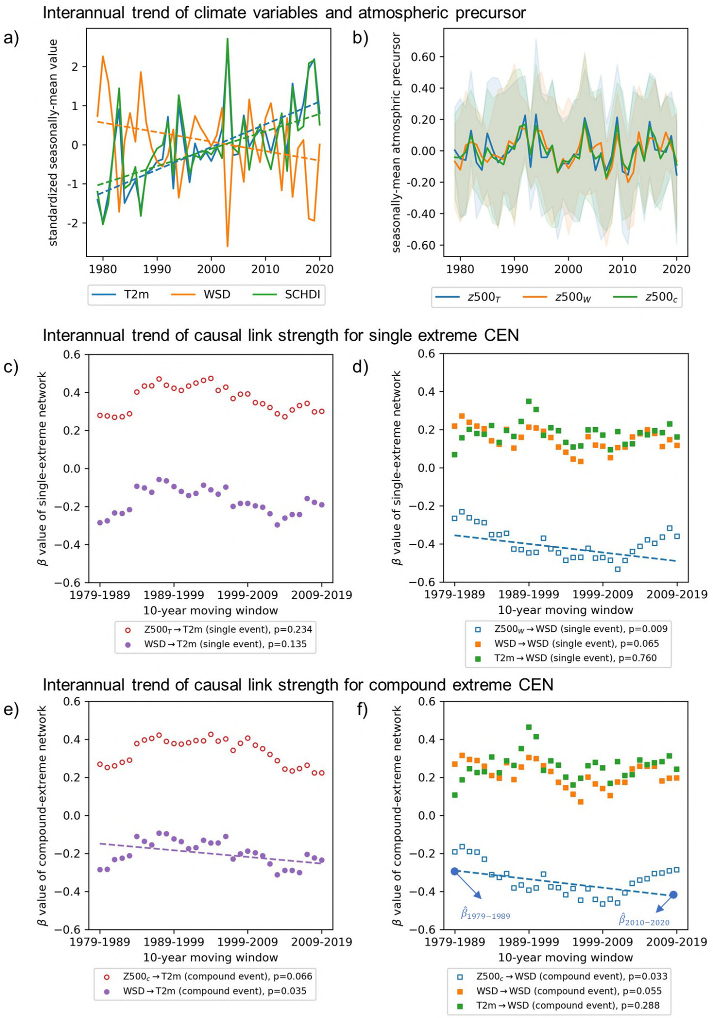

Figure 6.5: **Interannual trends of climate variables, atmospheric drivers and causal links strength.** Interannual trends of **a)** standardized summer seasonal-mean of T2m, WSD, and SCHDI and **b)** atmospheric precursors. **c-f)** Interannual trends of β values **c-d)** for the single extreme CEN and **e-f)** for the compound CEN. Solid lines in **a-b)** represent year-mean values, dashed lines in **a-f)** represent regressions with $p < 0.05$ and shadows in **b)** cover the range from the seasonal 5th to the 95th percentiles. Circles and squares in **c-f)** represent the causal links leading to T2m and WSD variations, respectively, while unfilled and filled scatters represent causal links where atmospheric precursors and land drivers are the causal drivers, respectively.

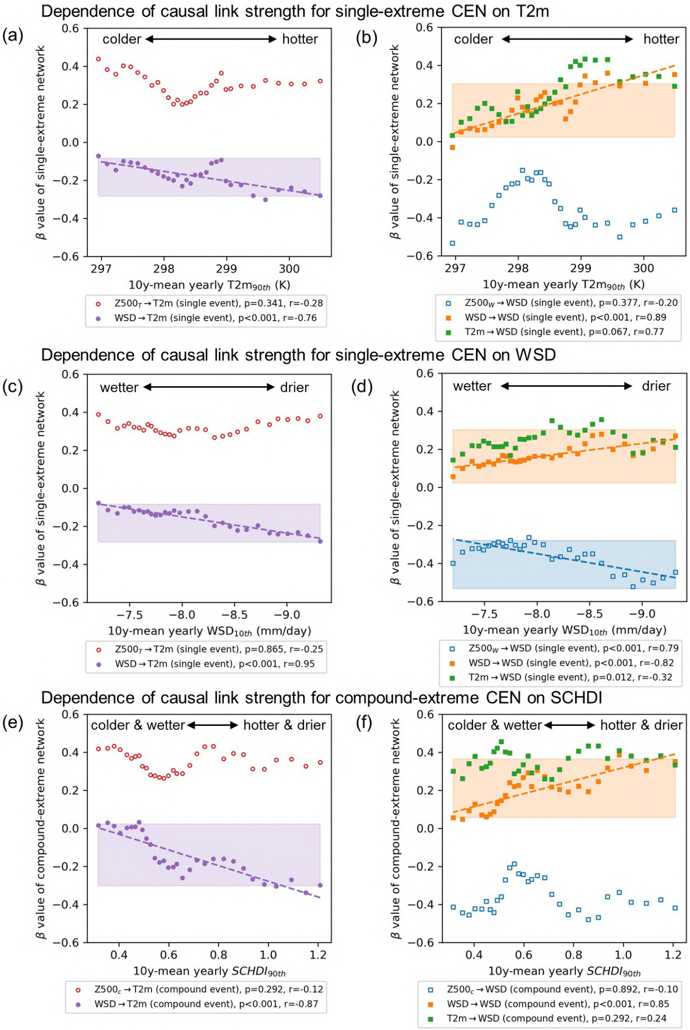

Figure 6.6: **Variation of causal links with T2m and WSD.** Changes of β values in **a-d)** single extreme and **e, f)** compound CENs. Each β value is calculated using a 10 years moving window according to **a, b)** increasing seasonal T2m$_{90\text{th}}$, **c, d)** decreasing seasonal WSD$_{10\text{th}}$, and **e, f)** increasing seasonal SCHDI$_{90\text{th}}$. 10% confidence bounds (shadows) are computed by calculating 1000 surrogates β values from bootstrapped sets of 10 years. The shown linear regressions (dashed lines) are significant at $\alpha = 0.05$ and are characterized by a correlation coefficient between β value and corresponding climate variables (i.e., T2m, WSD, or SCHDI) > 0.7. Circles and squares represent the causal links leading to T2m and WSD, respectively, while unfilled and filled scatters represent causal links where atmospheric precursors and land drivers are the causal drivers, respectively. Notice that the x-axis ranges from colder to hotter state (**a, b**), from wetter to drier state (**c, d**), and from colder/wetter to hotter/drier state (**e, f**).

6.3.4 SST patterns favoring hot and dry conditions in central Europe

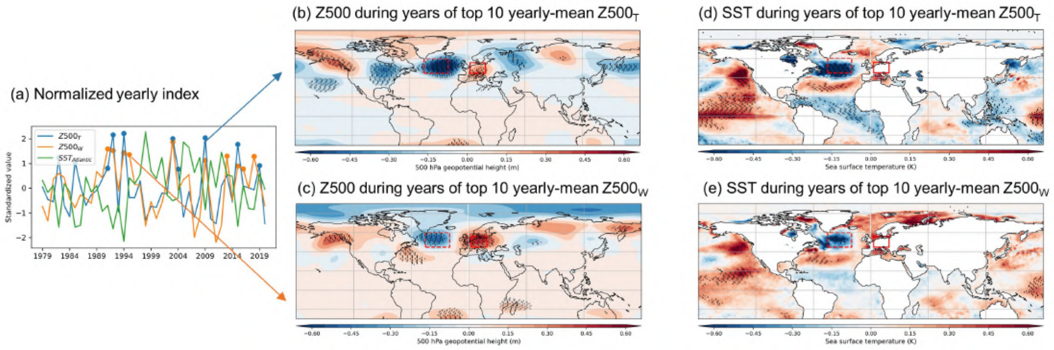

Figure 6.7: **Large-scale atmospheric patterns and sea surface temperature. a)** Standsardized seasonal-mean $Z500_T$, $Z500_W$, and the Atlantic-mean SST anomaly. Dots representing the top 10 years of corresponding time series. The Atlantic region are indicated by the dashed red box in panel (b-e). **b-c)** Z500 anomaly composites during top 10 years of **b)** $Z500_T$ and **c)** $Z500_W$ seasonal mean. **d-e)** SST anomaly composites during top 10 years of **d)** $Z500_T$ and **e)** $Z500_W$ seasonal mean. In panels (b-e), black dots represent grid points where the anomaly is significant at $\alpha = 0.05$, solid red box refers to central Europe, dashed red box refers to Atlantic ocean that is related to CEU hot and dry extremes.

Previous literature has associated the "Atlantic low-Europe high" pattern depicted in Fig. 6.2a (lag-1 and lag 0) with sea surface temperature (SST) anomalies in the North Atlantic (Duchez et al., 2016), which motivates us to investigate the related variations in SST. The composite of SST anomalies for the 10 years with the highest seasonal-mean $Z500_T$ shows a positive anomaly over western North America, central Europe, and central northern Siberia, with negative anomalies over North Pacific, eastern North America, North Atlantic, and eastern Europe (Fig. 6.7d). Furthermore, the low-pressure system over the mid-latitude North Atlantic associated with high $Z500_T$ deepens over Greenland, which resembles a negative phase of the North Atlantic Oscillation (NAO) (Fig. 6.7b). The composite for the highest 10 seasonal $Z500_W$ is similar to the $Z500_T$ pattern, although we notice a more pronounced positive center over central Europe, a high-pressure system to the south of the Atlantic low, and generally negative Z500 anomalies in the Arctic (Fig. 6.7c).

The corresponding SST anomaly in Figs. 6.7d-e reveals both similarities and differences. During years with high seasonal mean $Z500_T$, significant negative SST anomalies can be observed in the mid- and high-latitude North Atlantic, with positive anomalies occurring in the subtropics and negative anomalies over the tropical North Atlantic (Fig. 6.7d). To quantify this relationship, we calculate the yearly summer-mean SST in mid-latitude North Atlantic (45°-20° W, 45°-15° N (Duchez et al., 2016), shown in Fig. 6.7a as $SST_{Atltantic}$). We found that yearly summer-mean $SST_{Atltantic}$ is significantly correlated with $Z500_T$ ($r = -0.63$, $p < 0.01$) and $Z500_W$ ($r = -0.44$, $p < 0.01$). In addition, warm anomalies occur over the North Pacific, from the northeastern part of the North Pacific towards the eastern and central tropical Pacific, while cold anomalies cover the western tropical Pacific. Similarly, during years with high seasonal mean $\mathrm{Z500_W}$, we observe a southward cold-warm-cold SST pattern over the North Atlantic and a warmer eastern Pacific Ocean (Fig. 6.7e). However, cold anomalies over the tropical Atlantic in Fig. 6.7e are not as significant as the ones in Fig. 6.7d.

Furthermore, we investigate the influence of the $SST_{Atlantic}$ on the single and compound extreme CENs by using sub-selections of 10 years based on increasing seasonal-mean $SST_{Atlantic}$. As shown in Appendix B, Fig. B.7, colder Atlantic SSTs have a similar impact on the single extreme CEN (Fig. B.7a and B.7b) as warmer temperatures in central Europe (Fig. 6.6a and 6.6b), especially regarding to WSD→T2m and WSD→WSD. However, Atlantic SSTs do not significantly affect the compound extreme CENs (Figs. B.7c and B.7d).

6.4 Discussion and Conclusion

In this study, we link single and compound hot and dry extremes in central Europe to their large-scale atmospheric precursors and local surface drivers and quantify the causal pathways based on the PCMCI causal algorithm. Our analysis reveals that ten days before hot and dry extreme events, a distinct atmospheric configuration characterized by a high-pressure system over the CEU and a concomitant low-pressure system in the western North Atlantic emerges, which then becomes significant five days before the occurrences of extremes (Fig. 6.2). This atmospheric pattern can be further correlated to a zonal cold-warm-cold SST pattern across the North Atlantic and warmer temperatures in the eastern North Pacific (Fig. 6.7). Notably, when these atmospheric precursors exceed their 95th percentile, the likelihood of single hot, single dry, and compound extremes show a 6-, 5-, and 7-fold increase, respectively (Fig. 6.3).

The CEN analysis shows that the intra-seasonal T2m variability is influenced by both the atmospheric pattern ($\mathrm{Z500_T}$→T2m, AUC≈0.70-0.77) and the WSD (WSD→T2m, AUC≈0.68-0.74). Similarly, the WSD variability is also predominantly governed by its atmospheric precursor ($\mathrm{Z500_W}$→WSD, AUC≈0.63-0.73), while changes in its own dynamics (WSD→WSD, AUC≈0.57-0.70) and temperature anomalies (T2m→WSD, AUC≈0.51-0.60) show a weaker causal effect (Fig. 6.4). Moreover, under warming and drying trends, WSD results as the most affected variable: its causal effect on the other actors increases (WSD→T2m and WSD→WSD), while becoming more sensitive to changes of its causal precursors ($\mathrm{Z500_W}$→WSD, Figs. 6.5 and 6.6).

By building and comparing CENs for the single and compound extremes separately, we show that compound hot and dry events are the result of (i) amplified atmospheric coupling, which is indicated by the causal effect of atmospheric precursor on both T2m and WSD in the compound CEN (Figs. 6.4a, b) and (ii) intensified land-atmosphere interactions, revealed by a stronger and more significant intensification of the WSD→T2m link with high SCHDI than with single extremes indices (Figs. 6.5-6.6). While being in accordance with prior studies (Trenberth and Shea, 2005; Seneviratne et al., 2006;

Berg et al., 2015; Lesk et al., 2021), here we are able to quantify the differences between the causal links in single and compound CENs. During 1979-2020, the strength of the WSD→T2m link is amplified by 67% for compound CEN (Fig. 6.5e), and the strength of $Z500_c$→WSD ($Z500_W$→WSD) increases by 50% (36%) for compound (single) CEN (Figs. 6.5d and f). Moreover, although the warming or drying conditions intensify the land-atmosphere interactions when separately analyzed (Figs. 6.6a,c), the strength of the WSD→T2m link reaches twice its average value under the co-occurrence of hot and dry conditions (Figs. 6.6 e). Thus, our findings help explaining the more pronounced increase of compound extremes (Zscheischler and Seneviratne, 2017).

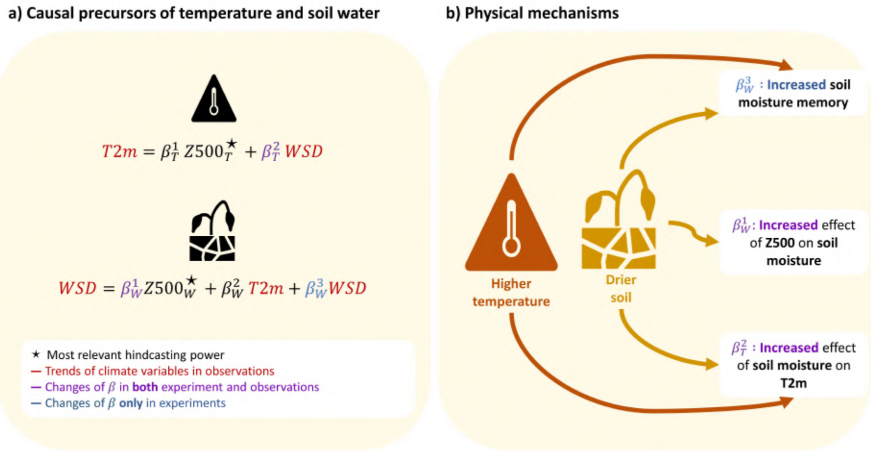

Figure 6.8: **Schematic summary.** **a)** Linear hindcast model of T2m and WSD based on causal drivers and the changes in the Causal Effect Networks. **b)** Physical mechanisms highlighted by our causal analysis.

Previous studies attempted to decompose the warming trend in Europe into its dynamic (Vautard et al., 2023) and thermodynamic components (Suarez-Gutierrez et al., 2020). The dynamic part refers to whether the frequency or intensity of atmospheric circulation is conducive to hot and dry extremes, while the thermodynamic one represents whether the forcing of the atmospheric or surface drivers get strengthened due to warming. To distinguish their relative importance, earlier studies have employed quantile-regression analysis between T2m and circulation features (Emori and Brown, 2005; Vautard et al., 2023) to calculate the dynamic changes and then interpret the residual as thermodynamic changes. However, the quantile regression does not allow a quantitative causal analysis. In our study, we apply CENs to directly assess the thermodynamic forcing by analyzing the changes in the causal links. Our results provide statistical evidence for the key role of the thermodynamic drivers, which is evidenced by the variations in the strength of the causal links (Figs. 6.5-6.6).

Europe has been affected by hot and dry extremes at an enhanced pace compared to other northern mid-latitude regions, with a rise of approximately 0.61 days per decade (Rousi et al., 2022) and a significant increase in flash droughts occurrences by up to 80% (Shah et al., 2022). Our findings are in line with these studies and provide deeper insights into global warming influence on the occurrence of hot and dry extremes. Generally, both T2m variability and WSD changes are more sensitive to their atmospheric precursor (Fig. 6.8a). By analyzing the historical trends (Fig. 6.5), we observe three ways leading to a warmer and drier climate, through (i) the stronger strength of causal drivers, (ii) the enhanced strength of causal links, and (iii) the intensified strength of both causal drivers and causal links (Figs. 6.8a). The latter two scenarios pose an extra risk to the hot and dry extreme effects due to their nonlinear nature. For instance, T2m increases if soil moisture decreases (T2m $\propto \beta_T^2 \times$WSD), and thus the overall drying trend directly affects temperature even considering a constant β_T^2. However, we show that β_T^2 has been intensifying over the last decades as well, from which the nonlinear effect on T2m due to the simultaneous variations of both WSD and β_T^2.

Under warming or drying trend, three causal links are significantly intensified (Fig. 6.8b), including WSD→T2m (β_T^2), Z500$_\mathrm{W}$→WSD (β_W^1), and WSD→WSD (β_W^3). The heightened response of WSD→T2m (β_T^2) under hot and dry conditions is associated with reduced evapotranspiration due to limited soil moisture, leading to increased sensible heat flux (Bartusek et al., 2022). The increasing strength of Z500$_\mathrm{W}$→WSD (β_W^1) causal link can be explained by an enhanced hydrological cycle and an increasing concurrence of soil drought and atmospheric aridity due to land-atmosphere interaction. Once high pressure leads to reduced precipitation, the WSD will quickly respond due to the overall soil moisture shortage (Zhou et al., 2019). The sensitivity of WSD→WSD (β_W^3) to temperature, rarely reported before, can be comprehended within the context of soil moisture-limited regime (Zscheischler et al., 2015). In this scenario, a positive feedback loop initiated by a deficit in soil moisture causes a reduction in evaporation. This consequently causes a temperature increase, leading to a decreased cloud cover and precipitation, ultimately resulting in a further decline in soil moisture.

Global warming will further add to these nonlinear effects, especially for compound events. On the one hand, historical observations already show a stronger increase in the causal pathways of compound CEN compared to the single extreme CEN (β_W^1 and β_T^2, Fig. 6.8b). On the other hand, we show that under a warmer and drier climate soil moisture memory could increase (β_W^3, Fig. 6.8b), and indeed some studies have already reported a continuous warming temperature and drying soil in central Europe and over larger areas (Dai, 2013; Vautard et al., 2014). These spatio-temporal variations in temperature and soil moisture imply further changes in the causal links, especially under different emission scenarios. Further research is needed to quantify the risks based on future climate projections and to assess the Causal Effect Network of hot and dry extremes with other human-related drivers included to disentangle the anthropogenic contribution from the natural variability.

7 Conclusions

The work described in this dissertation focuses on the application of complex systems methodologies to climate science, to gain novel insights into the spatial synchronizations and causal pathways that underlie compound extremes in Europe. We adopt a complex systems framework to unravel the spatio-temporal relationships between these extremes, examining how spatial synchronizations (i.e., the co-occurrence of extremes across different regions) manifest, as well as identifying the causal pathways that link disparate climatic events. Our findings contribute to a deeper understanding of the interconnected nature of climate extremes in Europe, offering insights that may inform climate risk assessments and enhance early warning systems.

In this final Chapter, we provide a comprehensive summary of the main contributions of this dissertation, revisiting the scientific questions that motivated our research and emphasizing the significant results achieved through our applications. Additionally, we explore open questions and potential directions for future research.

7.1 Contributions of this work

Our research falls within the field of climate science, utilizing an interdisciplinary approach that bridges the gap between complex systems science and atmospheric physics. In particular, we apply complex climate networks and causal effect networks to characterize the spatio-temporal features of hot and dry compound events in Europe.

In the first part of this dissertation (Part I) we lay the groundwork by discussing the theoretical foundations of our studies. In Chapter 2 we introduce and describe complex network theory, focusing on spatially embedded climate networks, which are applied in Chapter 4 and 5. In Chapter 3 we revise causal discovery and causal effect networks, with a focus on the Peter and Clark momentary conditional independence algorithm which we apply in Chapter 6.

Is there a coherent structure emerging from extremes synchronizations?

We demonstrate that complex networks are key for identifying the spatio-temporal structures of extreme event synchronizations.

In our first application (Chapter 4), we identify continental networks of meteorological droughts for four different accumulation periods. We observe that the structure of these drought networks is quite similar across the four accumulation periods, with differences primarily related to the presence of long-range connections, which increase as precipitation deficiency timescales extend from short to long. Thus, we conclude that a regional structure underlies the synchronization of droughts in Europe, which remains coherent across different timescales, with small but crucial differences that help explain the spatial characteristics of droughts in relation to their temporal scale. Furthermore, regional communities based on drought propagation are characterized in terms of source-sink systems, unravelling the average spatial patterns of meteorological droughts. This type of analysis would be unfeasible without considering the synchronization structure as a whole, which links structural features to dynamic functioning.

In our second application (Chapter 5), we model European hot and dry compound event synchronizations through evolving networks. This analysis focuses on the temporal evolution of the graph structures in addition to their spatial features. We find that the topology of the resulting networks differs between the summer and winter seasons, with direct connections to the typical atmospheric regimes that characterize each season. Again, we show that climate networks enable the detection of spatial structures consistent with the climate regimes.

Can we detect this structure to enhance our understanding of the occurrence and propagation of these extremes?

The reliability of the identified network structures is directly connected to the methodology applied to construct the graphs from data. It is crucial to minimize the uncertainties related to link attribution in order to link structural properties to physical functioning.

In our first application (Chapter 4), we address this problem by constructing the network based on links that are robust over time, using what we call the Hamming procedure. This procedure introduces a new approach to reduce the uncertainties of link attribution for unweighted and undirected networks reconstruction, when there is no prior knowledge of the system being studied. The Hamming procedure helps us determine the optimal cutoff threshold to select connections that are both significant and temporally robust. This approach allows us to retain the long-lasting backbone structure of the process, while discarding most of the spurious synchronizations caused by internal variability and noise.

In our second application (Chapter 5), the issue of link attribution is addressed using a statistical procedure based on the construction of time series surrogates. We apply block shuffling to the original data and test the significance of synchronization values, while also accounting for multiple significance testing.

In the third application (Chapter 6), we first select those causal relationships which are statistically significant (also accounting for multiple significance testing) and subsequently we use a bootstrapping procedure to test if the strengths of the causal link, i.e. the β values, is significantly different from random samples of the data.

These procedures ensure that the detected structures are reliable for further analysis, allowing us to confidently link topological features to the underlying physical mechanisms.

What are the statistical relationships between local and atmospheric variables that lead to compound events? Have these statistical relationships changed in the recent past with increasing global warming?

In Chapter 5, we qualitatively explore the relationships between spatial synchronizations of hot and dry compound extremes in Europe and atmospheric conditions by comparing the structure of the evolving networks with the geopotential heights composites evolution. The results of this analysis are distinguished between summer and winter season and European regions, each one with its own peculiar features. During summer, we find that the north and the center of the continent are more strongly connected in recent times, with stronger geopotential height anomalies over Europe, suggesting that an increase of the positive phase of SNAO could be associated with these conditions. During winter, the increase of Mediterranean synchronizations appears to be closely related to the positive phase of winter NAO.

In our study on causal effect networks of compound hot and dry extremes in central Europe (Chapter 6), we explore in detail the causal relationships and their trends in the recent past between local variables (temperature and soil water content) and remote atmospheric drivers (geopotential height patterns related to extreme temperature and soil water content conditions). Here, we are able to quantify the mutual interactions and explore the potential evolution of these relationships under hotter and drier future scenarios. We find that the influence of dry soil on temperature has increased by 67% during compound hot and dry extremes, while the impact of atmospheric drivers on soil moisture has intensified by 50% during compound extremes and by 36% during single extremes.

In both these works we explicitly investigate the evolution of the synchronizations and causal relationships related to hot and dry compounds. We demonstrate that evolving networks and causal discovery analysis are well suited to perform this kind of assessment, offering new insights in the intricate statistical relationships involved.

Can we detect and quantify the causal links between the local and atmospheric variables connected to hot and dry extreme events?

Causal discovery, and the application of the PCMCI algorithm, allows to directly quantify the causal relationships between climate variables. We apply this analysis by using linear partial correlation as statistical independence test, but it is possible to use nonlinear metrics as well, as we discuss in Chapter 3. It is also important to keep in mind that the found causal links are strictly related to the analysed variables. Once we identify the set of causal parents for each variables, we use multivariate regression to build statistical hindcast models based on the causal precursors. The multivariate models are used to hindcast the evolution of temperature and soil water content to check how these models behave in mimicking hot and dry conditions, and their performances are measured with the AUC score. This way, we quantify the impact of each and every causal parent to its response variable, and distinguish the model performance based on its hindcast ability for different extreme scenarios. The found relationships can be used to predict the impacts of the identified drivers.

7.2 Challenges and future work

As demonstrated throughout this dissertation, complex networks provide an insightful approach to gain valuable information in the climate field. They are a highly versatile tool, adaptable to studying a wide range of processes using any statistical measures of choice. The strength of complex networks lies in their ability to model processes at various spatial and temporal scales. We believe that this field holds significant potential for further development, both from a methodological perspective—where new and advanced statistical techniques could enhance this approach—and in terms of its diverse applications.

However, several important points must be carefully considered when applying these methodologies. It is crucial to explicitly acknowledge the limitations of these methods to avoid over-interpreting the results. First, climate networks—at least those presented in this thesis—are constructed using statistical metrics that are not designed to capture the true physical behavior of the complex system under study, but rather to measure the functional connectivity among nodes. This is, in fact, the essence of a functional network: the attributed links, even the significant ones, represent a statistical model of the system and are therefore susceptible to erroneous attributions. Furthermore, the uncertainties in the dataset used to construct the network directly influence the network's construction, whether the data is derived from observations or from climate and weather models.

The choice of a specific statistical similarity measure carries the assumptions underlying that metric, which must always be clearly stated. Each metric has its own strengths and limitations, and not all measures provide the same perspective on the process under examination. Additionally, the thresholding of the interaction matrix, which follows the application of the statistical measure to determine relationships between nodes, is another critical step: the method used to filter out non-significant links may introduce biases.

The selection of the variables is also a delicate step, especially in methods based on Granger causality, where the sufficiency of the dataset must be ensured. For spatially embedded networks, this requires a careful choice of the spatial domain considered in the analysis, keeping in mind that the spatial embedding may introduce strong biases on the network indexes patterns. The temporal scale influences the results too and must be chosen based on a solid understanding of the system under study, especially when using causal detection algorithms where the time scale can influence the detection of the causal links.

Another important challenge when representing climate data with networks is the selection of appropriate network measures. Network theory provides a wide range of metrics to characterize different network properties, such as identifying key nodes through centrality measures or detecting coherent structures with clustering measures. Each metric has its own strengths and limitations, and it is essential to use a measure only when there is a clear understanding of its meaning and interpretability. Simply put, there is no benefit in applying a complicated network index if it cannot be translated into concrete, physical terms.

Here we focus on hot and dry extremes in Europe, but, looking ahead, the present study could be further extended to include other regions and processes.

In our first application described in Chapter 4, we focus on meteorological droughts, but the same methodology could be easily expanded to other types of droughts, accounting for multiple variables to model agricultural, hydrologic or even socioeconomic water deficiencies. This would offer a complete picture of this processes in the context of the European continent, where we see a high spatial variability in precipitation and water availability, with contrasts between the north and the south of the continent.

When analysing the evolution of compound extremes, as we have done in our second application on Chapter 5, it would be useful to apply the evolving network approach to climate predictions or projections, to see how the synchronizations of these extremes are going to evolve under future conditions. It could be also interesting to better assess the atmospheric conditions related to these extremes by analysing other variables beyond the geopotential height, so to get a more complete picture of the climate conditions during extremes.

Our application of causal effect networks to hot and dry extremes in central Europe (Chapter 6) could be also expanded to the use of nonlinear statistical independence test, also accounting for different variables that may be important in influencing hot and dry conditions.

Further research is also needed to quantify the risk related to compound extremes, providing policy-relevant results to mitigate or avoid the most dangerous future scenarios.

Earth System dynamics is a vast and rich field, where many unsolved questions still remain. Complex networks prove to be a reliable tool to complement other approaches to gain better insight of the functioning of the climate system at various scales. The intersection of complex theory and climate science should be even more promoted, towards the development of multidisciplinary research, which is key to overcome the limitations and biases of single disciplines just as well as combine their strengths.

7.3 List of publications

1. Giaquinto, D., Marzocchi, W., and Kurths, J.: Exploring meteorological droughts' spatial patterns across Europe through complex network theory, Nonlin. Processes Geophys., 30, 167–181, https://doi.org/10.5194/npg-30-167-2023, 2023.

2. Giaquinto, D., Di Capua, G., Marzocchi, W., and Kurths, J.: Spatio-temporal evolution of compound hot and dry extremes synchronizations in Europe, accepted for publication by Climate Dynamics.

3. Tian*, Y., Giaquinto*, D., Di Capua, G., Claassen, J., Ali, J., Li, H., De Michele, C.: Historical changes in the Causal Effect Networks of compound hot and dry extremes in central Europe, accepted for publication by Communications Earth & Environment.

*These authors contributed equally to this work.

Appendix A

Supplementary Material to Chapter 5

A.1 NAO and SNAO indices computation

The NAO index is based on the difference of normalized daily mean sea level pressure (SLP) between Ponta Delgada, Portugal (37.74°N, -25.68°E) and Reykjavik, Iceland (64.13°N, -21.83°E) (Hurrell, 1995; Jones et al., 1997). We compute it at daily resolution for the study period 1941–2020 and for the DJF season.

First of all, the SLP at station A (Ponta Delgada) and day d, $SLP_{A,d}$, is normalized based on the mean and standard deviation computed from the reference period 1941–1970:

$$SLP'_{A,d} = \frac{SLP_{A,d} - \overline{SLP_{A,d}}}{\sigma_{A,d}} = \frac{SLP_{A,d} - \frac{\sum_{1941}^{1970} SLP_{A,d}}{n}}{\sqrt{\frac{\sum_{1941}^{1970}(SLP_{A,d} - \overline{SLP_{A,d}})^2}{n-1}}}, \tag{A.1}$$

where $SLP'_{A,d}$ is the normalized SLP at at station A and day d, $\overline{SLP_{A,d}}$ and $\sigma_{A,d}$ are the SLP mean and standard deviation at station A and day d during the reference period 1941–1970, and n is the number of days d in the reference period, i.e., 30. Similarly, the normalized SLP at station B (Reykjavik) and day d is also derived. The daily NAO index is then computed by differencing the two normalized series:

$$NAO_d = SLP'_{A,d} - SLP'_{B,d}. \tag{A.2}$$

The monthly NAO index and the DJF one are simply computed by averaging the daily index over the month and the DJF season, respectively.

The NAO index can be also computed using other methodologies, such as empirical orthogonal analysis (EOF) (Folland et al., 2009), which is suited to account for the annual migration of NAO centers of action. However, since we compute the NAO index only for the DJF season, computing the index using fixed locations is enough (Cropper et al., 2015).

The SNAO index is based on the difference of normalized daily mean sea level pressure between two domains: one at coordinates 25°W–5°E, 45–55°N and one at 52–22°W, 60–70°N. These are selected to cover the SNAO centers of action (Dunstone et al., 2023; Wang and Ting, 2022) during summer. It is computed following the same approach described for the NAO but for the JJA season, where $SLP_{A,d}$ is the daily mean sea level pressure averaged over the domain 25°W–5°E, 45–55°N and $SLP_{B,d}$ is the daily mean sea level pressure averaged over the domain 52–22°W, 60–70°N.

A.2 Number of events and synchronicity scenarios

In the context of the present study, it is crucial to distinguish between number of events at location i and location j and number of possible significant synchronizations between events at location i and events at location j. This distinction is indeed the core motivation of this work, as assessing compounds evolution is not the same as assessing compound synchronizations evolution. Even if we expect these two quantities to generally correlate, this is not always true, as we are going to explain in the following.

Let us consider nodes i and j and let us assume that they are both characterized by a relatively high number of events occurrences, say S_i and S_j, w.r.t. the length of the analysed period L. If the events are randomly placed, we expect the number of synchronized events to be relatively high (Figure A.3a-b).

Although this is what we statistically anticipate, the climate system does not operate fully at random, thus it may happen that such event series could be even more synchronous (Figures A.3c-d, e.g., think of two adjacent locations, if a very refined spatial resolution is used) or almost fully anti-correlated in events occurrences (Figures A.3e-f). Thus, a high number of events does not imply high number of synchronizations. The reverse is also true, i.e., a low number of events does not imply low synchronizations, as shown in Figure A.4.

In our specific case, these circumstances do sometimes take place. In JJA, a high number of events in northern Europe results in high average degree centrality (please compare Figures 5.3a and 5.5a), similarly as the case depicted in Figures A.3a-b. Conversely, in DJF we find that Great Britain, northern France, and Germany, have high degree centrality even if few events are detected (please compare Figures 5.3b and 5.5b), similarly as the case depicted in Figures A.4c-d.

Similar reasoning is applied when analysing the events trend and the synchronizations trend, i.e., in the comparison between Figures 5.3c-d and Figures 5.5c-d. During JJA, we find that some locations in Finland, northern Poland, and the Baltic display a significant increasing degree centrality (Figure 5.5c), while the number of compound events is not significantly growing (Figure 5.3c). Conversely, southern Portugal, southern Spain, and Northwest Africa do not display an increasing degree centrality (Figure 5.5c), but are characterized by an increasing number of events (Figure 5.3c).

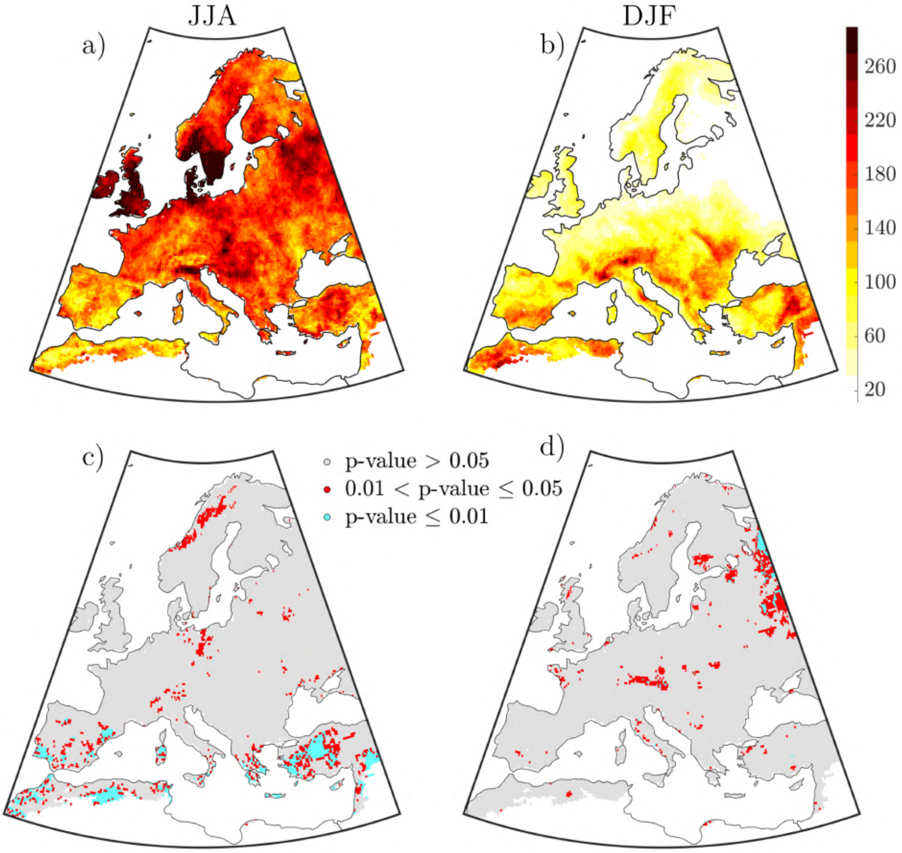

Figure A.1: **Spatial distribution and trend significance of compound events.** Number of compound events during 1941 – 2020 for **a)** the JJA season and **b)** the DJF season. P-values of the detected seasonal trends of compound events for **c)** the JJA season and **d)** the DJF season.

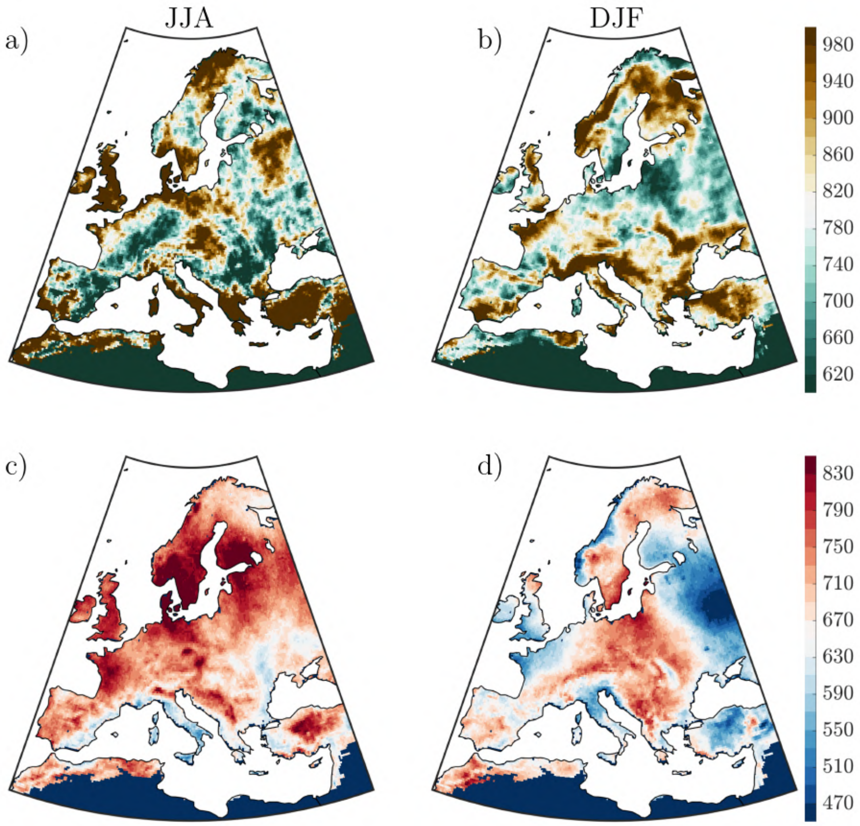

Figure A.2: **Spatial distribution of hot and dry extremes.** Number of dry extremes during 1941 – 2020 for **a)** the JJA season and **b)** the DJF season. Number of hot extremes during 1941 – 2020 for **c)** the JJA season and **d)** the DJF season.

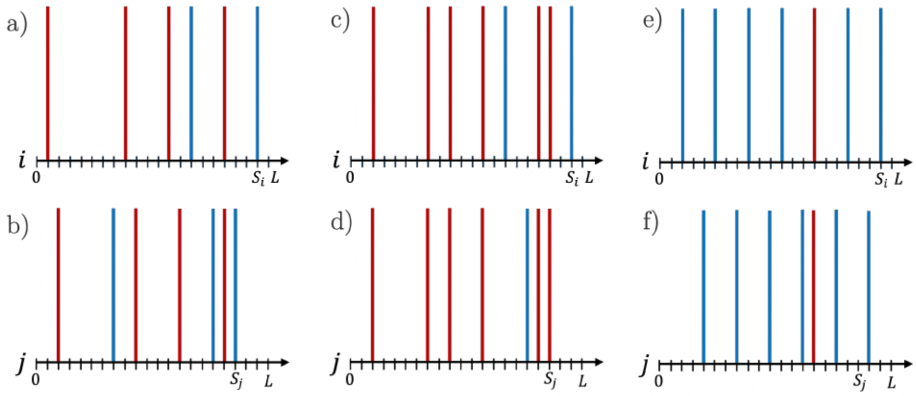

Figure A.3: **Series with high number of events and their synchronizations. a)** Random event series of total length L of location i, with S_i being the total number of events. An event marked in red is synchronized with an event at j, while events marked in blue are not synchronized. **b)** Same as **(a)** but for event series j. **c-d)** Same as panels **(a-b)** but for almost fully synchronized event series. **e-f)** Same as panels **(a-b)** but for almost fully de-synchronized event series.

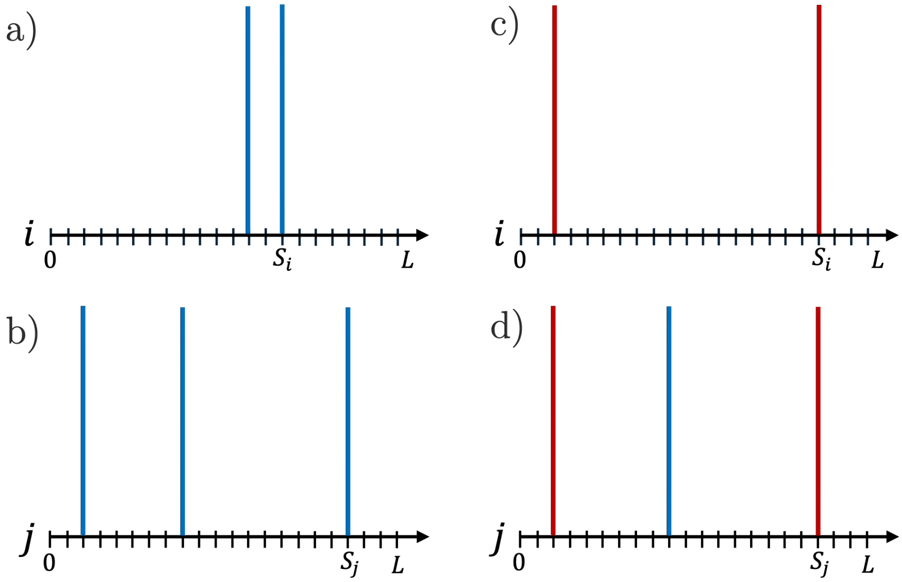

Figure A.4: **Series with low number of events and their synchronizations. a)** Random event series of total length L of location i, with S_i being the total number of events. An event marked in red is synchronized with an event at j, while events marked in blue are not synchronized. **b)** Same as **(a)** but for event series j. **c-d)** Same as panels **(a-b)** but for almost fully synchronized event series.

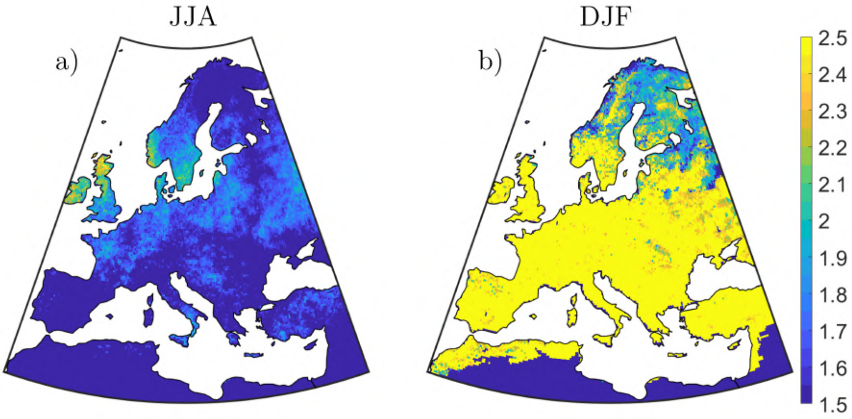

Figure A.5: **Average clustering coefficient.** Average value of clustering coefficient across the 51 network blocks for **a)** the JJA season and **b)** the DJF season. The clustering coefficient is dimensionless because of the correction of bias due to spatial embedding.

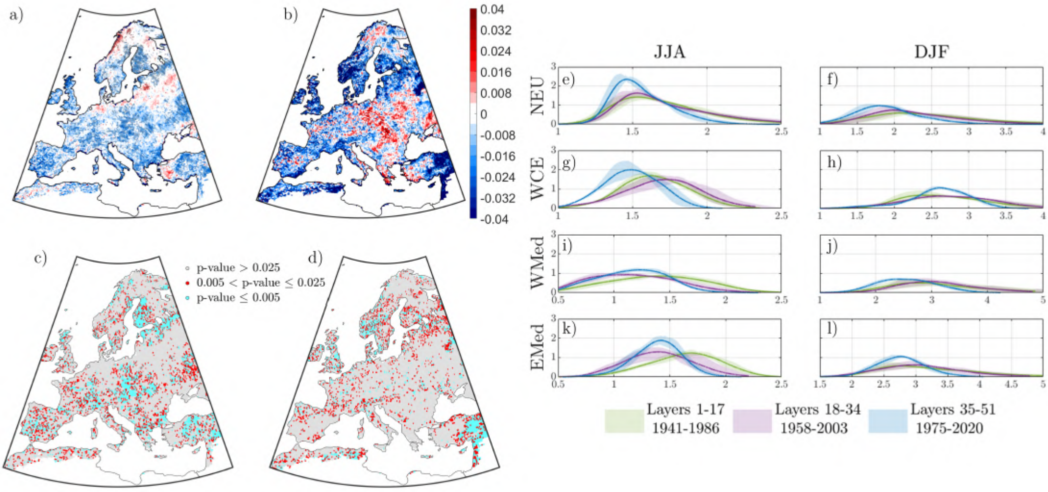

Figure A.6: **Evolution of clustering coefficient.** clustering coefficient trend for **c)** the JJA season and **d)** the DJF season. Dots are drawn if the trend is significant at $\alpha = 0.05$ (two-sided sieve bootstrap t-test). P-values of the detected clustering coefficient trends for **c)** the JJA season and **d)** the DJF season. **e-l)** Pdfs (empirically estimated via Gaussian-Kernel distributions) of the clustering coefficient for JJA and DJF and for every European region. The 51 distributions are divided in 3 groups for which we show the average value (solid lines) and 1 s.t.d. confidence bound (shades). The clustering coefficient is dimensionless because of the correction of bias due to spatial embedding.

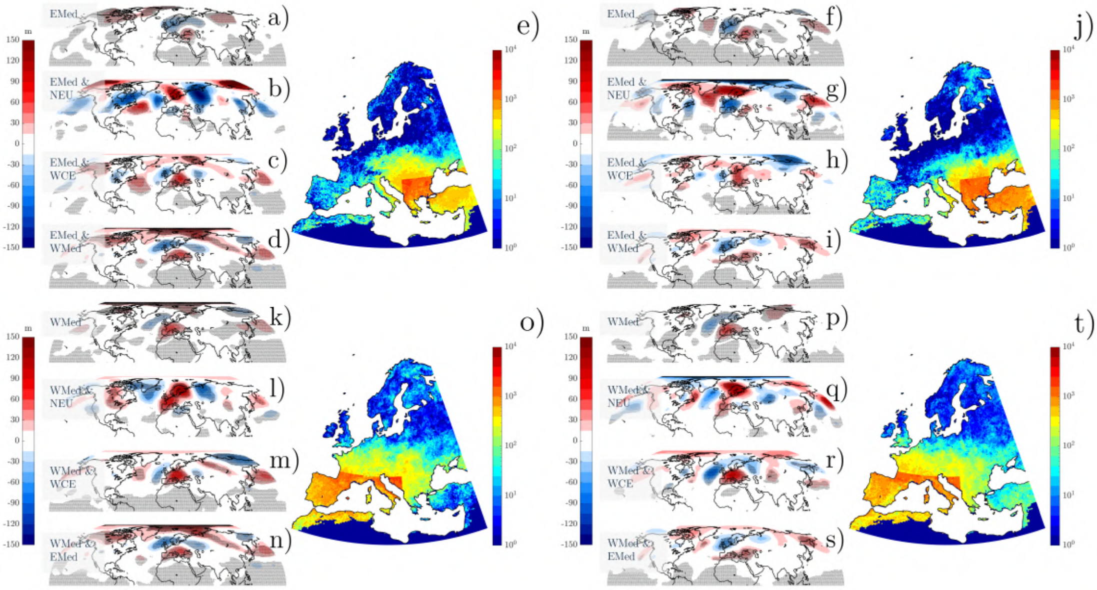

Figure A.7: **Geopotential height composites and links variations during JJA. a-d)** Z500 composites during the top 10% of days for number of compound events occurrences for the indicated regions and for the period 1941-1970. **e)** Number of links directed to EMed found in the 1941-1970 network block for each node. **f-j)** Same as panels (a-e), but considering the last 30 years of the analysed period, i.e. 1991-2020. **k-t)** Same as panels (a-j) but with respect to WMed. For all the composites, black dots are drawn if the Z500 anomaly is significant at $\alpha = 0.05$.

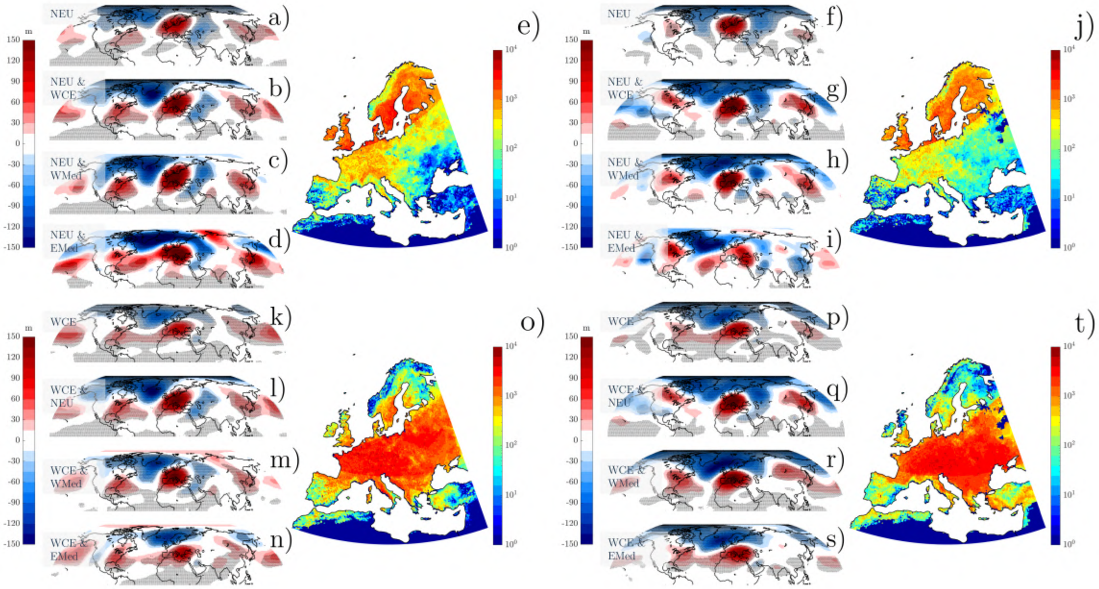

Figure A.8: **Geopotential height composites and links variations during DJF. a-d)** Z500 composites during the top 10% of days for number of compound events occurrences for the indicated regions and for the period 1941-1970. **e)** Number of links directed to NEU found in the 1941-1970 network block for each node. **f-j)** Same as panels (a-e), but considering the last 30 years of the analysed period, i.e. 1991-2020. **k-t)** Same as panels (a-j) but with respect to WCE. For all the composites, black dots are drawn if the Z500 anomaly is significant at $\alpha = 0.05$.

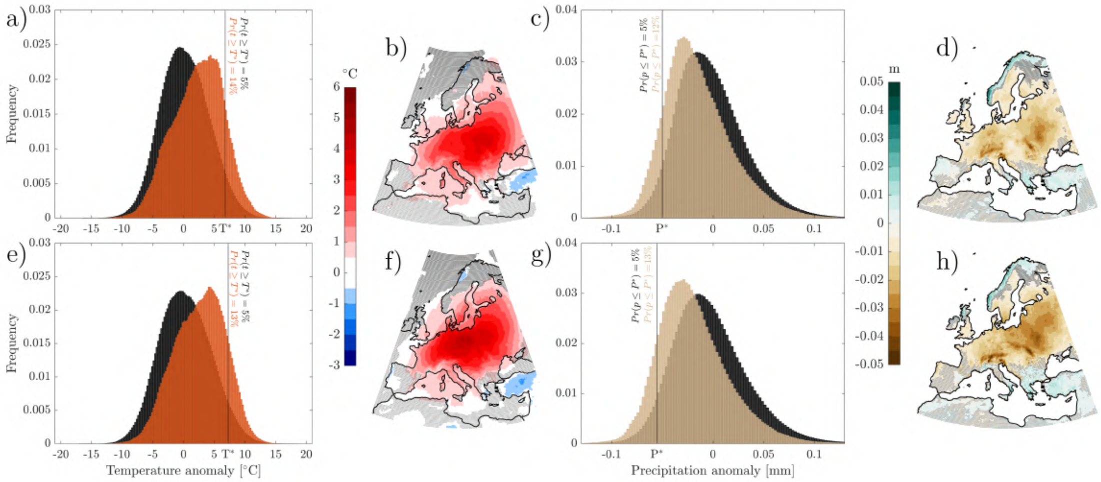

Figure A.9: **Temperature and precipitation anomalies for WCE in JJA. a,c)** Normalized histogram plots of temperature (a) and precipitation (b) for the JJA season in 1941-1970 (black histograms) and for high compound days (temperature in red and precipitation in brown). The black line indicates the 95th (5th) percentile T^* (P^*) of the complete JJA temperature (precipitation) distribution. The probability of exceeding this temperature (precipitation) level during high compound days is shown in red (brown). **b,d)** Temperature (b) and precipitation (d) composites during high compound days. Black dots are drawn if the anomaly is not significant at $\alpha = 0.05$. **e,h)** Same as (a-d) but for 1991-2020.

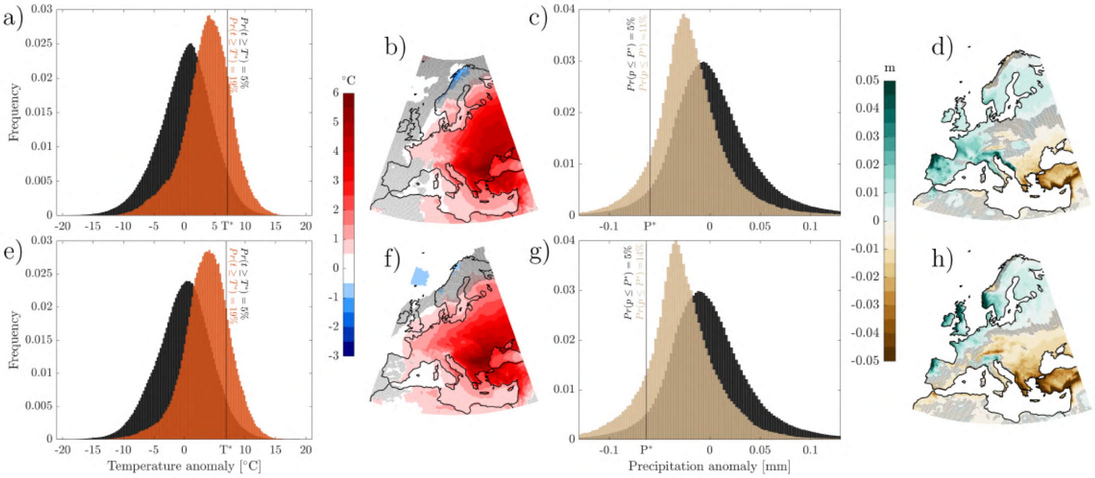

Figure A.10: **Temperature and precipitation anomalies for EMed in DJF. a,c)** Normalized histogram plots of temperature (a) and precipitation (b) for the JJA season in 1941-1970 (black histograms) and for high compound days (temperature in red and precipitation in brown). The black line indicates the 95th (5th) percentile T^* (P^*) of the complete JJA temperature (precipitation) distribution. The probability of exceeding this temperature (precipitation) level during high compound days is shown in red (brown). **b,d)** Temperature (b) and precipitation (d) composites during high compound days. Black dots are drawn if the anomaly is not significant at $\alpha = 0.05$. **e,h)** Same as (a-d) but for 1991-2020.

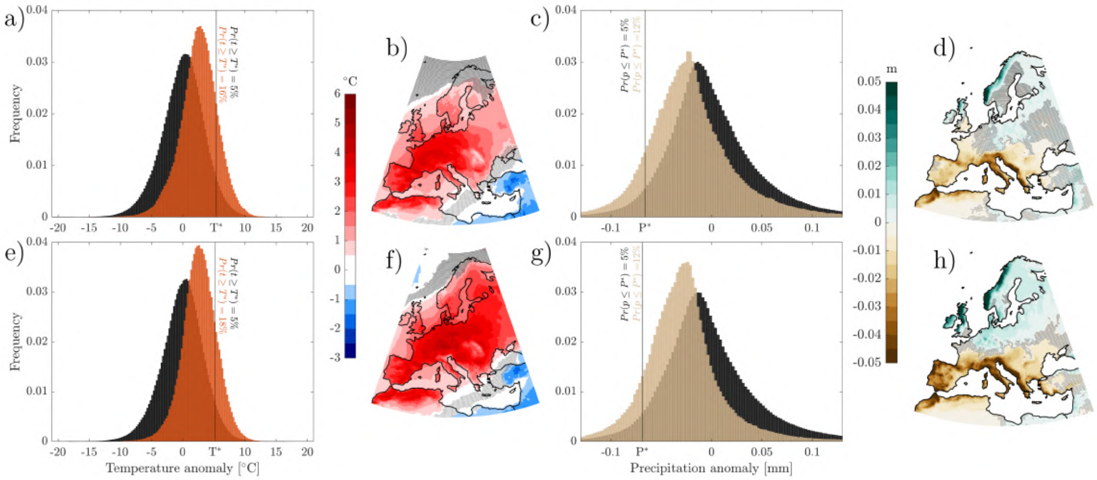

Figure A.11: **Temperature and precipitation anomalies for WMed in DJF. a,c)** Normalized histogram plots of temperature (a) and precipitation (b) for the JJA season in 1941-1970 (black histograms) and for high compound days (temperature in red and precipitation in brown). The black line indicates the 95th (5th) percentile T^* (P^*) of the complete JJA temperature (precipitation) distribution. The probability of exceeding this temperature (precipitation) level during high compound days is shown in red (brown). **b,d)** Temperature (b) and precipitation (d) composites during high compound days. Black dots are drawn if the anomaly is not significant at $\alpha = 0.05$. **e,h)** Same as (a-d) but for 1991-2020.

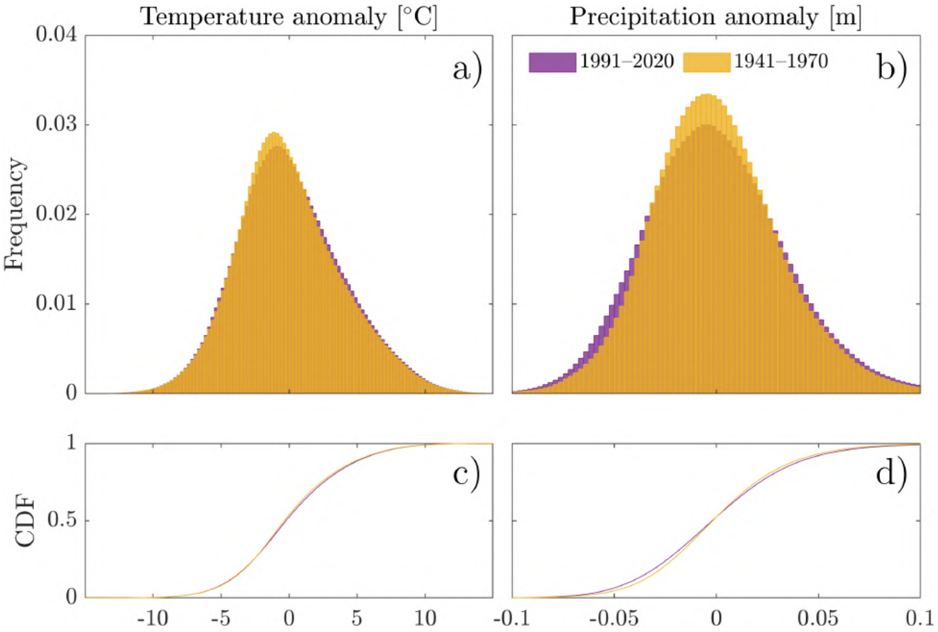

Figure A.12: **JJA Temperature and precipitation distributions for NEU. a)** Normalized histogram plots of temperature and **(b)** precipitation for the JJA season in 1941-1970 (yellow histograms) and in 1991-2020 (violet histograms). **c)** Cumulative distribution function of temperature and **(d)** precipitation for the JJA season in 1941-1970 (yellow line) and in 1991-2020 (violet line).

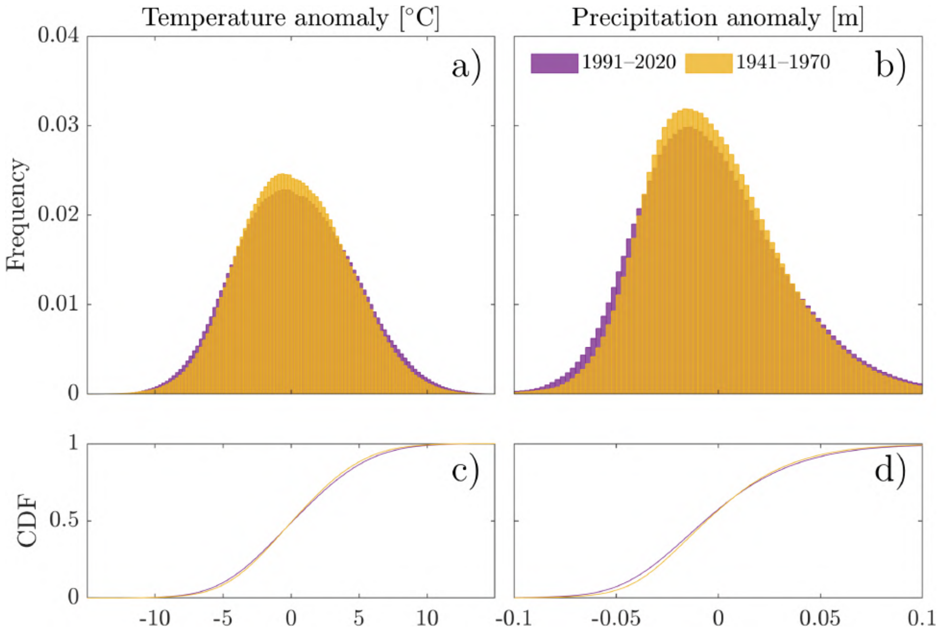

Figure A.13: **JJA Temperature and precipitation distributions for WCE. a)** Normalized histogram plots of temperature and **(b)** precipitation for the JJA season in 1941-1970 (yellow histograms) and in 1991-2020 (violet histograms). **c)** Cumulative distribution function of temperature and **(d)** precipitation for the JJA season in 1941-1970 (yellow line) and in 1991-2020 (violet line).

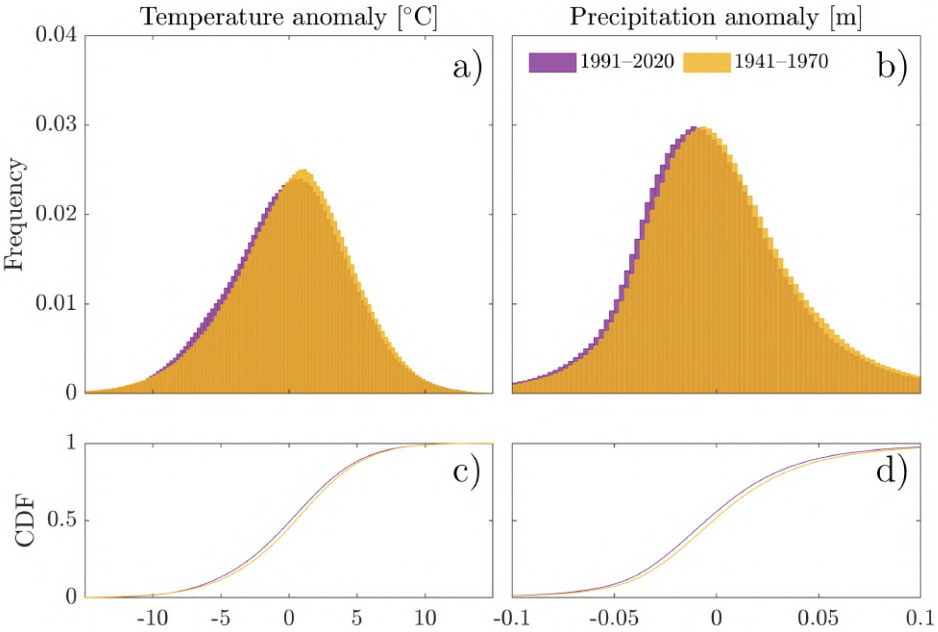

Figure A.14: **DJF Temperature and precipitation distributions for EMed. a)** Normalized histogram plots of temperature and **(b)** precipitation for the JJA season in 1941-1970 (yellow histograms) and in 1991-2020 (violet histograms). **c)** Cumulative distribution function of temperature and **(d)** precipitation for the JJA season in 1941-1970 (yellow line) and in 1991-2020 (violet line).

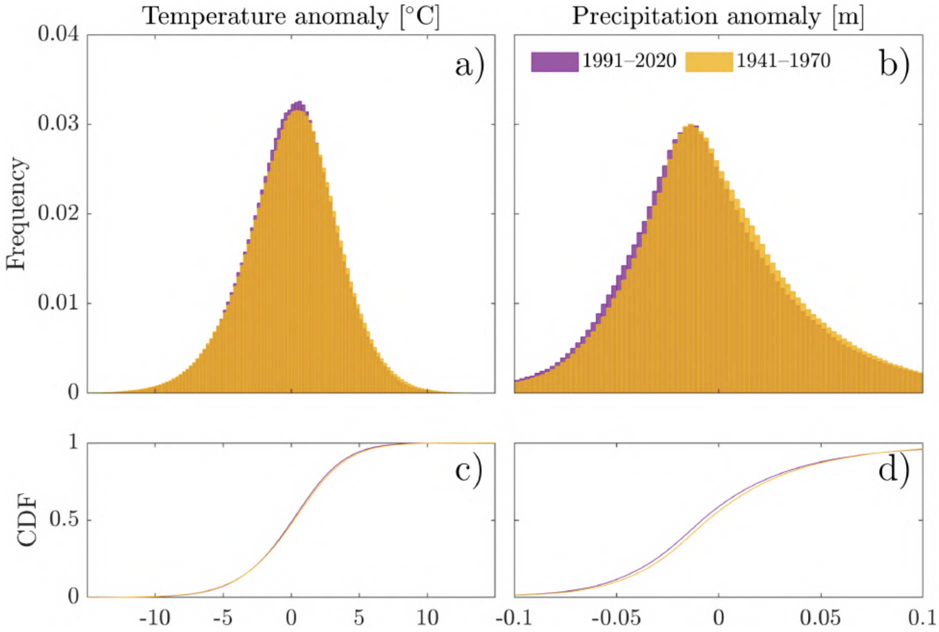

Figure A.15: **DJF Temperature and precipitation distributions for WMed. a)** Normalized histogram plots of temperature and **(b)** precipitation for the JJA season in 1941-1970 (yellow histograms) and in 1991-2020 (violet histograms). **c)** Cumulative distribution function of temperature and **(d)** precipitation for the JJA season in 1941-1970 (yellow line) and in 1991-2020 (violet line).

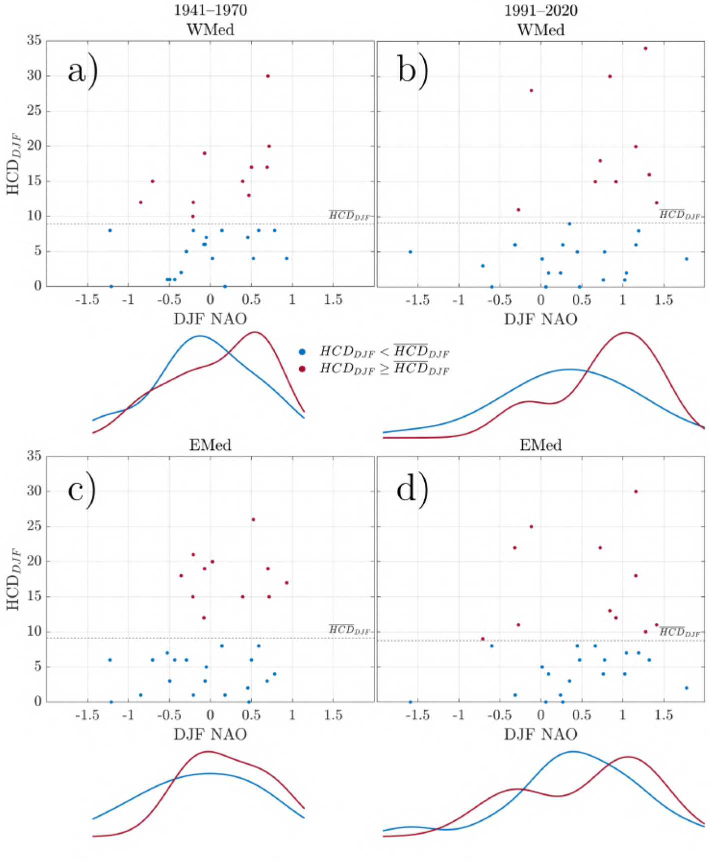

Figure A.16: **DJF HCD Vs. DJF NAO index.** **a)** Scatter plot of the number of HCD in WMed during one DJF season (HCD_{DJF}) and the corresponding value of the DJF NAO index for the 1941–1970 period. Red dots are seasons whose HCD_{DJF} is higher than the expected number of HCD if HCD where uniformly distributed in time ($\overline{HCD}_{DJF}$). Marginal distributions of the SNAO index of red and blue dots are depicted below the graph. **b)** Same as (a) but for WMed during 1991–2020. **c)** Same as (a) but for EMed during 1941–1971. **d)** Same as (a) but for EMed during 1991–2020.

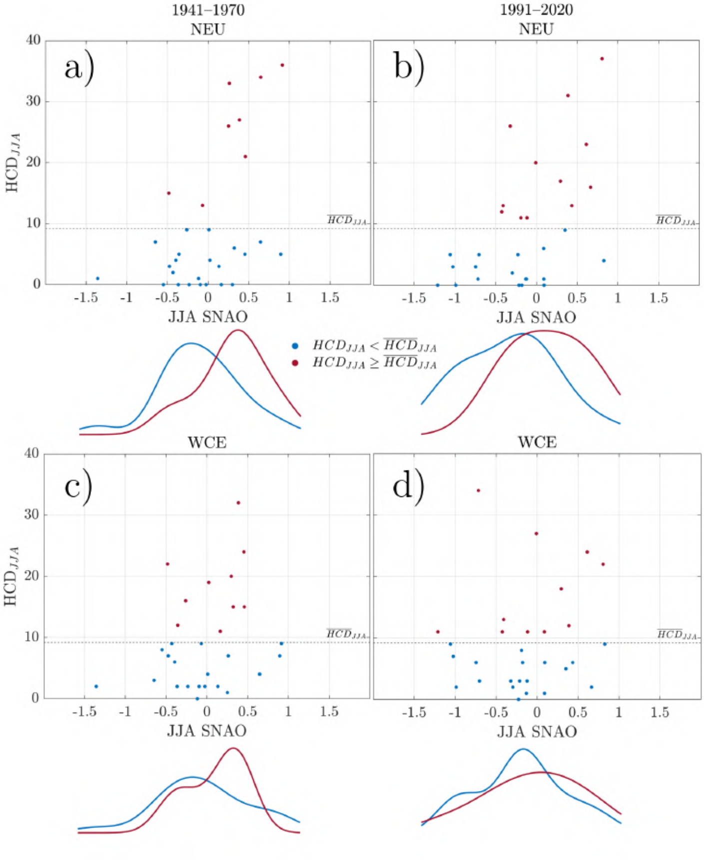

Figure A.17: **JJA HCD Vs. JJA SNAO index.** **a)** Scatter plot of the number of HCD in NEU during one JJA season (HCD_{JJA}) and the corresponding value of the JJA SNAO index for the 1941–1970 period. Red dots are seasons whose HCD_{JJA} is higher than the expected number of HCD if HCD where uniformly distributed in time ($\overline{HCD}_{JJA}$). Marginal distributions of the SNAO index of red and blue dots are depicted below the graph. **b)** Same as (a) but for NEU during 1991–2020. **c)** Same as (a) but for WCE during 1941–1971. **d)** Same as (a) but for WCE during 1991–2020.

Appendix B

Supplementary Material to Chapter 6

B.1 Selection procedure of the atmospheric precursors representative area

We select the representative area of the atmospheric precursors based on their ability to hindcast T2m and WSD variations. For the single extreme CEN, we calculate $Z500_T$ (Fig. B.1a) and $Z500_W$ (Fig. B.1b) by defining the representative area using one to three ridges and troughs at lag -1 and, consequently, we establish the corresponding CEN (Fig. B.1c-e). We show the hindcast model of T2m and WSD variations at the bottom of the corresponding CEN.

For each estimated hindcast model in Fig. B.1, we compute the ROC curve and the AUC value for T2m and WSD (Fig. B.2). The highest AUC values are reached when adopting the $Z500_T$ and $Z500_W$ computed by considering three pairs of ridges and troughs (Fig. B.2). Therefore, we use the three ridges and troughs pairs region (Figs. B.1a and B.1b) as the representative area of atmospheric precursors for single extreme CEN. The selection procedure of the representative area of $Z500_c$ is similar. In this case, a highest AUC value of 0.87 is reached when three pairs of ridges and troughs are considered as well.

B.2 Sensitivity test of the causal links to data length

To test the robustness of the single and compound extreme CENs, we perform 42 tests based on a sub-selection of years, from 1 to 42. The β values of each CEN derived from each sub-selected group of year are tested against a null model composed of up to 1000 random selection of group of years. The causal link strength of these 42 groups are shown in Figs. B.4-B.6, where the circles are the observed values and the box plots are derived from the null models corresponding to each sub-selection of years. In general, we notice that the sign and the strength of the β values are robust when changing the considered years, although larger variability can be observed when shorter subsets are considered (Figs. B.4-B.6).

Table B.1: Linear temporal correlation coefficients between the three atmospheric precursors time series.

Corr. coeff.	$Z500_T$	$Z500_W$	$Z500_c$
$Z500_T$	1	0.728	0.860
$Z500_W$		1	0.838
$Z500_c$			1

Table B.2: AIC index of different Copula models for SCHDI computation.

	Gaussian	t	Clayton	Gumbel	Frank	Rotated Joe 270 degrees
AIC	-498	-486	-415	-493	-475	-385

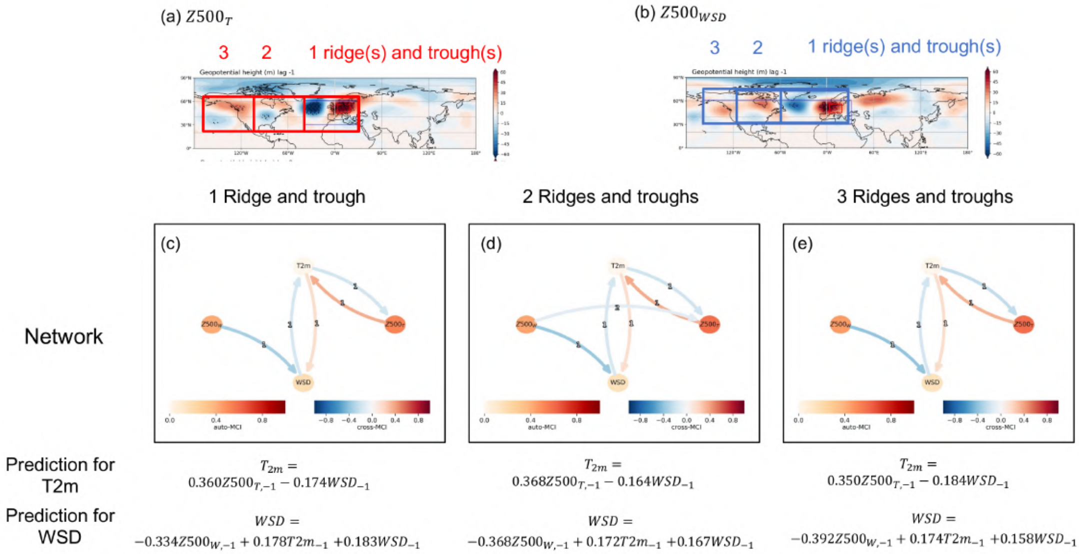

Figure B.1: Composites of Z500 fields at lag -1 for **a)** single hot extremes (T2m > $T2m_{95th}$) and **b)** single dry extremes (WSD < WSD_{5th}); red and blue boxes are drawn to highlight the ridge and trough pairs regions. **c-e)** CENs and the corresponding hindcast models for single extreme events based on atmospheric precursors with one to three pairs of ridges and troughs.

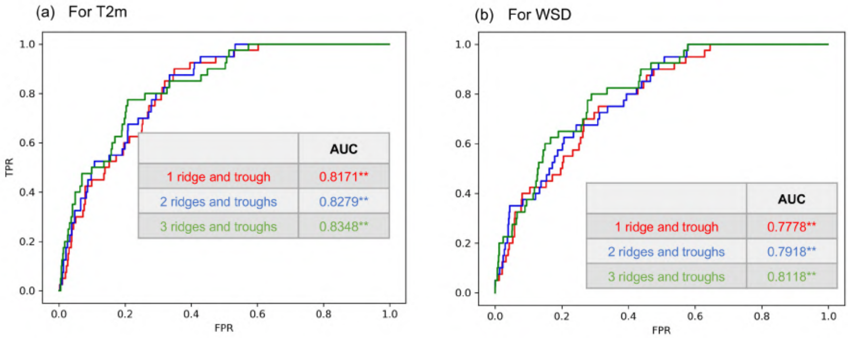

Figure B.2: ROC curve of hindcast models for single extreme events based on atmospheric precursors with one to three pairs of ridges and troughs.

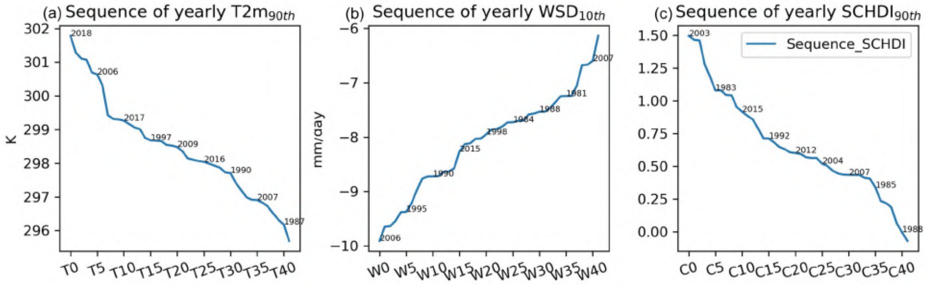

Figure B.3: Years ranking based on **a)** summer T_{90th} (descending order), **b)** summer WSD_{10th} (ascending order), and **c)** summer $SCHDI_{90th}$(descending order).

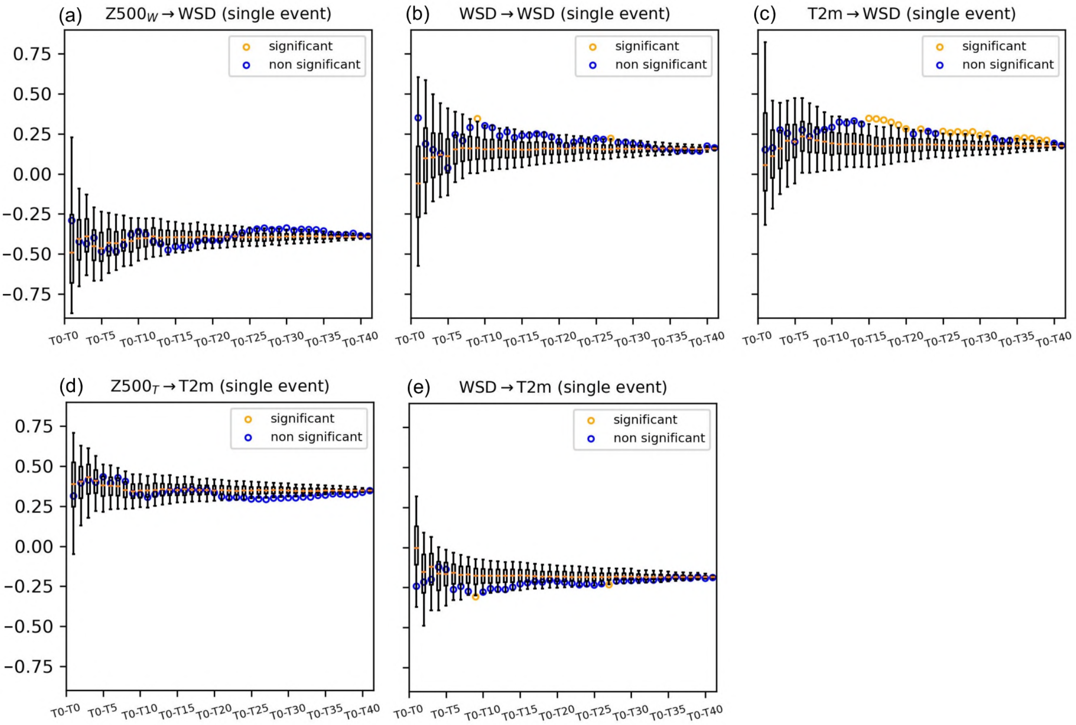

Figure B.4: The variation of β values with top 1 to 42 years ranking by yearly T2m$_{90\text{th}}$ during summer in a descending sequence (T$_0$ to T$_{41}$). For each dot, the β value is calculated using a sub-selection of 1-42 years. Box plots are drawn by computing the β value from 1000 (when possible) different realization of bootstrapped sets of years.

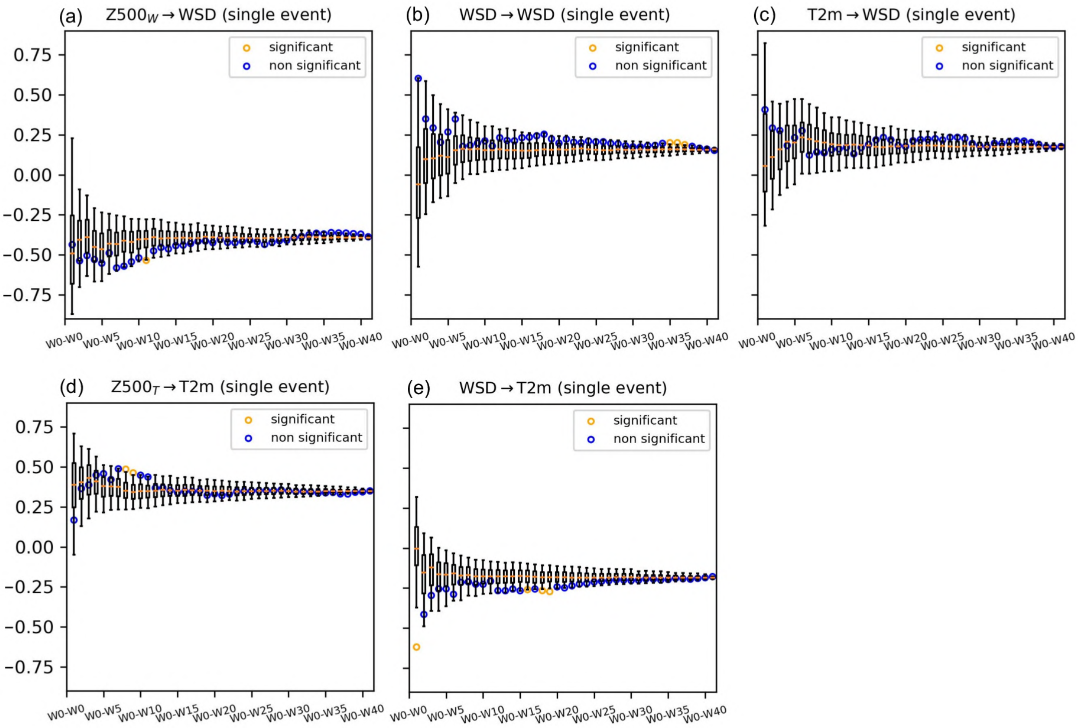

Figure B.5: The variation of β values with top 1 to 42 years ranking by yearly WSD$_{10th}$ during summer in a increasing sequence (W$_0$ to W$_{41}$). For each dot, the β value is calculated using a sub-selection of 1-42 years. Box plots are drawn by computing the β value from 1000 (when possible) different realization of bootstrapped sets of years.

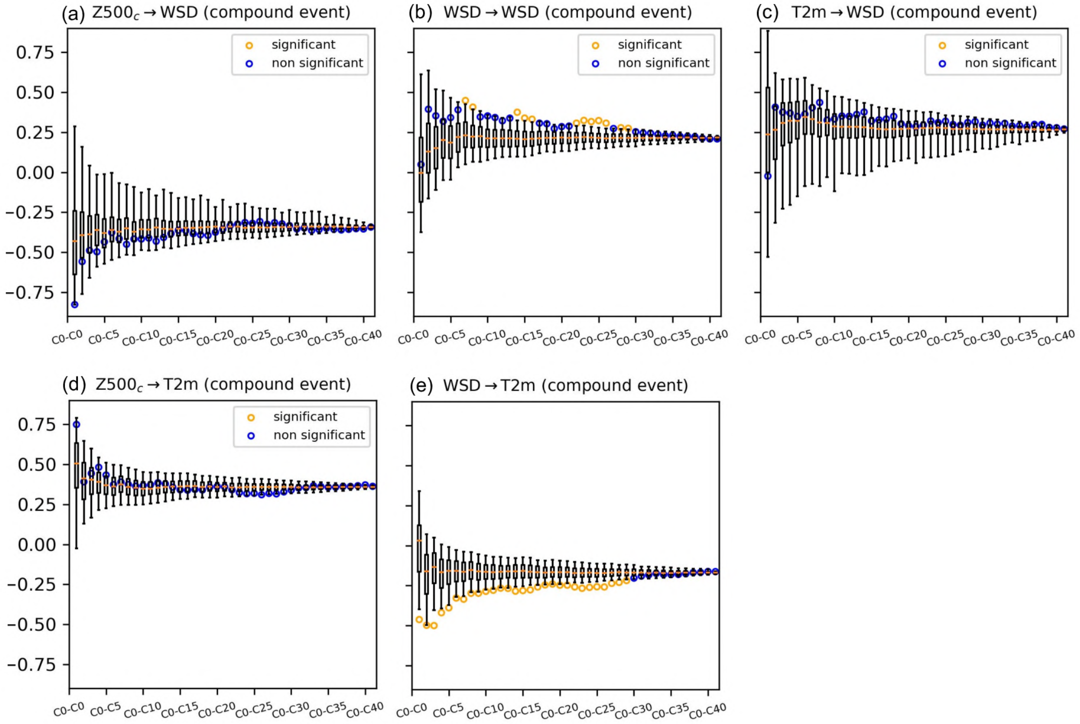

Figure B.6: The variation of β values with top 1 to 42 years ranking by yearly SCHDI$_{90\text{th}}$ during summer in a descending sequence (C$_0$ to C$_{41}$). For each dot, the β value is calculated using a sub-selection of 1-42 years. Box plots are drawn by computing the β value from 1000 (when possible) different realization of bootstrapped sets of years.

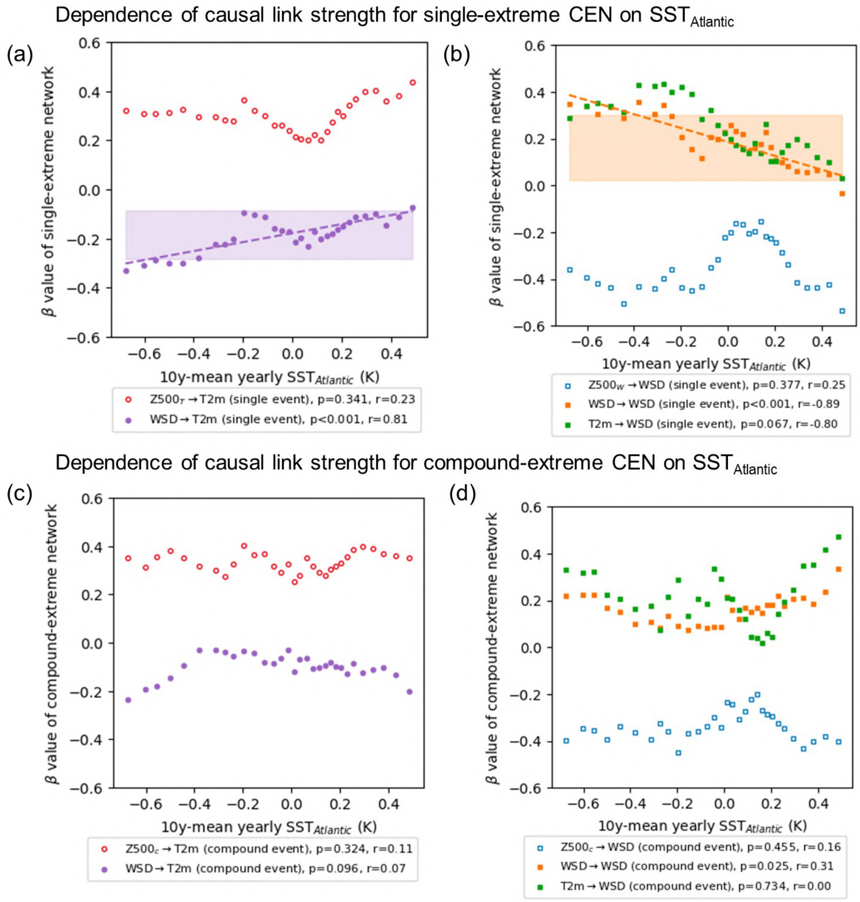

Figure B.7: Variation of causal links with Atlantic Ocean SSTs. Changes of β values in **a-b)** single extreme and **c, d)** compound CENs. Each β value is calculated using a 10-years moving window according to increasing seasonal mean SST$_{\text{Atlantic}}$ (45°-20° W, 45°-15° N). The shown linear regressions (dashed lines) are significant at $\alpha = 0.05$ and are characterized by a correlation coefficient between β value and SST$_{\text{Atlantic}}$. Circles and squares represent the causal links leading to T2m and WSD, respectively, while unfilled and filled scatters represent causal links where atmospheric precursors and land drivers are the causal drivers, respectively.

Bibliography

A. Agarwal, L. Caesar, N. Marwan, R. Maheswaran, B. Merz, and J. Kurths, “Multi-scale event synchronization analysis for unravelling climate processes: a wavelet-based approach,” *Nonlinear Processes in Geophysics*, vol. 24, no. 4, pp. 599–611, 2017.

A. AghaKouchak, F. Chiang, L. S. Huning, C. A. Love, I. Mallakpour, O. Mazdiyasni, H. Moftakhari, S. M. Papalexiou, E. Ragno, and M. Sadegh, “Climate extremes and compound hazards in a warming world,” *Annual Review of Earth and Planetary Sciences*, vol. 48, no. 1, pp. 519–548, 2020.

S. Arianos, E. Bompard, A. Carbone, and F. Xue, “Power grid vulnerability: A complex network approach,” *Chaos: An Interdisciplinary Journal of Nonlinear Science*, vol. 19, no. 1, 2009.

S. Arrhenius, “On the influence of carbonic acid in the air upon the temperature of the ground,” *Philosophical Magazine and Journal of Science*, vol. 41, p. 237–276, 1896.

M. Ausloos, F. Petroni, J. Johnson, Y.-C. Zhang, and G. Rotundo, “How visas shape and make visible the geopolitical architecture of the planet,” *Physica A: Statistical Mechanics and its Applications*, vol. 484, pp. 267–275, 2017.

E. Bach, S. Motesharrei, E. Kalnay, and A. Ruiz-Barradas, “Local atmosphere–ocean predictability: Dynamical origins, lead times, and seasonality,” *Journal of Climate*, vol. 32, no. 21, pp. 7507–7519, 2019.

J. W. Baldwin, J. B. Dessy, G. A. Vecchi, and M. Oppenheimer, “Temporally compound heat wave events and global warming: An emerging hazard,” *Earth’s Future*, vol. 7, no. 4, pp. 411–427, 2019.

J. Ballester, M. Quijal-Zamorano, R. F. Méndez Turrubiates, F. Pegenaute, F. R. Herrmann, J. M. Robine, X. Basagaña, C. Tonne, J. M. Antó, and H. Achebak, “Heat-related mortality in europe during the summer of 2022,” *Nature Medicine*, vol. 29, no. 7, pp. 1857–1866, 2023.

A.-L. Barabási and R. Albert, “Emergence of scaling in random networks,” *science*, vol. 286, no. 5439, pp. 509–512, 1999.

M. Bardoscia, G. Livan, M. Marsili, P. Castaldi, and S. Battiston, “The physics of financial networks,” *Nature Reviews Physics*, vol. 3, no. 7, pp. 490–507, 2021.

A. Bárdossy and H. Caspary, “Detection of climate change in Europe by analyzing European atmospheric circulation patterns from 1881 to 1989,” *Theoretical and Applied Climatology*, vol. 42, pp. 155–167, 1990.

S. Bartusek, K. Kornhuber, and M. Ting, “2021 North American heatwave amplified by climate change-driven nonlinear interactions,” *Nature Climate Change*, vol. 12, no. 12, pp. 1143–1150, 2022.

A. Bastos, Z. Fu, P. Ciais, P. Friedlingstein, S. Sitch, J. Pongratz, U. Weber, M. Reichstein, P. Anthoni, A. Arneth *et al.*, “Impacts of extreme summers on european ecosystems: a comparative analysis of 2003, 2010 and 2018,” *Philosophical Transactions of the Royal Society B*, vol. 375, no. 1810, p. 20190507, 2020.

M. M. M. Bateni, J. Behmanesh, C. De Michele, J. Bazrafshan, and H. Rezaie, “Composite agrometeorological drought index accounting for seasonality and autocorrelation,” *Journal of Hydrologic Engineering*, vol. 23, no. 6, 2017.

D. Beillouin, B. Schauberger, A. Bastos, P. Ciais, and D. Makowski, “Impact of extreme weather conditions on european crop production in 2018,” *Philosophical Transactions of the Royal Society B*, vol. 375, no. 1810, p. 20190510, 2020.

G. Benito, M. J. Machado, and A. Pérez-González, “Climate change and flood sensitivity in spain,” *Geological Society, London, Special Publications*, vol. 115, no. 1, pp. 85–98, 1996.

Y. Benjamini and Y. Hochberg, “Controlling the false discovery rate: a practical and powerful approach to multiple testing,” *Journal of the Royal Statistical Society: series B (Methodological)*, vol. 57, no. 1, pp. 289–300, 1995.

Y. Benjamini and D. Yekutieli, “The control of the false discovery rate in multiple testing under dependency,” *Annals of Statistics*, pp. 1165–1188, 2001.

A. Berg, B. R. Lintner, K. Findell, S. I. Seneviratne, B. van Den Hurk, A. Ducharne, F. Chéruy, S. Hagemann, D. M. Lawrence, S. Malyshev *et al.*, “Interannual coupling between summertime surface temperature and precipitation over land: Processes and implications for climate change,” *Journal of Climate*, vol. 28, no. 3, pp. 1308–1328, 2015.

W. R. Berghuijs, R. A. Woods, C. J. Hutton, and M. Sivapalan, “Dominant flood generating mechanisms across the united states,” *Geophysical Research Letters*, vol. 43, no. 9, pp. 4382–4390, 2016.

W. R. Berghuijs, S. Harrigan, P. Molnar, L. J. Slater, and J. W. Kirchner, “The relative importance of different flood-generating mechanisms across europe,” *Water Resources Research*, vol. 55, no. 6, pp. 4582–4593, 2019.

A. G. Bevacqua, P. L. Chaffe, V. B. Chagas, and A. AghaKouchak, "Spatial and temporal patterns of propagation from meteorological to hydrological droughts in brazil," *Journal of Hydrology*, vol. 603, p. 126902, 2021.

E. Bevacqua, D. Maraun, M. Vousdoukas, E. Voukouvalas, M. Vrac, L. Mentaschi, and M. Widmann, "Higher probability of compound flooding from precipitation and storm surge in europe under anthropogenic climate change," *Science Advances*, vol. 5, no. 9, p. eaaw5531, 2019.

E. Bevacqua, G. Zappa, F. Lehner, and J. Zscheischler, "Precipitation trends determine future occurrences of compound hot–dry events," *Nature Climate Change*, vol. 12, no. 17, p. 350–355, 2022.

G. Bianconi, *Higher-order networks*. Cambridge University Press, 2021.

V. Bjerknes, "Das problem der wettervorhersage, betrachtet vom standpunkte der mechanik und der physik," *Meteor. Z.*, vol. 21, pp. 1–7, 1904.

I. Bladé, B. Liebmann, D. Fortuny, and G. J. van Oldenborgh, "Observed and simulated impacts of the summer nao in europe: implications for projected drying in the mediterranean region," *Climate Dynamics*, vol. 39, pp. 709–727, 2012.

V. D. Blondel, J.-L. Guillaume, R. Lambiotte, and E. Lefebvre, "Fast unfolding of communities in large networks," *Journal of statistical mechanics: theory and experiment*, vol. 2008, no. 10, p. P10008, 2008.

S. Boccaletti, V. Latora, Y. Moreno, M. Chavez, and D.-U. Hwang, "Complex networks: Structure and dynamics," *Physics Reports*, vol. 424, no. 4-5, pp. 175–308, 2006.

S. Boccaletti, G. Bianconi, R. Criado, C. I. Del Genio, J. Gómez-Gardenes, M. Romance, I. Sendina-Nadal, Z. Wang, and M. Zanin, "The structure and dynamics of multilayer networks," *Physics reports*, vol. 544, no. 1, pp. 1–122, 2014.

S. Boccaletti, P. De Lellis, C. Del Genio, K. Alfaro-Bittner, R. Criado, S. Jalan, and M. Romance, "The structure and dynamics of networks with higher order interactions," *Physics Reports*, vol. 1018, pp. 1–64, 2023.

N. Boers, B. Bookhagen, N. Marwan, J. Kurths, and J. A. Ballesteros-Canovas, "Complex networks identify spatial patterns of extreme rainfall events of the south american monsoon system," *Geophysical Research Letters*, vol. 40, no. 16, pp. 4386–4392, 2013.

N. Boers, A. Rheinwalt, B. Bookhagen, H. M. Barbosa, N. Marwan, M. H. Trauth, and J. Kurths, "Complex networks reveal global pattern of extreme-rainfall teleconnections," *Nature*, vol. 566, no. 7744, pp. 373–377, 2019.

A. Böhnisch, M. Mittermeier, M. Leduc, and R. Ludwig, "Hot spots and climate trends of meteorological droughts in europe–assessing the percent of normal index in a single-model initial-condition large ensemble," *Frontiers in Water*, vol. 3, p. 716621, 2021.

D. G. Bonett and T. A. Wright, “Sample size requirements for estimating pearson, kendall and spearman correlations,” *Psychometrika*, vol. 65, pp. 23–28, 2000.

P. Borgnat, E. Fleury, J.-L. Guillaume, C. Magnien, C. Robardet, and A. Scherrer, “Evolving networks,” in *Mining massive data sets for security*. IOS Press, 2008, pp. 198–203.

A. Bretto, “Hypergraph theory,” *An introduction. Mathematical Engineering. Cham: Springer*, vol. 1, 2013.

C. Bueh and H. Nakamura, “Scandinavian pattern and its climatic impact,” *Quarterly Journal of the Royal Meteorological Society: A journal of the atmospheric sciences, applied meteorology and physical oceanography*, vol. 133, no. 629, pp. 2117–2131, 2007.

P. Bühlmann, “Sieve bootstrap for time series,” *Bernoulli*, pp. 123–148, 1997.

J. G. Charney, R. Fjörtoft, and J. v. Neumann, “Numerical integration of the barotropic vorticity equation,” *Tellus*, vol. 2, no. 4, pp. 237–254, 1950.

J. Cheng, M. Leng, L. Li, H. Zhou, and X. Chen, “Active semi-supervised community detection based on must-link and cannot-link constraints,” *PloS one*, vol. 9, no. 10, p. e110088, 2014.

J. I. Christian, J. B. Basara, E. D. Hunt, J. A. Otkin, J. C. Furtado, V. Mishra, X. Xiao, and R. M. Randall, “Global distribution, trends, and drivers of flash drought occurrence,” *Nature Communications*, vol. 12, no. 1, p. 6330, 2021.

P. Ciais, M. Reichstein, N. Viovy, A. Granier, J. Ogée, V. Allard, M. Aubinet, N. Buchmann, C. Bernhofer, A. Carrara *et al.*, “Europe-wide reduction in primary productivity caused by the heat and drought in 2003,” *Nature*, vol. 437, no. 7058, pp. 529–533, 2005.

C. Ciemer, L. Rehm, J. Kurths, R. V. Donner, R. Winkelmann, and N. Boers, “An early-warning indicator for amazon droughts exclusively based on tropical atlantic sea surface temperatures,” *Environmental Research Letters*, vol. 15, no. 9, p. 094087, 2020.

B. I. Cook, J. S. Mankin, and K. J. Anchukaitis, “Climate change and drought: From past to future,” *Current Climate Change Reports*, vol. 4, pp. 164–179, 2018.

B. I. Cook, J. S. Mankin, K. Marvel, A. P. Williams, J. E. Smerdon, and K. J. Anchukaitis, “Twenty-first century drought projections in the cmip6 forcing scenarios,” *Earth’s Future*, vol. 8, no. 6, p. e2019EF001461, 2020.

Copernicus, “European summer 2023: a season of contrasting extremes,” https://climate.copernicus.eu/european-summer-2023-season-contrasting-extremes, 2023, accessed: 11th September 2024.

——, “Precipitation, relative humidity and soil moisture for August 2023,” https://climate.copernicus.eu/precipitation-relative-humidity-and-soil-moisture-august-2023, 2023, accessed: 11th September 2024.

——, “Copernicus: 2023 is the hottest year on record, with global temperatures close to the 1.5°C limit,” https://climate.copernicus.eu/copernicus-2023-hottest-year-record, 2024, accessed: 11th September 2024.

Copernicus Climate Change Service, “Esotc 2023, precipitation,” https://climate.copernicus.eu/esotc/2023/precipitation, 2024, accessed: 11th November 2024.

——, “European state of the climate 2023,” https://climate.copernicus.eu/esotc/2023, 2024, accessed: 11th November 2024.

——, “Esotc 2023, river flow,” https://climate.copernicus.eu/esotc/2023/river-flow, 2024, accessed: 11th November 2024.

——, “Esotc 2023, soil moisture,” https://climate.copernicus.eu/esotc/2023/soil-moisture, 2024, accessed: 11th November 2024.

——, “Surface air temperature for june 2024,” https://climate.copernicus.eu/surface-air-temperature-june-2024, 2024, accessed: 11th November 2024.

——, “Precipitation, relative humidity and soil moisture for august 2023,” https://climate.copernicus.eu/precipitation-relative-humidity-and-soil-moisture-august-2023, 2024, accessed: 11th November 2024.

D. Coumou and S. Rahmstorf, “A decade of weather extremes,” *Nature climate change*, vol. 2, no. 7, pp. 491–496, 2012.

D. Coumou, V. Petoukhov, S. Rahmstorf, S. Petri, and H. J. Schellnhuber, “Quasi-resonant circulation regimes and hemispheric synchronization of extreme weather in boreal summer,” *Proceedings of the National Academy of Sciences*, vol. 111, no. 34, pp. 12 331–12 336, 2014.

T. Cropper, E. Hanna, M. A. Valente, and T. Jónsson, “A daily azores–iceland north atlantic oscillation index back to 1850,” *Geoscience Data Journal*, vol. 2, no. 1, pp. 12–24, 2015.

A. Dai, “Increasing drought under global warming in observations and models,” *Nature Climate Change*, vol. 3, no. 1, pp. 52–58, 2013.

P. De Luca and M. G. Donat, “Projected changes in hot, dry, and compound hot-dry extremes over global land regions,” *Geophysical Research Letters*, vol. 50, no. 13, p. e2022GL102493, 2023.

P. De Luca, G. Messori, D. Faranda, P. J. Ward, and D. Coumou, “Concurrent wet and dry hydrological extremes at the global scale,” *Earth System Dynamics*, vol. 11, no. 1, pp. 251–266, 2020.

G. Di Capua, M. Kretschmer, G. Zappa, and D. Coumou, “Drivers behind the summer 2010 wave train leading to russian heatwave and pakistan flooding,” *npj Climate and Atmospheric Science*, vol. 4, p. 7, 2021.

G. Di Capua and D. Coumou, “Changes in meandering of the Northern Hemisphere circulation,” *Environmental Research Letters*, vol. 11, no. 9, p. 094028, 2016.

G. Di Capua, M. Kretschmer, J. Runge, A. Alessandri, R. Donner, B. van Den Hurk, R. Vellore, R. Krishnan, and D. Coumou, “Long-lead statistical forecasts of the Indian summer monsoon rainfall based on causal precursors,” *Weather and Forecasting*, vol. 34, no. 5, pp. 1377–1394, 2019.

G. Di Capua, M. Kretschmer, R. V. Donner, B. Van Den Hurk, R. Vellore, R. Krishnan, and D. Coumou, “Tropical and mid-latitude teleconnections interacting with the indian summer monsoon rainfall: a theory-guided causal effect network approach,” *Earth System Dynamics*, vol. 11, no. 1, pp. 17–34, 2020.

G. Di Capua, M. Kretschmer, J. Runge, P. A. Arias, and D. Coumou, “Tropical and mid-latitude teleconnections interacting with the indian summer monsoon rainfall: a theory-guided causal effect network approach,” *Earth System Dynamics*, vol. 11, no. 1, pp. 17–34, 2020.

G. Di Capua, J. Runge, R. V. Donner, B. van den Hurk, A. G. Turner, R. Vellore, R. Krishnan, and D. Coumou, “Dominant patterns of interaction between the tropics and mid-latitudes in boreal summer: Causal relationships and the role of time-scales,” *Weather and Climate Dynamics Discussions*, vol. 2020, pp. 1–28, 2020.

C. Di Napoli, F. Pappenberger, and H. L. Cloke, “Assessing heat-related health risk in europe via the universal thermal climate index (utci),” *International Journal of Biometeorology*, vol. 62, pp. 1155–1165, 2018.

H. A. Dijkstra, E. Hernández-García, C. Masoller, and M. Barreiro, *Networks in climate*. Cambridge University Press, 2019.

P. A. Dirmeyer, G. Balsamo, E. M. Blyth, R. Morrison, and H. M. Cooper, “Land-atmosphere interactions exacerbated the drought and heatwave over northern europe during summer 2018,” *AGU Advances*, vol. 2, no. 2, p. e2020AV000283, 2021.

D. Docquier, G. Di Capua, R. V. Donner, C. A. Pires, A. Simon, and S. Vannitsem, “A comparison of two causal methods in the context of climate analyses,” *Nonlinear Processes in Geophysics*, vol. 31, no. 1, pp. 115–136, 2024.

J. F. Donges, H. C. Schultz, N. Marwan, Y. Zou, and J. Kurths, “The backbone of the climate network,” *Europhysics Letters*, vol. 87, no. 4, p. 48007, 2009.

J. F. Donges, Y. Zou, N. Marwan, and J. Kurths, “Complex networks in climate dynamics: Comparing linear and nonlinear network construction methods,” *The European Physical Journal Special Topics*, vol. 174, no. 1, pp. 157–179, 2009.

C. E. Doughty, D. Metcalfe, C. Girardin, F. F. Amézquita, D. G. Cabrera, W. H. Huasco, J. Silva-Espejo, A. Araujo-Murakami, M. Da Costa, W. Rocha *et al.*, “Drought impact on forest carbon dynamics and fluxes in amazonia,” *Nature*, vol. 519, no. 7541, pp. 78–82, 2015.

J. Douris and G. Kim, “The atlas of mortality and economic losses from weather, climate and water extremes (1970-2019),” *WMO*, no. 1267, 2021.

P. Drobinski, N. D. Silva, G. Panthou, S. Bastin, C. Muller, B. Ahrens, M. Borga, D. Conte, G. Fosser, F. Giorgi *et al.*, “Scaling precipitation extremes with temperature in the Mediterranean: past climate assessment and projection in anthropogenic scenarios,” *Climate Dynamics*, vol. 51, pp. 1237–1257, 2018.

A. Duchez, E. Frajka-Williams, S. A. Josey, D. G. Evans, J. P. Grist, R. Marsh, G. D. McCarthy, B. Sinha, D. I. Berry, and J. J. Hirschi, “Drivers of exceptionally cold North Atlantic Ocean temperatures and their link to the 2015 European heat wave,” *Environmental Research Letters*, vol. 11, no. 7, p. 074004, 2016.

N. Dunstone, D. M. Smith, S. C. Hardiman, L. Hermanson, S. Ineson, G. Kay, C. Li, J. F. Lockwood, A. A. Scaife, H. Thornton *et al.*, “Skilful predictions of the summer north atlantic oscillation,” *Communications Earth & Environment*, vol. 4, no. 1, p. 409, 2023.

N. Eagle, A. Pentland, and D. Lazer, “Inferring friendship network structure by using mobile phone data,” *Proceedings of the national academy of sciences*, vol. 106, no. 36, pp. 15 274–15 278, 2009.

D. C. Edwards, “Characteristics of 20th century drought in the united states at multiple time scales.” Air Force Inst of Tech Wright-Patterson Afb Oh, Tech. Rep., 1997.

S. Emori and S. Brown, “Dynamic and thermodynamic changes in mean and extreme precipitation under changed climate,” *Geophysical Research Letters*, vol. 32, no. 17, 2005.

P. Erdos and A. H. Stone, “On the structure of linear graphs,” *Bulletin of the American Mathematical Society*, vol. 52, no. 12, pp. 1087–1091, 1946.

P. Erdos, A. Rényi *et al.*, “On the evolution of random graphs,” *Publ. Math. Inst. Hung. Acad. Sci*, vol. 5, no. 1, pp. 17–60, 1960.

L. Euler, “Solutio problematis ad geometriam situs pertinentis,” *Commentarii academiae scientiarum Petropolitanae*, pp. 128–140, 1741.

European Drought Observatory, “Standardized precipitation index (spi),” European Drought Observatory, Tech. Rep., 2020.

V. Eyring, S. Bony, G. A. Meehl, C. A. Senior, B. Stevens, R. J. Stouffer, and K. E. Taylor, “Overview of the coupled model intercomparison project phase 6 (cmip6) experimental design and organization,” *Geoscientific Model Development*, vol. 9, no. 5, pp. 1937–1958, 2016.

J. Fan, J. Meng, Y. Ashkenazy, A. Bunde, S. Havlin, J. Ludescher, and H. J. Schellnhuber, "Statistical physics approaches to the complex earth system," *Physics Reports*, vol. 896, pp. 1–84, 2021.

Q. Y. Feng and H. Dijkstra, "Are north atlantic multidecadal sst anomalies westward propagating?" *Geophysical Research Letters*, vol. 41, no. 2, pp. 541–546, 2014.

X. Feng, C. Merow, Z. Liu, D. S. Park, P. R. Roehrdanz, B. Maitner, E. A. Newman, B. L. Boyle, A. Lien, J. R. Burger *et al.*, "How deregulation, drought and increasing fire impact amazonian biodiversity," *Nature*, vol. 597, no. 7877, pp. 516–521, 2021.

M.-L. Fernández and G. Valiente, "A graph distance metric combining maximum common subgraph and minimum common supergraph," *Pattern Recognition Letters*, vol. 22, no. 6-7, pp. 753–758, 2001.

C. B. Field, V. Barros, T. F. Stocker, and Q. Dahe, *Managing the risks of extreme events and disasters to advance climate change adaptation: special report of the intergovernmental panel on climate change*. Cambridge University Press, 2012.

A. H. Fink, T. Brücher, A. Krüger, G. C. Leckebusch, J. G. Pinto, and U. Ulbrich, "The 2003 european summer heatwaves and drought–synoptic diagnosis and impacts," *Weather*, vol. 59, no. 8, pp. 209–216, 2004.

E. Fischer, S. Sippel, and R. Knutti, "Increasing probability of record-shattering climate extremes," *Nature Climate Change*, vol. 11, no. 8, pp. 689–695, 2021.

C. K. Folland, J. Knight, H. W. Linderholm, D. Fereday, S. Ineson, and J. W. Hurrell, "The summer north atlantic oscillation: past, present, and future," *Journal of Climate*, vol. 22, no. 5, pp. 1082–1103, 2009.

S. Fortunato, "Community detection in graphs," *Physics reports*, vol. 486, no. 3-5, pp. 75–174, 2010.

H. Fowler and C. Kilsby, "A weather-type approach to analysing water resource drought in the yorkshire region from 1881 to 1998," *Journal of Hydrology*, vol. 262, no. 1-4, pp. 177–192, 2002.

J. A. Francis and S. J. Vavrus, "Evidence linking arctic amplification to extreme weather in mid-latitudes," *Geophysical Research Letters*, vol. 39, no. 6, p. L06801, 2012.

X. Gao, B. Xiao, D. Tao, and X. Li, "A survey of graph edit distance," *Pattern Analysis and applications*, vol. 13, pp. 113–129, 2010.

D. Giaquinto, W. Marzocchi, and J. Kurths, "Exploring meteorological droughts' spatial patterns across europe through complex network theory," *Nonlinear Processes in Geophysics Discussions*, pp. 1–19, 2023.

K.-I. Goh, M. E. Cusick, D. Valle, B. Childs, M. Vidal, and A.-L. Barabási, "The human disease network," *Proceedings of the National Academy of Sciences*, vol. 104, no. 21, pp. 8685–8690, 2007.

C. W. J. Granger, "Time series analysis, cointegration, and applications," *American Economic Review*, vol. 94, no. 3, pp. 421–425, 2004.

C. W. Granger, "Investigating causal relations by econometric models and cross-spectral methods," *Econometrica: journal of the Econometric Society*, pp. 424–438, 1969.

A. Gretton, K. Fukumizu, C. Teo, L. Song, B. Schölkopf, and A. Smola, "A kernel statistical test of independence," *Advances in neural information processing systems*, vol. 20, 2007.

L. Gudmundsson, F. C. Rego, M. Rocha, and S. I. Seneviratne, "Predicting above normal wildfire activity in southern europe as a function of meteorological drought," *Environmental Research Letters*, vol. 9, no. 8, p. 084008, 2014.

S. Gupta, K. Shivam Sundaram, A. Choudhury, and S. Roy, "Complex network approach for detecting tropical cyclones," *Climate Dynamics*, vol. 57, pp. 3355–3364, 2021.

S. Gupta, N. Mastrantonas, C. Masoller, and J. Kurths, "Perspectives on the importance of complex systems in understanding our climate and climate change—the nobel prize in physics 2021," *Chaos: An Interdisciplinary Journal of Nonlinear Science*, vol. 32, no. 5, 2022.

S. Gupta, Z. Su, N. Boers, J. Kurths, N. Marwan, and F. Pappenberger, "Interconnection between the indian and the east asian summer monsoon: Spatial synchronization patterns of extreme rainfall events," *International Journal of Climatology*, vol. 43, no. 2, 2022.

N. B. Guttman, "Accepting the standardized precipitation index: a calculation algorithm 1," *JAWRA Journal of the American Water Resources Association*, vol. 35, no. 2, pp. 311–322, 1999.

K.-J. Ha, Y.-W. Seo, J.-H. Yeo, A. Timmermann, E.-S. Chung, C. L. Franzke, J. C. Chan, S.-W. Yeh, and M. Ting, "Dynamics and characteristics of dry and moist heatwaves over east asia," *npj Climate and Atmospheric Science*, vol. 5, no. 1, p. 49, 2022.

M. S. Habibullah, B. H. Din, S.-H. Tan, and H. Zahid, "Impact of climate change on biodiversity loss: global evidence," *Environmental Science and Pollution Research*, vol. 29, no. 1, pp. 1073–1086, 2022.

A. Hall and X. Qu, "Using the current seasonal cycle to constrain snow albedo feedback in future climate change," *Geophysical Research Letters*, vol. 33, no. 3, 2006.

K. Hasselmann, "Stochastic climate models part i. theory," *tellus*, vol. 28, no. 6, pp. 473–485, 1976.

M. Hatzaki, G. Di Capua, J. Chaniotis, P. Patlakas, R. V. Donner, and H. A. Flocas, "Causal drivers of Mediterranean winter climate variability," *Environmental Sciences Proceedings*, vol. 26, no. 1, p. 155, 2023.

H. Hersbach, B. Bell, P. Berrisford, G. Biavati, A. Horányi, J. Muñoz Sabater, J. Nicolas, C. Peubey, R. Radu, I. Rozum, D. Schepers, A. Simmons, C. Soci, and D. Dee, "Era5 hourly data on single levels from 1940 to present," *Copernicus Climate Change Service (C3S) Climate Data Store (CDS)*, 2023.

H. Hersbach, B. Bell, P. Berrisford, G. Biavati, A. Horányi, J. Muñoz Sabater, J. Nicolas, C. Peubey, R. Radu, I. Rozum, D. Schepers, A. Simmons, C. Soci, D. Dee, and J.-N. Thépaut, "ERA5 hourly data on single levels from 1940 to present," *Copernicus Climate Change Service (C3S) Climate Data Store (CDS)*, 2023.

K. Hlaváčková-Schindler, M. Paluš, M. Vejmelka, and J. Bhattacharya, "Causality detection based on information-theoretic approaches in time series analysis," *Physics Reports*, vol. 441, no. 1, pp. 1–46, 2007.

H. Hoag, "Russian summer tops 'universal'heatwave index," *Nature*, vol. 16, no. 4, p. 636, 2014.

M. Hoerling, J. Eischeid, A. Kumar, R. Leung, A. Mariotti, K. Mo, S. Schubert, and R. Seager, "Causes and predictability of the 2012 Great Plains drought," *Bulletin of the American Meteorological Society*, vol. 95, no. 2, pp. 269–282, 2014.

M. Hofstätter, A. Lexer, M. Homann, and G. Blöschl, "Large-scale heavy precipitation over central europe and the role of atmospheric cyclone track types," *International Journal of Climatology*, vol. 38, no. Suppl Suppl 1, p. e497, 2018.

R. Hollmann, C. J. Merchant, R. Saunders, C. Downy, M. Buchwitz, A. Cazenave, E. Chuvieco, P. Defourny, G. de Leeuw, R. Forsberg *et al.*, "The esa climate change initiative: Satellite data records for essential climate variables," *Bulletin of the American Meteorological Society*, vol. 94, no. 10, pp. 1541–1552, 2013.

J. W. Hurrell, "Decadal trends in the north atlantic oscillation: Regional temperatures and precipitation," *Science*, vol. 269, no. 5224, pp. 676–679, 1995.

M. Ionita, L. M. Tallaksen, D. G. Kingston, J. H. Stagge, G. Laaha, and H. A. Van Lanen, "The european 2015 drought from a climatological perspective," *Hydrology and Earth System Sciences*, vol. 21, no. 3, pp. 1397–1419, 2017.

M. Ionita, D. E. Caldarescu, and V. Nagavciuc, "Compound Hot and Dry Events in Europe: Variability and Large-Scale Drivers," *Frontiers in Climate*, vol. 3, no. June, pp. 1–19, 2021.

——, "Compound Hot and Dry Events in Europe: Variability and Large-Scale Drivers," *Frontiers in Climate*, vol. 3, no. June, pp. 1–19, 2021.

IPCC, *Climate Change 2022 – Impacts, Adaptation and Vulnerability: Working Group II Contribution to the Sixth Assessment Report of the Intergovernmental Panel on Climate Change*. Cambridge University Press, 2023.

M. Iturbide, J. M. Gutiérrez, L. Alves, J. Bedia, E. Cimadevilla, A. S. Cofiño, R. Cerezo-Mota, C. Fioreze, M. García-Díez, S. Herrera *et al.*, "An update of ipcc climate reference regions for subcontinental analysis of climate model data: definition and aggregated datasets," *Earth System Science Data*, vol. 12, no. 4, pp. 2959–2970, 2020.

L. Jian and C. Hao-Ming, "Atlas in the ipcc ar6," *Advances in Climate Change Research*, vol. 17, no. 6, p. 726, 2021.

P. D. Jones, T. Jónsson, and D. Wheeler, "Extension to the north atlantic oscillation using early instrumental pressure observations from gibraltar and south-west iceland," *International Journal of Climatology: A Journal of the Royal Meteorological Society*, vol. 17, no. 13, pp. 1433–1450, 1997.

G. Jurman, R. Visintainer, and C. Furlanello, "An introduction to spectral distances in networks," in *Neural Nets Wirn10*. IOS Press, 2011, pp. 227–234.

L.-A. Kautz, O. Martius, S. Pfahl, J. G. Pinto, A. M. Ramos, P. M. Sousa, and T. Woollings, "Atmospheric blocking and weather extremes over the Euro-Atlantic sector – a review," *Weather and Climate Dynamics*, vol. 3, no. 1, pp. 305–336, 2022.

——, "Atmospheric blocking and weather extremes over the Euro-Atlantic sector – a review," *Weather and Climate Dynamics*, vol. 3, no. 1, pp. 305–336, 2022.

M. G. Kendall, "A new measure of rank correlation," *Biometrika*, vol. 30, no. 1-2, pp. 81–93, 1938.

G. Konapala, S. Mondal, and A. Mishra, "Quantifying spatial drought propagation potential in north america using complex network theory," *Water Resources Research*, vol. 58, no. 3, p. e2021WR030914, 2022.

K. Kornhuber, S. Osprey, D. Coumou, S. Petri, and V. Petoukhov, "Extreme weather events in early summer 2018 connected by a recurrent hemispheric wave-7 pattern," *Environmental Research Letters*, vol. 14, no. 5, p. 054002, 2019.

K. Kornhuber, D. Coumou, E. Vogel, C. Lesk, J. F. Donges, G. Murray-Tortarolo, and J. Rockström, "Amplified rossby waves enhance risk of concurrent heatwaves in major breadbasket regions," *Nature Climate Change*, vol. 10, no. 1, pp. 48–53, 2020.

J.-P. Kreiss, "Asymptotical properties of residual bootstrap for autoregressions," Institute für Mathematik, Techn. Univ., Tech. Rep., 1997.

M. Kretschmer, D. Coumou, J. F. Donges, and J. Runge, "Using causal effect networks to analyze different arctic drivers of midlatitude winter circulation," *Journal of climate*, vol. 29, no. 11, pp. 4069–4081, 2016.

M. Kretschmer, J. Runge, and D. Coumou, "Early prediction of extreme stratospheric polar vortex states based on causal precursors," *Geophysical Research Letters*, vol. 44, no. 16, pp. 8592–8600, 2017.

J. Kurths, A. Agarwal, R. Shukla, N. Marwan, M. Rathinasamy, L. Caesar, R. Krishnan, and B. Merz, “Unravelling the spatial diversity of indian precipitation teleconnections via a non-linear multi-scale approach,” *Nonlinear Processes in Geophysics*, vol. 26, no. 3, pp. 251–266, 2019.

G. Lancaster, D. Iatsenko, A. Pidde, V. Ticcinelli, and A. Stefanovska, “Surrogate data for hypothesis testing of physical systems,” *Physics Reports*, vol. 748, pp. 1–60, 2018.

A. Lancichinetti and S. Fortunato, “Limits of modularity maximization in community detection,” *Physical Review E—Statistical, Nonlinear, and Soft Matter Physics*, vol. 84, no. 6, p. 066122, 2011.

R. Leeding, J. Riboldi, and G. Messori, “On pan-atlantic cold, wet and windy compound extremes,” *Weather and Climate Extremes*, vol. 39, p. 100524, 2023.

J. Lehmann, D. Coumou, and K. Frieler, “Increased record-breaking precipitation events under global warming,” *Climatic Change*, vol. 132, pp. 501–515, 2015.

T. M. Lenton, H. Held, E. Kriegler, J. W. Hall, W. Lucht, S. Rahmstorf, and H. J. Schellnhuber, “Tipping elements in the earth’s climate system,” *Proceedings of the national Academy of Sciences*, vol. 105, no. 6, pp. 1786–1793, 2008.

M. Leonard, S. Westra, A. Phatak, M. Lambert, B. van den Hurk, K. McInnes, J. Risbey, S. Schuster, D. Jakob, and M. Stafford-Smith, “A compound event framework for understanding extreme impacts,” *Wiley Interdisciplinary Reviews: Climate Change*, vol. 5, no. 1, pp. 113–128, 2014.

C. Lesk, E. Coffel, J. Winter, D. Ray, J. Zscheischler, S. I. Seneviratne, and R. Horton, “Stronger temperature–moisture couplings exacerbate the impact of climate warming on global crop yields,” *Nature Food*, vol. 2, no. 9, pp. 683–691, 2021.

D. Li, J. Yuan, and R. E. Kopp, “Escalating global exposure to compound heat-humidity extremes with warming,” *Environmental Research Letters*, vol. 15, no. 6, p. 064003, 2020.

J. Li, Z. Wang, X. Wu, J. Zscheischler, S. Guo, and X. Chen, “A standardized index for assessing sub-monthly compound dry and hot conditions with application in China,” *Hydrology and Earth System Sciences*, vol. 25, no. 3, pp. 1587–1601, 2021.

H. W. Linderholm, C. K. Folland, and A. Walther, “A multicentury perspective on the summer north atlantic oscillation (snao) and drought in the eastern atlantic region,” *Journal of Quaternary Science: Published for the Quaternary Research Association*, vol. 24, no. 5, pp. 415–425, 2009.

B. Lloyd-Hughes, “The impracticality of a universal drought definition,” *Theoretical and Applied Climatology*, vol. 117, no. 3, pp. 607–611, 2014.

E. N. Lorenz, “Deterministic nonperiodic flow,” *Journal of atmospheric sciences*, vol. 20, no. 2, pp. 130–141, 1963.

R. Lorenz, D. Argüeso, M. G. Donat, A. J. Pitman, B. van den Hurk, A. Berg, D. M. Lawrence, F. Chéruy, A. Ducharne, S. Hagemann *et al.*, "Influence of land-atmosphere feedbacks on temperature and precipitation extremes in the glace-cmip5 ensemble," *Journal of Geophysical Research: Atmospheres*, vol. 121, no. 2, pp. 607–623, 2016.

J. Ludescher, A. Bunde, C. Franzke, and H. J. Schellnhuber, "Network-based forecasting of climate phenomena," *Proceedings of the National Academy of Sciences*, vol. 118, no. 47, p. e1922872118, 2021.

E. Madonna, J. T. Pasquier, M. Croci-Maspoli, A. P. Weigel, and C. C. Raible, "Reconstructing winter climate anomalies in the euro-atlantic sector using circulation patterns," *Weather and Climate Dynamics*, vol. 2, no. 3, pp. 777–794, 2021.

P. J. Mailier, D. B. Stephenson, C. A. Ferro, and K. I. Hodges, "Serial clustering of extratropical cyclones," *Monthly weather review*, vol. 134, no. 8, pp. 2224–2240, 2006.

N. Malik, N. Marwan, and J. Kurths, "Spatial structures and directionalities in monsoonal precipitation over south asia," *Nonlinear Processes in Geophysics*, vol. 17, no. 5, pp. 371–381, 2010.

N. Malik, B. Bookhagen, N. Marwan, and J. Kurths, "Analysis of spatial and temporal extreme monsoonal rainfall over south asia using complex networks," *Climate Dynamics*, vol. 39, pp. 971–987, 2012.

C. Manning, M. Widmann, E. Bevacqua, A. F. Van Loon, D. Maraun, and M. Vrac, "Soil moisture drought in europe: a compound event of precipitation and potential evapotranspiration on multiple time scales," *Journal of Hydrometeorology*, vol. 19, no. 8, pp. 1255–1271, 2018.

C. Manning, M. Widmann, E. Bevacqua, A. F. Van Loon, and D. Maraun, "Increased probability of compound long-duration dry and hot events in europe during summer (1950–2013)," *Environmental Research Letters*, vol. 14, no. 9, p. 094006, 2019.

P. Marinho Ferreira Barbosa, D. Masante, C. Arias-Muñoz, C. Cammalleri, A. De Jager, D. Magni, M. Mazzeschi, N. Mccormick, G. Naumann, J. Spinoni, and J. Vogt, *Droughts in Europe and Worldwide 2019-2020.* Luxembourg (Luxembourg): Publications Office of the European Union, 2021, no. KJ-NA-30719-EN-N (online).

A. Mariotti and P. Arkin, "The north atlantic oscillation and oceanic precipitation variability," *Climate Dynamics*, vol. 28, pp. 35–51, 2007.

N. D. Martinez, "Artifacts or attributes? effects of resolution on the little rock lake food web," *Ecological monographs*, vol. 61, no. 4, pp. 367–392, 1991.

S. Maslov, K. Sneppen, and A. Zaliznyak, "Detection of topological patterns in complex networks: correlation profile of the internet," *Physica A: Statistical Mechanics and its Applications*, vol. 333, pp. 529–540, 2004.

C. McCain, S. Hooker, G. Feldman, and P. Bontempi, “Satellite data for ocean biology, biogeochemistry, and climate research,” *Eos, Transactions American Geophysical Union*, vol. 87, no. 34, pp. 337–343, 2006.

M. C. McGraw and E. A. Barnes, “Memory matters: A case for granger causality in climate variability studies,” *Journal of climate*, vol. 31, no. 8, pp. 3289–3300, 2018.

T. B. McKee, N. J. Doesken, J. Kleist *et al.*, “The relationship of drought frequency and duration to time scales,” in *Proceedings of the 8th Conference on Applied Climatology*, vol. 17, no. 22. Boston, MA, USA, 1993, pp. 179–183.

J. Mellado-Cano, P. Ortega, J. Martín-Chivelet, J. J. Díaz, M. Jiménez, M. Montoya, A. Gómez-Pellicer, and A. Moreno, “Examining the north atlantic oscillation, east atlantic pattern, and jet variability since 1685,” *Journal of Climate*, vol. 32, no. 19, pp. 6285–6298, 2019.

D. G. Miralles, A. J. Teuling, C. C. Van Heerwaarden, and J. Vilà-Guerau de Arellano, “Mega-heatwave temperatures due to combined soil desiccation and atmospheric heat accumulation,” *Nature Geoscience*, vol. 7, no. 5, pp. 345–349, 2014.

A. K. Mishra and V. P. Singh, “A review of drought concepts,” *Journal of hydrology*, vol. 391, no. 1-2, pp. 202–216, 2010.

D. Mitchell, K. Kornhuber, J. Wolff, and C. Huntingford, “The day the 2003 european heatwave record was broken,” *The Lancet Planetary Health*, vol. 3, no. 7, pp. e290–e292, 2019.

K. C. Mo and D. P. Lettenmaier, “Heat wave flash droughts in decline,” *Geophysical Research Letters*, vol. 42, no. 8, pp. 2823–2829, 2015.

——, “Prediction of flash droughts over the United States,” *Journal of Hydrometeorology*, vol. 21, no. 8, pp. 1793–1810, 2020.

J. M. Montoya, S. L. Pimm, and R. V. Solé, “Ecological networks and their fragility,” *Nature*, vol. 442, no. 7100, pp. 259–264, 2006.

S. Mukherjee, A. Mishra, and K. E. Trenberth, “Climate change and drought: a perspective on drought indices,” *Current Climate Change Reports*, vol. 4, no. 2, pp. 145–163, 2018.

S. Mukherjee, A. K. Mishra, J. Zscheischler, and D. Entekhabi, “Interaction between dry and hot extremes at a global scale using a cascade modeling framework,” *Nature Communications*, vol. 14, no. 1, pp. 1–15, 2023.

G. Naumann, C. Cammalleri, L. Mentaschi, and L. Feyen, “Increased economic drought impacts in europe with anthropogenic warming,” *Nature Climate Change*, vol. 11, no. 6, pp. 485–491, 2021.

M. Newman, *Networks*. Oxford university press, 2018.

M. E. Newman, "The structure and function of complex networks," *SIAM review*, vol. 45, no. 2, pp. 167–256, 2003.

——, "Modularity and community structure in networks," *Proceedings of the national academy of sciences*, vol. 103, no. 23, pp. 8577–8582, 2006.

N. Nicholls, D. Easterling, C. Goodess, S. Kanae, J. Kossin, Y. Luo, J. Marengo, K. McInnes, M. Rahimi, M. Reichstein *et al.*, "Changes in climate extremes and their impacts on the natural physical environment," *Managing the risks of extreme events and disasters to advance climate change adaptation*, pp. 109–230, 2012.

K. Noguchi, Y. R. Gel, and C. R. Duguay, "Bootstrap-based tests for trends in hydrological time series, with application to ice phenology data," *Journal of Hydrology*, vol. 410, no. 3-4, pp. 150–161, 2011.

R. Orth and S. I. Seneviratne, "Analysis of soil moisture memory from observations in Europe," *Journal of Geophysical Research: Atmospheres*, vol. 117, no. D15, 2012.

J. A. Otkin, M. Svoboda, E. D. Hunt, T. W. Ford, M. C. Anderson, C. Hain, and J. B. Basara, "Flash droughts: A review and assessment of the challenges imposed by rapid-onset droughts in the United States," *Bulletin of the American Meteorological Society*, vol. 99, no. 5, pp. 911–919, 2018.

M. C. Peel, B. L. Finlayson, and T. A. McMahon, "Updated world map of the köppen-geiger climate classification," *Hydrology and Earth System Sciences*, vol. 11, no. 5, pp. 1633–1644, 2007.

S. E. Perkins and L. V. Alexander, "On the measurement of heat waves," *Journal of Climate*, vol. 26, no. 13, pp. 4500–4517, 2013.

P. Pfleiderer, C.-F. Schleussner, T. Geiger, and M. Kretschmer, "Robust predictors for seasonal Atlantic hurricane activity identified with causal effect networks," *Weather and Climate Dynamics*, vol. 1, no. 2, pp. 313–324, 2020.

I. D. Phillips and G. R. McGregor, "The utility of a drought index for assessing the drought hazard in devon and cornwall, south west england," *Meteorological Applications*, vol. 5, no. 4, pp. 359–372, 1998.

J. J. Potterat, L. Phillips-Plummer, S. Q. Muth, R. Rothenberg, D. Woodhouse, T. Maldonado-Long, H. Zimmerman, and J. Muth, "Risk network structure in the early epidemic phase of hiv transmission in colorado springs," *Sexually transmitted infections*, vol. 78, no. suppl 1, pp. i159–i163, 2002.

D. J. D. S. Price, "Networks of scientific papers: The pattern of bibliographic references indicates the nature of the scientific research front." *Science*, vol. 149, no. 3683, pp. 510–515, 1965.

R. Quian Quiroga, T. Kreuz, and P. Grassberger, "Event synchronization: a simple and fast method to measure synchronicity and time delay patterns," *Physical Review E*, vol. 66, no. 4, p. 041904, 2002.

R. Q. Quiroga, T. Kreuz, and P. Grassberger, “Event synchronization: a simple and fast method to measure synchronicity and time delay patterns,” *Physical review E*, vol. 66, no. 4, p. 041904, 2002.

F. Radicchi, C. Castellano, F. Cecconi, V. Loreto, and D. Parisi, “Defining and identifying communities in networks,” *Proceedings of the national academy of sciences*, vol. 101, no. 9, pp. 2658–2663, 2004.

M. Rahiz and M. New, “Spatial coherence of meteorological droughts in the uk since 1914,” *Area*, vol. 44, no. 4, pp. 400–410, 2012.

S. Rahmstorf and D. Coumou, “Increase of extreme events in a warming world,” *Proceedings of the National Academy of Sciences*, vol. 108, no. 44, pp. 17 905–17 909, 2011.

C. E. Rasmussen and C. K. Williams, “Gaussian processes for machine learning cambridge,” *MA: the MIT Press.*, 2006.

A. Rheinwalt, N. Marwan, J. Kurths, and P. Werner, “Boundary effects in network measures of spatially embedded networks,” in *2012 SC Companion: High Performance Computing, Networking Storage and Analysis*. IEEE, 2012, pp. 1082–1103.

——, “Non-linear time series analysis of precipitation events using regional climate networks for germany,” *Climate Dynamics*, vol. 46, pp. 1065–1074, 2016.

L. F. Richardson, *Weather prediction by numerical process*. University Press, 1922.

J.-M. Robine, S. L. K. Cheung, S. Le Roy, H. Van Oyen, C. Griffiths, J.-P. Michel, and F. R. Herrmann, “Death toll exceeded 70,000 in europe during the summer of 2003,” *Comptes Rendus. Biologies*, vol. 331, no. 2, pp. 171–178, 2008.

A. Robinson, J. Lehmann, D. Barriopedro, S. Rahmstorf, and D. Coumou, “Increasing heat and rainfall extremes now far outside the historical climate,” *npj Climate and Atmospheric Science*, vol. 4, no. 1, p. 45, 2021.

M. Röthlisberger and L. Papritz, “Quantifying the physical processes leading to atmospheric hot extremes at a global scale,” *Nature Geoscience*, vol. 16, pp. 210–216, 2023.

E. Rousi, C. Anagnostopoulos, K. Tolika, and P. Maheras, “An nao climatology in reanalysis data with the use of self-organizing maps,” in *Perspectives on Atmospheric Sciences*. Springer International Publishing, 2017, pp. 853–859.

E. Rousi, C. Anagnostopoulos, S. Fragkidis, G. C. Hegerl, and A. K. Paschalidou, “Implications of winter nao flavors on present and future european climate,” *Climate*, vol. 8, no. 1, p. 13, 2020.

E. Rousi, K. Kornhuber, G. Beobide-Arsuaga, F. Luo, and D. Coumou, “Accelerated western European heatwave trends linked to more-persistent double jets over Eurasia,” *Nature Communications*, vol. 13, no. 1, p. 3851, 2022.

E. Rousi, R. Vautard, C. Barbier, A. Jézéquel, F. E. L. Otto, Y. Keraunos, M. R. Haylock, and G. C. Hegerl, "The extremely hot and dry 2018 summer in central and northern europe from a multi-faceted weather and climate perspective," *Natural Hazards and Earth System Sciences*, vol. 23, no. 5, pp. 1699–1718, 2023.

E. Rousi, C. Anagnostopoulos, S. Fragkidis, G. C. Hegerl, and A. K. Paschalidou, "Changes in north atlantic atmospheric circulation in a warmer climate favor winter flooding and summer drought over europe," *Journal of Climate*, vol. 34, no. 6, pp. 2277–2295, 2021.

J. Ruffault, V. Moron, R. Trigo, and T. Curt, "Objective identification of multiple large fire climatologies: an application to a mediterranean ecosystem," *Environmental Research Letters*, vol. 11, no. 7, p. 075006, 2016.

J. Runge, "Causal network reconstruction from time series: From theoretical assumptions to practical estimation," *Chaos: An Interdisciplinary Journal of Nonlinear Science*, vol. 28, no. 7, 2018.

——, "Discovering contemporaneous and lagged causal relations in autocorrelated nonlinear time series datasets," in *Conference on Uncertainty in Artificial Intelligence*. Pmlr, 2020, pp. 1388–1397.

J. Runge, V. Petoukhov, and J. Kurths, "Quantifying the strength and delay of climatic interactions: The ambiguities of cross correlation and a novel measure based on graphical models," *Journal of Climate*, vol. 27, no. 2, pp. 720–739, 2014.

J. Runge, V. Petoukhov, J. F. Donges, J. Hlinka, N. Jajcay, M. Vejmelka, D. Hartman, N. Marwan, M. Paluš, and J. Kurths, "Identifying causal gateways and mediators in complex spatio-temporal systems," *Nature Communications*, vol. 6, no. 1, p. 8502, 2015.

J. Runge, P. Nowack, M. Kretschmer, S. Flaxman, and D. Sejdinovic, "Detecting and quantifying causal associations in large nonlinear time series datasets," *Science Advances*, vol. 5, no. 11, p. eaau4996, 2019.

S. Russo, J. Sillmann, and E. M. Fischer, "Top ten European heatwaves since 1950 and their occurrence in the coming decades," *Environmental Research Letters*, vol. 10, no. 12, p. 124003, 2015.

G. Salvadori, C. De Michele, N. T. Kottegoda, and R. Rosso, *Extremes in nature: an approach using copulas*. Springer Science & Business Media, 2007, vol. 56.

F. Sariş, D. M. Hannah, and W. J. Eastwood, "Spatial variability of precipitation regimes over turkey," *Hydrological Sciences Journal–Journal des Sciences Hydrologiques*, vol. 55, no. 2, pp. 234–249, 2010.

T. Schreiber, "Measuring information transfer," *Physical review letters*, vol. 85, no. 2, p. 461, 2000.

B. Schwikowski, P. Uetz, and S. Fields, “A network of protein–protein interactions in yeast,” *Nature biotechnology*, vol. 18, no. 12, pp. 1257–1261, 2000.

S. I. Seneviratne, N. Nicholls, D. Easterling, C. M. Goodess, S. Kanae, J. Kossin, Y. Luo, J. Marengo, K. McInnes, M. Rahimi, M. Reichstein, A. Sorteberg, C. Vera, and X. Zhang, “Changes in climate extremes and their impacts on the natural physical environment,” in *Managing the Risks of Extreme Events and Disasters to Advance Climate Change Adaptation*, C. B. Field, V. Barros, T. F. Stocker, D. Qin, D. J. Dokken, K. L. Ebi, M. D. Mastrandrea, K. J. Mach, G.-K. Plattner, S. K. Allen, M. Tignor, and P. M. Midgley, Eds. Cambridge, UK and New York, NY, USA: Cambridge University Press, 2012, pp. 109–230.

S. I. Seneviratne, D. Lüthi, M. Litschi, and C. Schär, “Land–atmosphere coupling and climate change in Europe,” *Nature*, vol. 443, no. 7108, pp. 205–209, 2006.

S. I. Seneviratne, T. Corti, E. L. Davin, M. Hirschi, E. B. Jaeger, I. Lehner, B. Orlowsky, and A. J. Teuling, “Investigating soil moisture–climate interactions in a changing climate: A review,” *Earth-Science Reviews*, vol. 99, no. 3-4, pp. 125–161, 2010.

S. I. Seneviratne, R. Wartenburger, B. P. Guillod, A. L. Hirsch, M. M. Vogel, V. Brovkin, D. P. van Vuuren, N. Schaller, L. Boysen, K. V. Calvin *et al.*, “Climate extremes, land–climate feedbacks and land-use forcing at 1.5 c,” *Philosophical Transactions of the Royal Society A: Mathematical, Physical and Engineering Sciences*, vol. 376, no. 2119, p. 20160450, 2018.

S. I. Seneviratne, X. Zhang, M. Adnan, W. Badi, C. Dereczynski, A. D. Luca, S. Ghosh, I. Iskandar, J. Kossin, S. Lewis *et al.*, “Weather and climate extreme events in a changing climate,” *Climate Change 2021: The Physical Science Basis. Contribution of Working Group I to the Sixth Assessment Report of the Intergovernmental Panel on Climate Change*, 2021.

Y.-W. Seo and K.-J. Ha, “Changes in land-atmosphere coupling increase compound drought and heatwaves over northern east asia,” *npj Climate and Atmospheric Science*, vol. 5, no. 1, p. 100, 2022.

J. Shah, V. Hari, O. Rakovec, Y. Markonis, L. Samaniego, V. Mishra, M. Hanel, C. Hinz, and R. Kumar, “Increasing footprint of climate warming on flash droughts occurrence in Europe,” *Environmental Research Letters*, vol. 17, no. 6, p. 064017, 2022.

D. Sharma, S. Das, and B. Goswami, “Variability and predictability of the Northeast India summer monsoon rainfall,” *International Journal of Climatology*, vol. 43, no. 11, pp. 5248–5268, 2023.

R. Shields, “Cultural topology: The seven bridges of königsburg, 1736,” *Theory, Culture & Society*, vol. 29, no. 4-5, pp. 43–57, 2012.

S. Solomon, D. Qin, M. Manning, Z. Chen, M. Marquis, K. Averyt, M. Tignor, and H. Miller, “Climate change 2007: The physical science basis. contribution of working group i to the fourth assessment report of the intergovernmental panel on climate change," *IPCC*, 2007.

C. Spearman, "The proof and measurement of association between two things," *The American journal of psychology*, vol. 100, no. 3/4, pp. 441–471, 1987.

J. Spinoni, G. Naumann, J. V. Vogt, and P. Barbosa, "World drought frequency, duration, and severity for 1951–2010," *International Journal of Climatology*, vol. 34, no. 8, pp. 2792–2804, 2014.

J. Spinoni, G. Naumann, J. Vogt, and P. Barbosa, "European drought climatologies and trends based on a multi-indicator approach," *Global and Planetary Change*, vol. 127, pp. 50–57, 2015.

J. Spinoni, G. Naumann, J. V. Vogt, and P. Barbosa, "The biggest drought events in Europe from 1950 to 2012," *Journal of Hydrology: Regional Studies*, vol. 3, pp. 509–524, 2015.

J. Spinoni, G. Naumann, J. Vogt, and P. Barbosa, *Meteorological droughts in europe: events and impacts-past trends and future projections*. Publications Office of the European Union, 2016.

J. Spinoni, G. Naumann, and J. V. Vogt, "Pan-european seasonal trends and recent changes of drought frequency and severity," *Global and Planetary Change*, vol. 148, pp. 113–130, 2017.

J. Spinoni, J. V. Vogt, G. Naumann, P. Barbosa, and A. Dosio, "Will drought events become more frequent and severe in europe?" *International Journal of Climatology*, vol. 38, no. 4, pp. 1718–1736, 2018.

J. Spinoni, P. Barbosa, E. Bucchignani, J. Cassano, T. Cavazos, J. H. Christensen, O. B. Christensen, E. Coppola, J. Evans, B. Geyer *et al.*, "Future global meteorological drought hot spots: a study based on CORDEX data," *Journal of Climate*, vol. 33, no. 9, pp. 3635–3661, 2020.

J. Spinoni, P. Barbosa, E. Bucchignani, J. Cassano, T. Cavazos, A. Cescatti, J. H. Christensen, O. B. Christensen, E. Coppola, J. P. Evans *et al.*, "Global exposure of population and land-use to meteorological droughts under different warming levels and ssps: a cordex-based study," *International Journal of Climatology*, vol. 41, no. 15, pp. 6825–6853, 2021.

P. Spirtes, C. Glymour, and R. Scheines, *Causation, prediction, and search*. MIT press, 2001.

V. Stolbova, P. Martin, B. Bookhagen, N. Marwan, and J. Kurths, "Topology and seasonal evolution of the network of extreme precipitation over the indian subcontinent and sri lanka," *Nonlinear Processes in Geophysics*, vol. 21, no. 4, pp. 901–917, 2014.

J. D. Storey, “False discovery rate.” *International encyclopedia of statistical science*, vol. 1, pp. 504–508, 2011.

P. A. Stott, D. A. Stone, and M. R. Allen, “Human contribution to the european heatwave of 2003,” *Nature*, vol. 432, no. 7017, pp. 610–614, 2004.

F. M. Strnad, N. Boers, B. Goswami, A. Rheinwalt, B. Bookhagen, H. M. J. Barbosa, and J. Kurths, “Propagation pathways of indo-pacific rainfall extremes are modulated by pacific sea surface temperatures,” *Nature Communications*, vol. 14, no. 1, p. 5708, 2023.

S. H. Strogatz, “Exploring complex networks,” *nature*, vol. 410, no. 6825, pp. 268–276, 2001.

J. Su, D. Chen, D. Zheng, Y. Su, and X. Li, “The insight of why: Causal inference in earth system science,” *Science China Earth Sciences*, vol. 66, no. 10, pp. 2169–2186, 2023.

L. Suarez-Gutierrez, W. A. Müller, C. Li, and J. Marotzke, “Dynamical and thermodynamical drivers of variability in European summer heat extremes,” *Climate Dynamics*, vol. 54, pp. 4351–4366, 2020.

G. Sugihara, R. May, H. Ye, C.-h. Hsieh, E. Deyle, M. Fogarty, and S. Munch, “Detecting causality in complex ecosystems,” *science*, vol. 338, no. 6106, pp. 496–500, 2012.

S. J. Sutanto, C. Vitolo, C. Di Napoli, M. D’Andrea, and H. A. Van Lanen, “Heatwaves, droughts, and fires: Exploring compound and cascading dry hazards at the pan-european scale,” *Environment international*, vol. 134, p. 105276, 2020.

G. J. Székely, M. L. Rizzo, and N. K. Bakirov, “Measuring and testing dependence by correlation of distances,” *Ann. Statist.*, 2007.

H. Tabari and P. Willems, “Global risk assessment of compound hot-dry events in the context of future climate change and socioeconomic factors,” *NPJ Climate and Atmospheric Science*, vol. 6, no. 1, p. 74, 2023.

M. Taufik, P. J. Torfs, R. Uijlenhoet, P. D. Jones, D. Murdiyarso, and H. A. Van Lanen, “Amplification of wildfire area burnt by hydrological drought in the humid tropics,” *Nature Climate Change*, vol. 7, no. 6, pp. 428–431, 2017.

A. Tavakol, V. Rahmani, and J. Harrington Jr, “Temporal and spatial variations in the frequency of compound hot, dry, and windy events in the central united states,” *Scientific Reports*, vol. 10, no. 1, p. 15691, 2020.

A. J. Teuling, A. F. Van Loon, S. I. Seneviratne, I. Lehner, M. Aubinet, B. Heinesch, C. Bernhofer, T. Grünwald, H. Prasse, and U. Spank, “Evapotranspiration amplifies european summer drought,” *Geophysical Research Letters*, vol. 40, no. 10, pp. 2071–2075, 2013.

M. Thomas and A. T. Joy, *Elements of information theory*. Wiley-Interscience, 2006.

Y. Tian, S. A. Ghausi, Y. Zhang, M. Zhang, D. Xie, Y. Cao, Y. Mei, G. Wang, D. Zhong, and A. Kleidon, “Radiation as the dominant cause of high-temperature extremes on the eastern Tibetan Plateau,” *Environmental Research Letters*, vol. 18, no. 7, p. 074007, 2023.

K. E. Trenberth and D. J. Shea, “Relationships between precipitation and surface temperature,” *Geophysical Research Letters*, vol. 32, no. 14, 2005.

K. P. Tripathy, S. Mukherjee, A. K. Mishra, M. E. Mann, and A. P. Williams, “Climate change will accelerate the high-end risk of compound drought and heatwave events,” *Proceedings of the National Academy of Sciences*, vol. 120, no. 28, p. 2017, jul 2023.

K. P. Tripathy and A. K. Mishra, “How unusual is the 2022 european compound drought and heatwave event?” *Geophysical Research Letters*, vol. 50, no. 15, p. e2023GL105453, 2023.

A. A. Tsonis and P. J. Roebber, “The architecture of the climate network,” *Physica A: Statistical Mechanics and its Applications*, vol. 333, pp. 497–504, 2004.

A. A. Tsonis, K. L. Swanson, and P. J. Roebber, “What do networks have to do with climate?” *Bulletin of the American Meteorological Society*, vol. 87, no. 5, pp. 585–596, 2006.

A. A. Tsonis, K. L. Swanson, and G. Wang, “On the role of atmospheric teleconnections in climate,” *Journal of Climate*, vol. 21, no. 12, pp. 2990–3001, 2008.

J. Tyndall, “The bakerian lecture—on the absorption and radiation of heat by gases and vapours, and on the physical connexion of radiation, absorption, and conduction,” *Proceedings of the Royal Society of London*, no. 11, pp. 100–104, 1862.

J. R. Ullmann, “An algorithm for subgraph isomorphism,” *Journal of the ACM (JACM)*, vol. 23, no. 1, pp. 31–42, 1976.

S. M. Vallejo-Bernal, A. M. Ramos, A. R. Pereira, M. L. Liberato, R. M. Trigo, and D. A. Lavers, “The role of atmospheric rivers in the distribution of heavy precipitation events over north america,” *Hydrology and Earth System Sciences*, vol. 27, no. 14, pp. 2645–2660, 2023.

S. Vannitsem and P. Ekelmans, “Causal dependences between the coupled ocean–atmosphere dynamics over the tropical pacific, the north pacific and the north atlantic,” *Earth System Dynamics*, vol. 9, no. 3, pp. 1063–1083, 2018.

R. Vautard, J. Cattiaux, T. Happé, J. Singh, R. Bonnet, C. Cassou, D. Coumou, F. D’Andrea, D. Faranda, E. Fischer *et al.*, “Heat extremes in Western Europe are increasing faster than simulated due to missed atmospheric circulation trends,” *Nature Communications*, vol. 14, p. 6803, 2023.

R. Vautard, A. Gobiet, S. Sobolowski, E. Kjellström, A. Stegehuis, P. Watkiss, T. Mendlik, O. Landgren, G. Nikulin, C. Teichmann *et al.*, "The European climate under a 2° C global warming," *Environmental Research Letters*, vol. 9, no. 3, p. 034006, 2014.

S. M. Vicente-Serrano, F. Domínguez-Castro, C. Murphy, J. Hannaford, F. Reig, D. Peña-Angulo, Y. Tramblay, R. M. Trigo, N. Mac Donald, M. Y. Luna *et al.*, "Long-term variability and trends in meteorological droughts in western europe (1851–2018)," *International journal of climatology*, vol. 41, pp. E690–E717, 2021.

J.-P. Vidal, E. Martin, L. Franchistéguy, F. Habets, J.-M. Soubeyroux, M. Blanchard, and M. Baillon, "Multilevel and multiscale drought reanalysis over france with the safran-isba-modcou hydrometeorological suite," *Hydrology and Earth System Sciences*, vol. 14, no. 3, pp. 459–478, 2010.

M. M. Vogel, J. Zscheischler, R. Wartenburger, D. Dee, and S. I. Seneviratne, "Concurrent 2018 hot extremes across Northern Hemisphere due to human-induced climate change," *Earth's Future*, vol. 7, no. 7, pp. 692–703, 2019.

M. M. Vogel, J. Zscheischler, and S. I. Seneviratne, "Varying soil moisture–atmosphere feedbacks explain divergent temperature extremes and precipitation projections in central Europe," *Earth System Dynamics*, vol. 9, no. 3, pp. 1107–1125, 2018.

M. M. Vogel, R. Orth, F. Cheruy, S. Hagemann, R. Lorenz, B. J. van den Hurk, and S. I. Seneviratne, "Regional amplification of projected changes in extreme temperatures strongly controlled by soil moisture-temperature feedbacks," *Geophysical Research Letters*, vol. 44, no. 3, pp. 1511–1519, 2017.

C. L. Walthall, J. Hatfield, P. Backlund, L. Lengnick, E. Marshall, M. Walsh, S. Adkins, M. Aillery, E. Ainsworth, C. Ammann *et al.*, *Climate change and agriculture in the United States: Effects and adaptation.* United States Department of Agriculture, Agricultural Research Services . . . , 2013.

L. Wang and M. Ting, "Stratosphere-troposphere coupling leading to extended seasonal predictability of summer north atlantic oscillation and boreal climate," *Geophysical Research Letters*, vol. 49, no. 2, p. e2021GL096362, 2022.

L. Wang, X. Yuan, Z. Xie, P. Wu, and Y. Li, "Increasing flash droughts over China during the recent global warming hiatus," *Scientific Reports*, vol. 6, no. 1, p. 30571, 2016.

X. F. Wang, "Complex networks: topology, dynamics and synchronization," *International journal of bifurcation and chaos*, vol. 12, no. 05, pp. 885–916, 2002.

Y. Wang, X. Yang, and Z.-H. Wang, "Causal mediation of urban temperature by geopotential height in us cities," *Sustainable Cities and Society*, vol. 100, p. 105010, 2024.

D. J. Watts and S. H. Strogatz, "Collective dynamics of 'small-world'networks," *nature*, vol. 393, no. 6684, pp. 440–442, 1998.

M. Wehner, S. Seneviratne, X. Zhang, M. Adnan, W. Badi, C. Dereczynski, A. Di Luca, S. Ghosh, I. Iskandar, J. Kossin *et al.*, "Weather and climate extreme events in a changing climate," in *AGU Fall Meeting Abstracts*, vol. 2021, 2021, pp. U13B–11.

W. Wei, J. Zhang, L. Zhou, B. Xie, J. Zhou, and C. Li, "Comparative evaluation of drought indices for monitoring drought based on remote sensing data," *Environmental Science and Pollution Research*, vol. 28, no. 16, pp. 20 408–20 425, 2021.

R. H. White, K. Kornhuber, O. Martius, and V. Wirth, "From atmospheric waves to heatwaves: A waveguide perspective for understanding and predicting concurrent, persistent, and extreme extratropical weather," *Bulletin of the American Meteorological Society*, vol. 103, no. 3, pp. E923–E935, 2022.

D. A. Wilhite and M. H. Glantz, "Understanding: the drought phenomenon: the role of definitions," *Water International*, vol. 10, no. 3, pp. 111–120, 1985.

D. S. Wilks, *Statistical methods in the atmospheric sciences*. Academic press, 2011, vol. 100.

WMO, "Atlas of mortality and economic losses from weather, climate and water extremes (1970–2019)," *WMO-No. 1267*, vol. WMO- No. 1090, 2021.

World Meteorological Organization, "WMO guidelines on the calculation of climate normals (WMO-no. 1203)," WMO, Geneva, Tech. Rep., 2017. [Online]. Available: https://library.wmo.int/idurl/4/55797

W. Xu, Y. Hou, Y. Hung, and Y. Zou, "A comparative analysis of spearman's rho and kendall's tau in normal and contaminated normal models," *Signal Processing*, vol. 93, no. 1, pp. 261–276, 2013.

N. Yadav, K. Rajendra, A. Awasthi, C. Singh, and B. Bhushan, "Systematic exploration of heat wave impact on mortality and urban heat island: A review from 2000 to 2022," *Urban Climate*, vol. 51, p. 101622, 2023.

K. Yamasaki, A. Gozolchiani, and S. Havlin, "Climate networks around the globe are significantly affected by el nino," *Physical review letters*, vol. 100, no. 22, p. 228501, 2008.

X. Yang, Z.-H. Wang, C. Wang, and Y.-C. Lai, "Finding causal gateways of precipitation over the contiguous united states," *Geophysical Research Letters*, vol. 50, no. 4, p. e2022GL101942, 2023.

K. Ye and G. Messori, "Two leading modes of wintertime atmospheric circulation drive the recent warm arctic–cold eurasia temperature pattern," *Journal of Climate*, vol. 33, no. 13, pp. 5565–5587, 2020.

J. Yin, P. Gentine, L. Slater, L. Gu, Y. Pokhrel, N. Hanasaki, S. Guo, L. Xiong, and W. Schlenker, "Future socio-ecosystem productivity threatened by compound drought–heatwave events," *Nature Sustainability*, vol. 6, no. 3, pp. 259–272, 2023.

N. Ying, D. Zhou, Z. Han, Q. Chen, Q. Ye, and Z. Xue, “Rossby waves detection in the co2 and temperature multilayer climate network,” *Geophysical Research Letters*, vol. 47, no. 2, p. e2019GL086507, 2020.

X. Yuan, L. Wang, E. F. Wood *et al.*, “Anthropogenic intensification of Southern African flash droughts as exemplified by the 2015/16 season,” *Bulletin of the American Meteorological Society*, vol. 99, no. 1, pp. S86–S90, 2018.

W. W. Zachary, “An information flow model for conflict and fission in small groups,” *Journal of anthropological research*, vol. 33, no. 4, pp. 452–473, 1977.

L. A. Zager and G. C. Verghese, “Graph similarity scoring and matching,” *Applied mathematics letters*, vol. 21, no. 1, pp. 86–94, 2008.

M. Zanin, P. Sousa, D. Papo, R. Bajo, J. García-Prieto, F. d. Pozo, E. Menasalvas, and S. Boccaletti, “Optimizing functional network representation of multivariate time series,” *Scientific reports*, vol. 2, no. 1, pp. 1–6, 2012.

A. Zargar, R. Sadiq, B. Naser, and F. I. Khan, “A review of drought indices,” *Environmental Reviews*, vol. 19, no. NA, pp. 333–349, 2011.

X. Zhang, N. Chen, H. Sheng, C. Ip, L. Yang, Y. Chen, Z. Sang, T. Tsegaye, P. Lim, A. Rajabifard *et al.*, “Urban drought challenge to 2030 sustainable development goals,” *Science of the Total Environment*, 2019.

T. Zhao and A. Dai, “Uncertainties in historical changes and future projections of drought. part ii: model-simulated historical and future drought changes,” *Climatic Change*, vol. 144, no. 3, pp. 535–548, 2017.

T. Zhao, T. S. Connor, X. Hao, X. Chen, F. Wang, and S. Yin, “Compound dry and hot events over major river basins of the world from 1921 to 2020,” *Weather and Climate Extremes*, vol. 44, p. 100679, 2024.

S. Zhou, A. P. Williams, A. M. Berg, B. I. Cook, Y. Zhang, S. Hagemann, R. Lorenz, S. I. Seneviratne, and P. Gentine, “Land–atmosphere feedbacks exacerbate concurrent soil drought and atmospheric aridity,” *Proceedings of the National Academy of Sciences*, vol. 116, no. 38, pp. 18 848–18 853, 2019.

J. Zscheischler and S. I. Seneviratne, “Dependence of drivers affects risks associated with compound events,” *Science Advances*, vol. 3, no. 6, p. e1700263, 2017.

J. Zscheischler, R. Orth, and S. I. Seneviratne, “A submonthly database for detecting changes in vegetation-atmosphere coupling,” *Geophysical Research Letters*, vol. 42, no. 22, pp. 9816–9824, 2015.

——, “Bivariate return periods of temperature and precipitation explain a large fraction of european crop yields,” *Biogeosciences*, vol. 14, no. 13, pp. 3309–3320, 2017.

J. Zscheischler, S. Westra, B. J. Van Den Hurk, S. I. Seneviratne, P. J. Ward, A. Pitman, A. AghaKouchak, D. N. Bresch, M. Leonard, T. Wahl *et al.*, “Future climate risk from compound events,” *Nature Climate Change*, vol. 8, no. 6, pp. 469–477, 2018.

J. Zscheischler, O. Martius, S. Westra, E. Bevacqua, C. Raymond, R. M. Horton, B. van den Hurk, A. AghaKouchak, A. Jézéquel, M. D. Mahecha, D. Maraun, A. M. Ramos, N. N. Ridder, W. Thiery, and E. Vignotto, “A typology of compound weather and climate events,” *Nature Reviews Earth and Environment*, vol. 1, no. 7, pp. 333–347, 2020.

J. Zscheischler, O. Martius, S. Westra, E. Bevacqua, C. Raymond, R. M. Horton, B. van den Hurk, A. AghaKouchak, A. Jézéquel, M. D. Mahecha *et al.*, “A typology of compound weather and climate events,” *Nature Reviews Earth & Environment*, vol. 1, no. 7, pp. 333–347, 2020.

P. Zschenderlein, A. H. Fink, S. Pfahl, and H. Wernli, “Processes determining heat waves across different European climates,” *Quarterly Journal of the Royal Meteorological Society*, vol. 145, no. 724, pp. 2973–2989, 2019.